A POSITION SENSORLESS CONTROL OF SWITCHED RELUCTANCE MOTORS

A POSITION SENSORLESS CONTROL OF SWITCHED RELUCTANCE MOTORS

By

Xiao Wang, B.Sc.

A Thesis
Submitted to the School of Graduate Studies
in Partial Fulfillment of the Requirements
for the Degree
Master of Applied Science

McMaster University

Master OF APPLIED SCIENCE(2016)   McMASTER UNIVERSITY
(Electrical and Computer Engineering)   Hamilton, Ontario

TITLE: **A Position Sensorless Control of Switched Reluctance Motors**

AUTHOR: Xiao Wang
B. Sc.
Electrical Engineering and Automation Department
(Tianjin University of Science & Technology, Tianjin, China)

SUPERVISOR: Ali Emadi, Professor
Ph. D. (Texas A&M University)
IEEE Fellow
Canada Excellence Research Chair in Hybrid Powertrain

NUMBER OF PAGES: XIV, 143

谨以此献给我的母亲父亲

To My Parents

ABSTRACT

Switched reluctance motor (SRM) is an attractive candidate for many industrial and domestic applications such as electric vehicles and home appliances. Rotor position detection is of significant importance for SRM control. However, external position sensors like absolute encoders and magnetic sensors reduce the reliability of SRM drive system in hash environments and increase the cost. Therefore, position sensorless control becomes a promising technique for SRM.

In this thesis, a new position sensorless control method for SRM is proposed to estimate rotor position and speed. Sliding mode observer is adopted at high speed and pulse injection method is adopted at low speed. Both of the two methods are adopted with a motion model based on the third order phase locked loop to improve the dynamic tracking performance. The analysis method of the proposed position sensorless method is also presented.

Both simulation and experiment results are presented to verify the proposed sensorless control method. The simulation results show that the proposed method can precisely estimate rotor position and speed with short response time. Experimental results further demonstrate the reliability and effectiveness of the proposed positon sensorless control method.

ACKNOWLEDGEMENTS

First of all, I would like to express my sincere gratitude to my advisor Dr. Ali Emadi for his full support, expert guidance, and encouragement throughout my master study and research. Besides, this research was undertaken, in part, thanks to funding from the Canada Excellence Research Chairs Program and the Natural Sciences and Engineering Research Council of Canada Discovery Grants Program.

Special thanks must go to Dr. Peng for his advice and support in my research and publications. His help in every aspect was imperative to my completion of my research work. I also would like to thank all my fellow graduate students in McMaster Institute for Automotive Research and Technology (MacAUTO) for their help, accompaniment, and concerns.

Last but not least, I owe my loving thanks to my parents for their endless support and generous love through my entire life. They are my friends and teachers in my life, and they give me the motivation to be hardworking, serious, and stronger.

CONTENT

LIST OF FIGURES

XIII

LIST OF TABLES

Chapter 1

INTRODUCTION

1.1. THE FEATURES OF SRM DRIVE

Switched reluctance motor (SRM) is an electrical motor with simple and robust structure [1]. Its stator and rotor are made of laminated steel with high magnetic permeability. The stators are wound with coils while the rotor has no magnet or coil attached.

SRM runs by reluctance torque. When the current is applied on a stator winding, the corresponding rotor magnetic tries to minimize reluctance path by aligning the rotor pole with the nearest stator pole. To maintain this rotation, an electronic control system is needed to switch on the successive stator poles. Besides, SRM usually uses an electronic position sensor or resolver to determine the rotor shifting angle to turn on and switch off the stator windings.

1.1.1. THE BASIC STRUCTURE OF SRM

As shown in Fig. 1.1, a switched reluctance machine system consists of four main parts: the switched reluctance motor, power converter, controller, and sensors. The controller generates the gate signal to the power converter. Power converter provides energy to SRM. Current and position sensors are used to provide feedback signals to the controller.
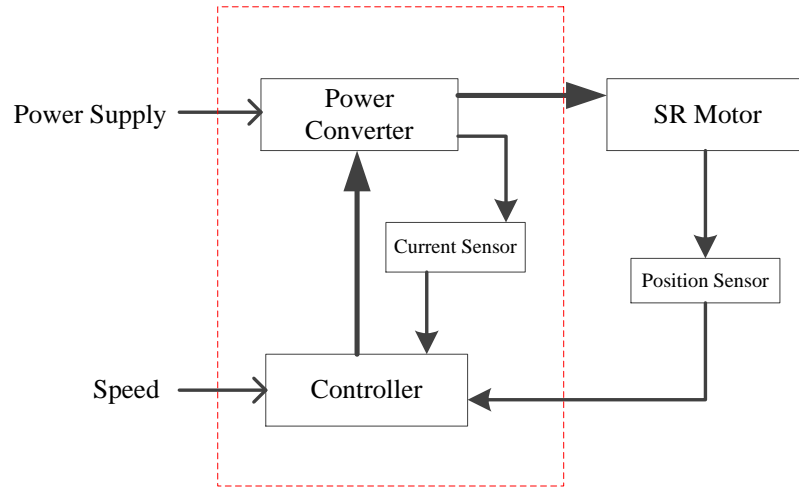
Fig. 1.1 Basic configuration of SRM drive.

The structure of SR machine depends on the number of stator poles and rotor poles. As shown in Fig. 1.2 [2], the SRM has salient poles on both stator and rotor and adopts multiphase concentrated windings on the stator. However, there is no copper winding or permanent magnet (PM) piece on the rotor.

There are two basic SR machine topologies: three phase 6/4-topology and four phase 8/6-topology. The former topology has advantages of low cost and better performance at high speed while the latter topology has lower torque ripple and acoustic noise than the former one [3] [4]. TABLE 1.1 describes some topologies design of SR machine, including the stator number N_s, the rotor number N_r, the step angle θ_{step} and the phase number of operation q [5] [6] [7].
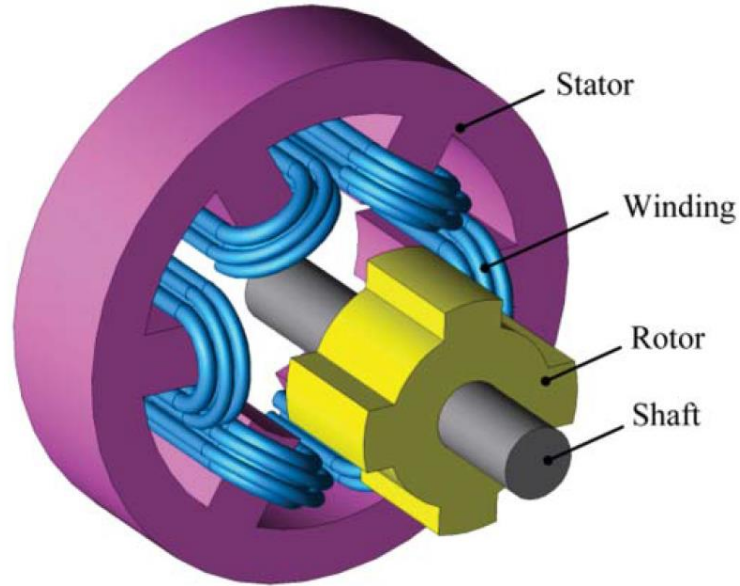
Fig. 1.2 SR machine structure.

TABLE 1.1 SRM structure topology design

m	3					4		5			6
N_s	6	6	12	18	24	8	16	10	10	10	12
N_r	4	8	8	12	16	6	12	4	6	8	10
$\theta_{step}/(°)$	30	15	15	10	7.5	15	7.5	20	12	9	6
q	1	1	2	3	4	1	2	1	1	1	1

1.1.2. CONVERTER TOPOLOGY

The torque production of the SRM is independent of the direction of current. Therefore, the power converter of SRM only needs to provide unidirectional current.

3

The converter is a critical part of the SRM drive system [8]. Generally, an ideal converter topology has to have features such as higher efficiency, faster excitation time, fast demagnetization, high power, and fault tolerance.

There are several converter topology types with different number of switches. For example, full bridge converter topology has four switches for each phase. Asymmetric bridge converter topology has two switches for each phase. R-dump converter topology has one switch for each phase. C-dump converter has one switch for each phase plus an additional switch for all phases [9]. Although the mentioned topologies are commonly applied to different applications, the asymmetric bridge topology is the most popular one and is widely used. Therefore, in this thesis, researches are based on the asymmetric bridge topology.
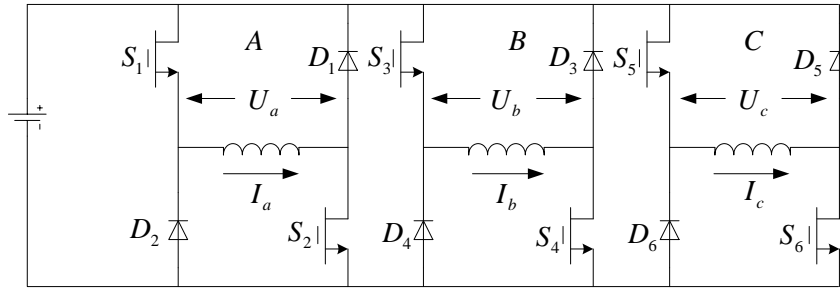
Fig. 1.3 Asymmetric converter topology.

As shown in Fig. 1.3, asymmetric converter topology uses two switches and two diodes per phase. Short-through problem is eliminated by using this converter. And each phase is independent from other phases.

There are three operation modes of this converter topology, which are defined as magnetization mode, freewheeling mode, and demagnetization mode [10]. As shown in Fig. 1.4, the current direction of three modes is marked by the red arrow. By turning on switches S_1 and S_2, phase A is energized by the voltage source, and the phase current starts to increase. This process is called magnetization. By only turning off S_1 while holding on S_2, the diode D_2 is conducted, and the voltage supply is cut off. This process is called freewheeling, and current will slowly decrease during this period. When both switches S_1 and S_2 are turned off, the diodes D_1 and D_2 are conducted, and the negative voltage is applied on the phase winding. This process is called demagnetization. Phase current will dramatically drop under the demagnetization voltage. The current waveform is shown in Fig. 1.5.

(a) Magnetization   (b) Freewheeling   (c) Demagnetization
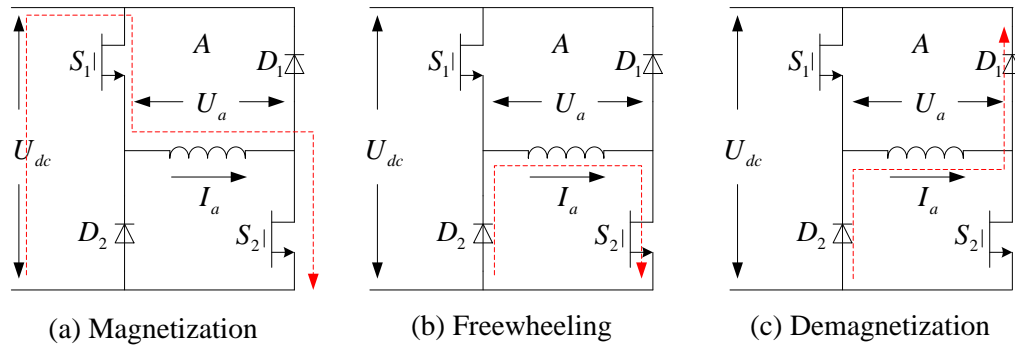
Fig. 1.4 Operation modes of asymmetric converter topology.

5
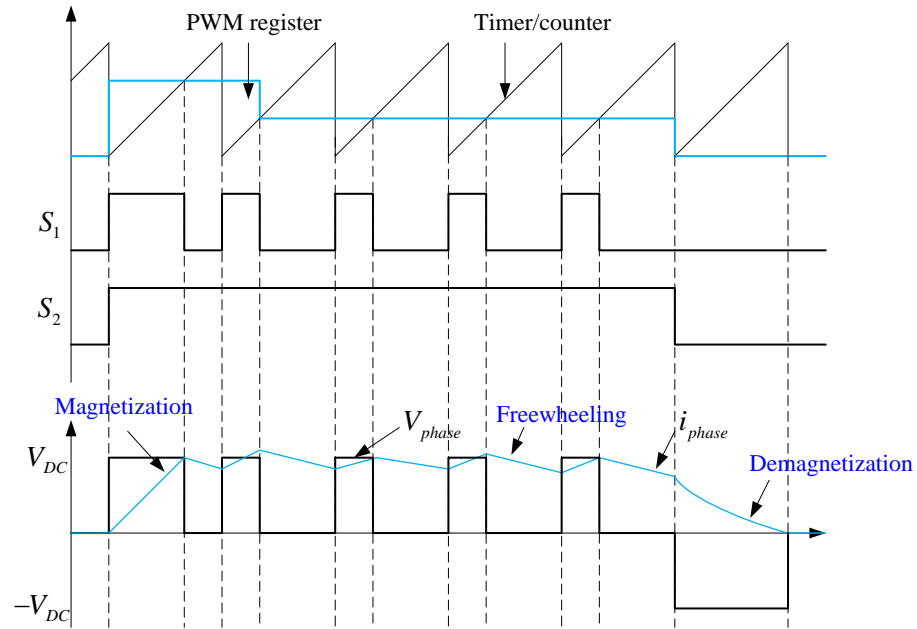
Fig. 1.5 Current waveform of three operation modes.

According to what is mentioned above, this topology has a dominant advantage of the control flexibility over others, and is more suitable for SRM drive system with high power, high voltage, and fewer phases.

1.1.3. ADVANTAGES AND DISADVANTAGES OF SRM

To apply the SRM drive to the industry field, the advantage and limits of switched reluctance motors have to be figured out. The benefits of switched reluctance motors can be summarized as following [11] [12].

6

a. The structure is simple, rugged, and low-cost. There is no magnet or coils attached on the rotor, making it suitable to operate at high or ultra-high speed. And the whole system has fast dynamic response due to the low inertia. The windings of stators are concentrated coils, which makes assembling and repairing easier than other type of machines.

b. The direction of current doesn't affect the direction of torque.

c. Asymmetric half bridge converter eliminates the short-through problem.

d. The flux-linkage of the phases are independent, which improves the reliability and fault-tolerant of the whole system.

However, the limitations of the applications of SRM cannot be ignored.

a. Higher current rating for power converter.

b. Instant torque ripple is significant, along with the problem of acoustic noise and vibration.

c. More terminals than conventional machine.

d. Converter is needed to drive.

e. An external position sensor is required for commutation and current control, which increases cost and reduces reliability.

The last disadvantage of SRM contributes to the development of position sensorless control of SRM [13].

1.2. OPERATION PRINCIPLE OF SRM

According to the principle of electromechanical energy conversion, SRM can be regarded as the system with electric input and mechanical output, and magnetic field connects the input and output. Neglecting the mutual inductance and iron loss, the electromechanical energy conversion of *m* phases SR machine is shown in Fig. 1.6.
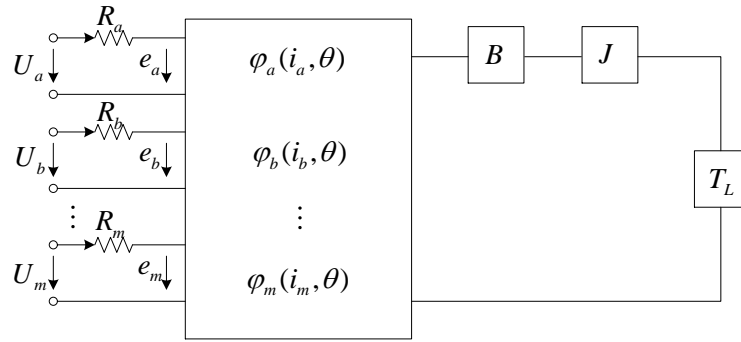
Fig. 1.6 Electromechanical energy conversion.

Where T_e, T_L, B, and J are electromagnetic torque, load torque, combined friction coefficient of motor and load, and combined moment of inertia of the motor respectively. U_k, i_k, R_k and e_k are phase voltage, phase current, phase resistance and phase induced electromotive force respectively. φ_k is the flux-linkage which is related to phase current and rotor position.

According to Faraday's electromagnetic induction law,

$$e_k = -\frac{d\varphi_k}{dt} \ , \ k = a,b,\ldots,m \tag{1.1}$$

Based on the principle of energy conversion, three basic equations to describe the system dynamic, including voltage, torque and mechanical, are introduced [2][14].

1.2.1. VOLTAGE EQUATION

According to the basic elementary equivalent circuit for SRM system, the voltage equation can be derived by neglecting the mutual inductance between phases.

$$U_k = R_k i_k - e_k = R_k i_k + \frac{d\varphi_k}{dt} \tag{1.2}$$

Where phase flux-linkage can be denoted as the product of phase inductance and phase current.

$$\varphi_k(i_k,\theta) = L(i_k,\theta)i_k \tag{1.3}$$

Due to the inherent nonlinearity of flux-linkage, phase inductance is a function of phase current. And the phase inductance varies with rotor position.

$$U_k = R_k i_k + \frac{\partial\varphi_k}{\partial i_k}\frac{di_k}{dt} + \frac{\partial\varphi_k}{\partial\theta}\frac{d\theta}{dt} = R_k i_k + (L_k + i_k\frac{\partial L_k}{\partial i_k})\frac{di_k}{dt} + i_k\omega\frac{\partial L_k}{\partial\theta} \tag{1.4}$$

Where ω is the angular speed.

9

In (1.4), the first item of the right equation is the resistance voltage drop of the *kth* phase; the second item is the voltage drop on the phase winding; the third item is back EMF of the SR machine. The equivalent circuit model is shown in Fig. 1.7 [15].
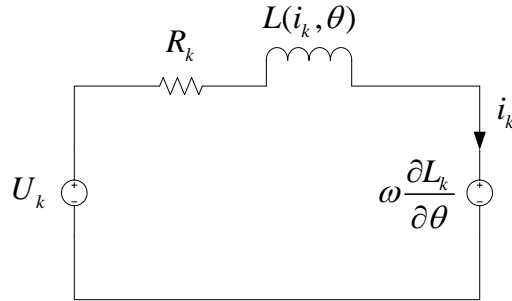
Fig. 1.7 Equivalent circuit model of SR machine.

1.2.2. TORQUE EQUATION

The flux-current curves for the unaligned and aligned position are plotted as shown in Fig. 1.8. $\theta = \theta_1$ represents the unaligned position, and $\theta = \theta_2$ represents the aligned position. Due to the magnetic saturation property at aligned position, the curve for θ_2 is nonlinear. While the characteristic for the unaligned position is almost linear [16].

The energy of windings can be denoted as

$$W = \int_0^{\varphi} i(\varphi, \theta) d\varphi \tag{1.5}$$

Then the co-energy can be written as

$$W^{'} = \int_0^i \varphi di = \int_0^i L(\theta,i)idi \qquad (1.6)$$
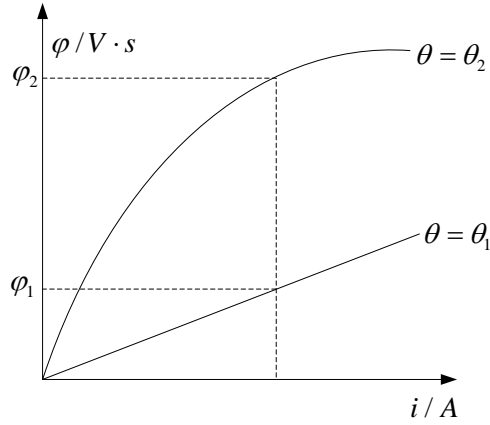
Fig. 1.8 Flux-current characristics.

The torque produced by SRM is incremental change of co-energy with the rotor position [17].

$$T_e = \frac{\partial W^{'}(\theta,i)}{\partial \theta} \qquad (1.7)$$

By combining (1.6) and (1.7) , the torque can be rewritten as

$$T_e(i,\theta) = \int_0^i \frac{\partial \varphi(i,\theta)}{\partial \theta} di = \int_0^i \frac{\partial L(i,\theta)}{\partial \theta} idi \qquad (1.8)$$

1.2.3. MECHANICAL EQUATION

According to Newton' mechanics laws, the mechanical equation for modeling consists of inertia, friction, and load torque. The mechanical equation determines the speed equation as following.

$$T_e = B\omega + J\frac{d\omega}{dt} + T_L \tag{1.9}$$

$$\omega = \frac{d\theta}{dt} \tag{1.10}$$

Where T_e is the torque of each phase, T_L is the load torque, B is viscous damping coefficient, and J is the combined rotor and load inertia.

1.2.4. ROTATION PRINCIPLE

As defined in [18], the torque of reluctance machine is produced by the tendency of its movement from current position to the position where the inductance of the excited winding is maximized. A three-phase 6/4 SRM is regarded as an example in this case. As shown in Fig. 1.9, rotor pole 1 is aligned with phase C at this moment. Then by exciting the phase A windings, the rotor tends to rotate clockwise to minimize the reluctance of flux-linkage path. When rotor 2 and 2' are aligned with stator pole A and A', the flux-linkage and inductance reach to the maximum value. And then, by turning off the switches of phase A and turning on the switches of phase B, the phase B is excited and rotor 2 starts to be aligned with phase B. In the same way, when rotor 2 and 2' are

aligned with the phase B, by switching off the phase B and switching on the phase C, the phase C is excited and rotor continues to rotate to align with the phase C. In this way, the rotor would rotate clockwise continuously. On the contrary, by conducting the phase windings in the sequence of A-C-B, the rotor rotates anticlockwise [2].
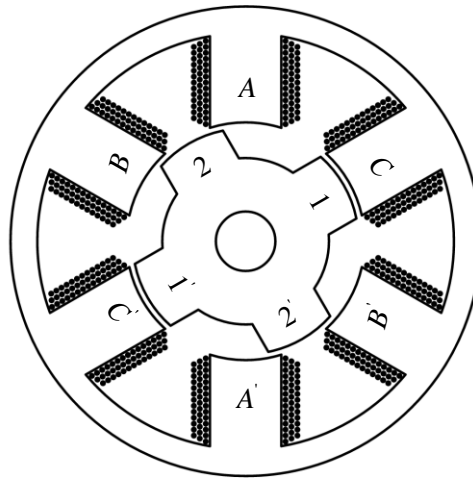
Fig. 1.9 Rotation principle of SRM.

1.2.5. SPEED CONTROL

Generally, there are two main control schemes for speed control of SR machines: the current chopping control (CCC) / voltage pulse-width modulation (PWM) and the angular position control (APC) [2]. The CCC/PWM is suitable for low speed or medium speed operation and APC usually be used for high-speed operation. The speed boundary between these two schemes is called the base speed ω_b. The back EMF is equal to the DC source voltage at this speed.

13
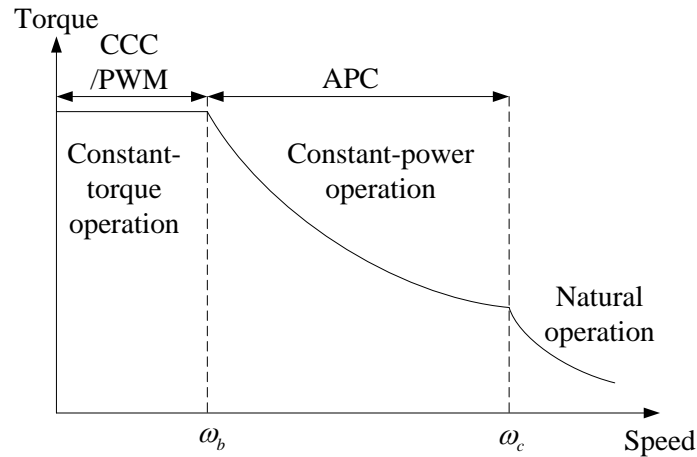
Fig. 1.10 Torque-speed capability of SR motor.

As shown in Fig. 1.10, this figure depicts the torque-speed capability of the SR motor covering all operation regions [2]. When the motor operates at low speed, namely, below the base speed, the back EMF is lower than DC source voltage, so that the torque keeps constant in this region. Once the speed exceeds the base speed, the back EMF is higher than the DC source voltage. The torque will decrease monotonously with the increase of speed until the speed reaches the critical speed of SR machine ω_c. The power maintains constant in this region. Beyond the critical speed of the motor, the torque drops dramatically, and the motor offers natural operation mode then.

The so-called CCC/PWM is kind of hysteresis control to control these switches. The phase currents or voltages have to be regulated at a particular value with predetermined upper and lower boundaries in the constant-torque operation region. For example, the

control scheme of CCC is shown in Fig. 1.11. Since the rise time or fall time is inevitable when building up the current or demagnetization, it is necessary to turn on and turn off the switches in advance for a certain angle. And when the phase shall be turned on or turned off is determined by phase current and rotor speed.
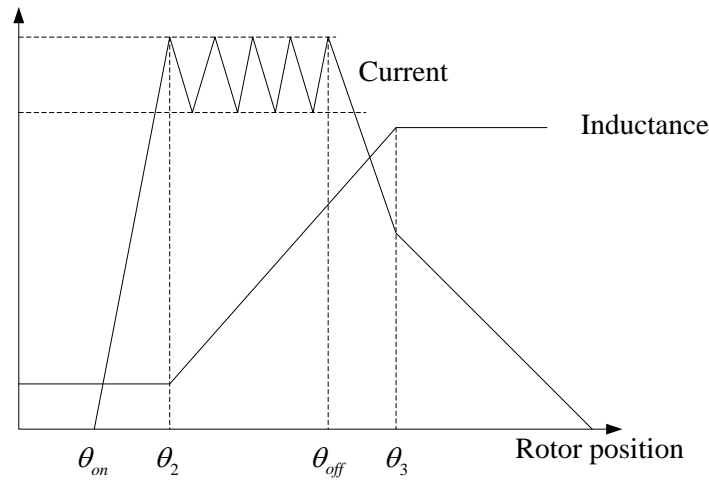
Fig. 1.11 Current chopping control for constant-torque operation.

Both CCC and PWM can be used to control the excited voltage on the windings to obtain the constant torque operation characteristics. In CCC mode, the current on the phases can be limited in a hysteresis band to control the conduction time of the DC source voltage on the phases. Then, the output torque can be controlled by changing the value of hysteresis band.

The advantage of this technique is inherent over-current protection feature [19]. This method can also be called Current PWM. In Voltage PWM mode, although the current on

each phase cannot be controlled directly, the output torque can be controlled by modulating the width of conducting time on each phase to change the average value of excited voltage.
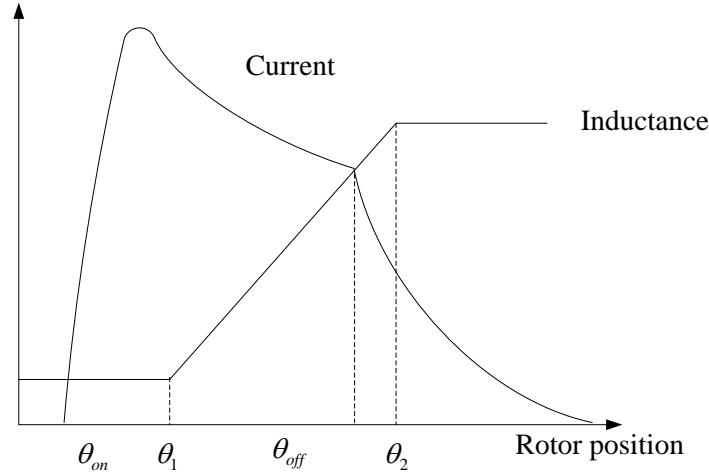
Fig. 1.12 Angular position control for constant-power operation.

In the constant-power operation region, since the back EMF is high than the DC-source voltage, the phase current is limited by the back EMF, operating at single pulse mode and never reaching the rated current. As shown in Fig. 1.12, in order to impulse the current into the phase winding, the turn-on angle of the switches needs to be well in advance of θ_2. When increasing the rotor speed, the back EMF will also increase, thus leads to the decrease of phase current as well as the torque. So the larger advancing of turn-on angle is required at high rotor speed, which ensures the level of current before turning off the switches. And such advancing turn-on angle can also offer the capability of constant-

power operation since the torque drops inversely with the rotor speed. However, this advancing turn-on angle can no longer be ahead of θ_1 in Fig. 1.12, limited by the position of negative slope region of phase inductance. At the same time, the turn-off angle has to be advanced enough too, making sure that phase current will decay to zero before the following negative slope region of the phase inductance.

1.3.   LINEAR AND NONLINEAR MODEL OF SRM

1.3.1. LINEAR MODEL OF SRM

As shown in Fig. 1.13, neglecting the magnetic saturation, the variation of phase inductance is described when rotor move from unaligned position to aligned position[2]. The relevant rotor position and operation regions can be characterized in the following groups.
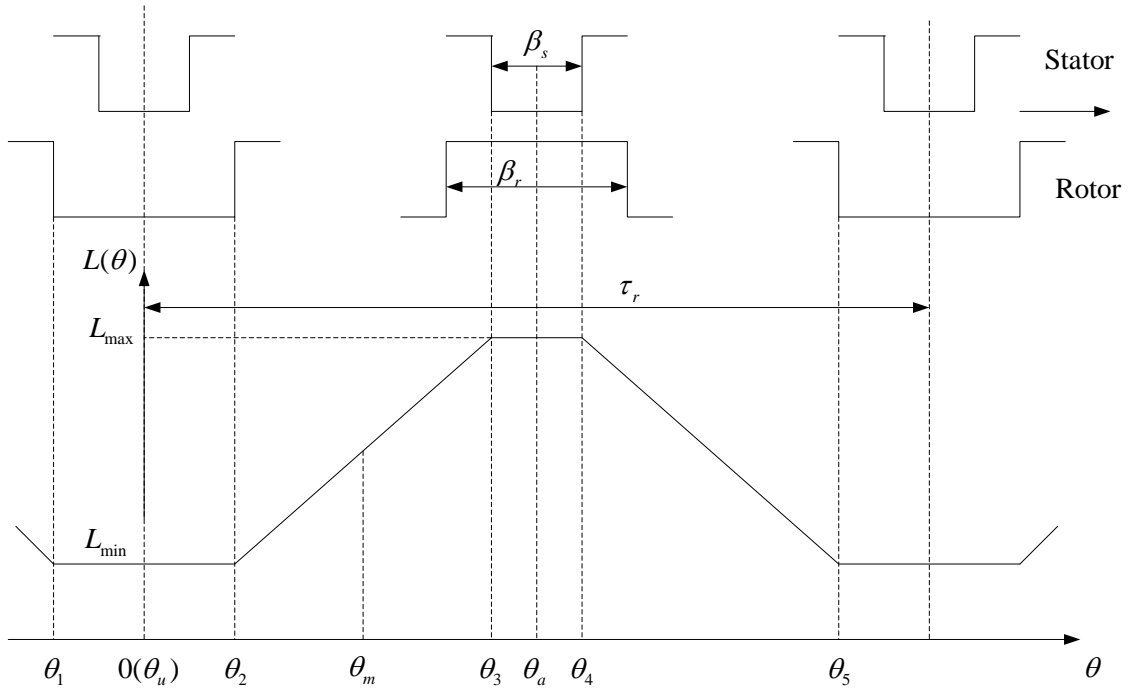
Fig. 1.13 Variation of phase inductance with rotor position.

β_s - stator pole arc;

β_r - rotor pole arc;

τ_r - rotor pole pitch, $\tau_r = 2\pi / N_r$, where N_r is the number of rotor poles.

Region 1 ($\theta_1 \rightarrow \theta_2$): $\theta_2 = (\tau_r - \beta_s - \beta_r)/2$

In this region, the stator and rotor are not overlapped, termed the unaligned position, so the inductance maintains at the minimum value L_{min}. There is no torque production in this region.

Region 2 ($\theta_2 \rightarrow \theta_3$) : $\theta_3 = \theta_2 + \beta_s = (\tau_r + \beta_s - \beta_r)/2$

In this region, the stator and rotor start to overlap, so the phase inductance linearly increases with rotor position. The incremental inductance on the rotor position is positive in this region, so a positive torque can be produced when applying a current to the windings. It should be noted that the polarity of the current has no influence on the polarity of the torque.

Region 3 ($\theta_3 \rightarrow \theta_4$) : $\theta_4 = \theta_3 + \beta_r - \beta_s = (\tau_r + \beta_r - \beta_s)/2$

In this region, the stator and rotor are entirely overlapped, termed aligned position, so the phase inductance keeps at the maximum value L_{max}. Since there is no change of phase inductance, the torque cannot be produced.

Region 4 ($\theta_4 \rightarrow \theta_5$) : $\theta_5 = \theta_4 + \beta_s = (\tau_r + \beta_s + \beta_r)/2$

In contrast to the region 2, the stator and rotor start to reduce the overlapping region from θ_4, so the phase inductance linearly decreases with the rotor position. The incremental inductance on the rotor position is negative, so produced torque is also negative when applying a current into windings.

Then the relationship between rotor position and phase inductance start to repeat the above regions.

19

For SR machine, the linear model of phase self-inductance can be described by the following equations

$$L(\theta) = \begin{cases} L_{min} & \theta_1 \leq \theta < \theta_2 \\ K(\theta - \theta_2) + L_{min} & \theta_2 \leq \theta < \theta_3 \\ L_{max} & \theta_3 \leq \theta < \theta_4 \\ L_{max} - K(\theta - \theta_4) & \theta_4 \leq \theta < \theta_5 \end{cases} \tag{1.11}$$

Where $K = (L_{max} - L_{min})/(\theta_3 - \theta_2) = (L_{max} - L_{min})/\beta_s$.

According to the Fourier series transformation, the self-inductance of the active stator can be represented by three terms whose coefficients depend on the current given as [20][21],

$$L(i,\theta) = L_0(i) + L_1(i)\cos(N_r\theta) + L_2(i)\cos(2N_r\theta) \tag{1.12}$$

Where N_r is the number of rotor poles,

$$\begin{cases} L_0 = \dfrac{1}{2}[\dfrac{1}{2}(L_a + L_u) + L_m] \\ L_1 = \dfrac{1}{2}(L_a - L_u) \\ L_2 = \dfrac{1}{2}[\dfrac{1}{2}(L_a + L_u) - L_m] \end{cases}$$

Where L_a, L_u and L_m are the inductance at aligned position, unaligned position and midway between aligned and unaligned position, respectively.

These three inductances can be expressed as a function of phase current at follows.

$$\begin{cases} L_u = L(\theta = 0^\circ) \\ L_m = L(\theta = \dfrac{\pi}{2N_r}) = \displaystyle\sum_{n=0}^{j} b_n i^n \\ L_a = L(\theta = \dfrac{\pi}{N_r}) = \displaystyle\sum_{n=0}^{j} a_n i^n \end{cases} \tag{1.13}$$

Where j is the degree of approximation, and coefficients a_n and b_n are determined by the curve fitting method. The inductance at unaligned position is assumed to be independent of current. To develop the self-inductance model, the measurements of inductance of L_a, L_u and L_m are required. Therefore, by obtaining the finite element analysis data at three different rotor positions, the self-inductance model of SRM is derived.

1.3.2. NONLINEAR MODEL OF SRM

Considering nonlinearity caused by the high saturation of flux-linkage, a more accurate model has to be set up to achieve higher control accuracy. Therefore, nonlinear model have to be studied [22]. There are several ways to set up the nonlinear model, including finite element method, artificial neural network, and analytical method.

The state-space differential equations of the SRM are presented in the following equations.

$$\frac{d\varphi_n}{dt} = v_n(t) - i_n(t)r_n \tag{1.14}$$

$$\frac{d\theta}{dt} = \omega(t) \tag{1.15}$$

$$\frac{d\omega}{dt} = -\frac{B}{J}\omega(t) + \frac{1}{J}\sum_{n=1}^{N_{ph}}T_n(\theta, \lambda_n) - \frac{1}{J}T_L(t) \tag{1.16}$$

Where θ and ω are the rotor position and speed respectively, T_n is torque of each phase, T_L is the load torque, N_{ph} is the number of stator phase. Without loss of generality, [23] proposed a flux-linkage model,

$$\varphi_j = \varphi_{sat}(1 - e^{-i_j f_j(\theta)}) \ , j = 1,2,3...m \tag{1.17}$$

Where φ_{sat} is the saturated flux linkage, i_j is the position current of the phase j , and the $f_j(\theta)$ can be expressed by a positive Fourier series expansion.

$$f_j(\theta) = a + \sum_{n=1}^{\infty}[b_n \cos(nN_r\theta - (j-1)2\pi/m) + c_n \sin(nN_r\theta - (j-1)2\pi/m)] \tag{1.18}$$

From (1.7) and (1.8), the instantaneous torque of the phase j can be expressed as

$$T_j(\theta, i_j) = \frac{\varphi_{sat}}{f_j^{\ 2}(\theta)}\frac{df_j(\theta)}{d\theta}\left\{1 - \left[1 + i_j f_j(\theta)\right]e^{-i_j f_j(\theta)}\right\} \tag{1.19}$$

Since the value of bracket $\{\bullet\}$ in (1.19) is between 0 and 1, the sign of $\{\bullet\}$ is positive.

Then the sign of torque is determined by the sign of $df_j(\theta)/d\theta$. Except the load torque,

all the nonlinear terms can be accurately modeled with equations (1.17) to (1.19), and this

model has merits like low computational efforts and fast operation speed.

Establishing a 3D look-up table is another effective way to set up a nonlinear model.

Since the flux-linkage and torque are all related to the phase current and rotor position,

the data of $\varphi(i,\theta)$ and $T(i,\theta)$ characteristic can be obtained from FEA and experiment,

and then stored in tabular forms. The nonlinear modeling of SRM can be described by

$$\varphi = \varphi(i,\theta) \tag{1.20}$$

$$T = T(i,\theta) \tag{1.21}$$

This modeling is very popular among the SRM control systems due to its simplicity. The

more data preserved in the look-up table, the more accurate model will be.

1.4. MOTIVATION

As is known, SRM drive system relies on position feedback. However, the existence of

position sensors will weaken the advantages of SRM like robustness and fault-tolerant

ability, and the reliability of high-speed operation will also be reduced. So, rotor position

sensorless detection methods have to be applied to improve the performance of SRM.

In this thesis, the pulse injection method and sliding-mode observer method are applied at low-speed and high-speed operation, respectively. As for the pulse-injection method, the phase inductance saturation region is considered. The slope of inductance saturation region and linear decreasing region are respectively calculated to estimate rotor position in a more precise way. Based on the previous SMO sensorless control method, a new position sensorless control method with the estimation of speed acceleration is proposed. This third order observer is aimed at reducing the dynamic error and improving the estimation accuracy. A method to design the SMO gains is also introduced, and the stability of the system is verified with the design of these SMO gains.

1.5. OUTLINE OF THIS THESIS

The rest of this thesis is organized as follows:

Chapter 2 briefly introduces state-of-the-art position sensorless methods which can be applied to SRM drive system. In chapter 3, high-frequency pulse injection method is presented in detail, including the initial position detection and sensorless control at low-speed operation. Sliding mode observer, which is suitable for high-speed operation, is introduced in Chapter 4. And in this chapter, the sliding mode control, and sliding mode observer are respectively discussed.

Simulation verification and experiments results are presented in Chapter 5 and Chapter 6, respectively. These results demonstrate that the proposed method can be applied for SRM sensorless control with desirable accuracy.

Finally, Chapter 7 draws the conclusions from the work done in this thesis and discusses further research possibilities in the future.

Chapter 2

POSITION SENSORLESS CONTROL METHODS

2.1. INTRODUCTION

Rotor position detection is of significant importance for SRM control. In general, external position sensors are mounted on the shaft, like absolute encoders and magnetic sensors, and they are used to detect the rotor position and give feedback information to the controller [24]. However, these position sensors not only reduce the reliability of SRM drive system in harsh environments but also increase the cost. Besides, they will significantly affect the reliability and robustness of the operation of SRM. Therefore, in order to achieve efficient control and operation, position sensorless control becomes a promising technique for SRM drives.

In the past thirty years, various sensorless control methods for SRM drives have been reported. In general, the classification of these sensorless control methods can be divided into three categories: hardware-intensive methods, data-intensive methods and model-based methods [25]. Different methods have different requirements. Hardware intensive methods need an external circuit to generate signal injection. Data intensive methods

require a large amount of memory space to store look-up table which contains the information of the magnetic characteristic of SRM. Model-based methods call for a microprocessor with high operation speed.

A diagram of three categories and corresponding example methods are given in Fig. 2.1. The ideal sensorless method is detecting the rotor position by only using the terminal measurements without any additional hardware or memory space and is suitable for entire speed range from standstill to ultra-high speed with high operation accuracy [25].

For the SRM drive system, it is clear that the mechanical time constant is much larger than its electrical time constant, which is the main idea of all the sensorless techniques. Therefore, by solving the voltage equation (1.2) and (1.4), the rotor position can be decoded from the information which is stored in the form of flux-linkage, inductance, and back-EMF [26].

Due to the fast development of DSP technology, several sensorless techniques can be realized by using DSP controllers. Furthermore, the high operation speed capability and computational power also contribute to developing new sensorless method without requirements of external hardware or memory. As the result, the model-based sensorless methods like sliding-mode observer are effectively and efficiently implemented and fulfilled by utilizing the DSP controller.
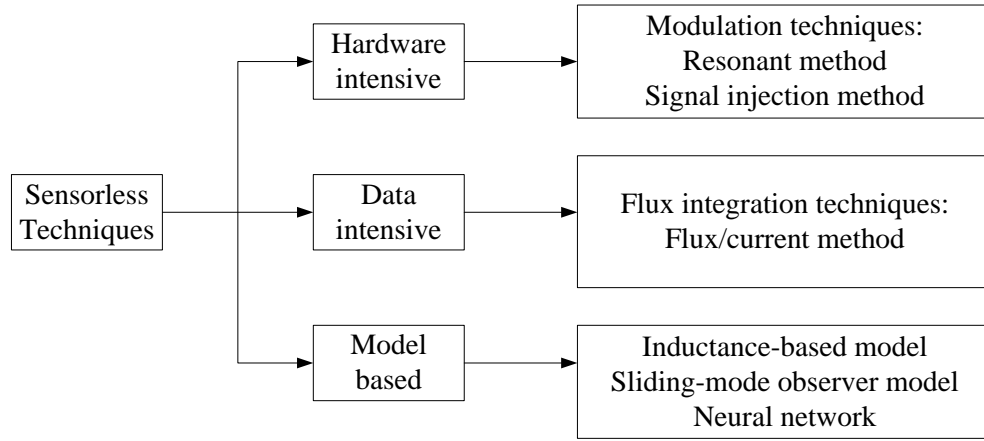
Fig. 2.1 Classification of various sensorless control schemes for SRM.

2.2. REVIEW OF SEVERAL BASIC METHODS

2.2.1. FLUX/CURRENT METHOD

The flux-current method was firstly proposed by Lyons in [27]. The main idea of this approach is to utilize the measurements of phase flux-linkage and phase current to determine the rotor position. To realize such commutation control without any shaft position sensor, the 3-D look-up table which stores the relationship of flux-linkage, phase current, and rotor position is demanded. However, the phase flux-linkage cannot be measured directly, (1.2) has to be reversed to get the flux-linkage by measuring the phase voltage and phase current.

$$\varphi(t) = \int (U_m - i_m R)dt \tag{2.1}$$

Where U_m and i_m are measured voltage and current respectively, and R is the phase resistance. By neglecting the mutual flux-linkage, the flux-linkage can be obtained by integrating the voltage applied on the phase windings. To realize this position sensorless technique, a family of flux-linkage and current characteristics at various rotor positions from unaligned position θ_u to aligned position θ_a has to be obtained in advance by finite element analysis or experiments. The expression of these characteristics can be written as follows,

$$\varphi = \varphi(\theta, i) \tag{2.2}$$

$$\theta = \theta(\varphi, i) \tag{2.3}$$

Since the 3-D look-up table contains the relationship of flux-linkage, phase current and rotor position, the rotor position can be acquired given the other two conditions. More rotor positions need to be tested in advance to depict the specified curves to get more accurate position sensorless detecting results.

However, there are lots of data need to be stored, which requires a significant amount of memory space. Besides, the above method also demands high computational speed which will increase the burden of the microcontroller. Based on the flux/current approach, an improved algorithm has been developed in [28]. Predefining the control signal rising edge of one phase as 0°, the corresponding degree of control signal rising and falling edges of all phases can be defined. Only the flux-current characteristics at these specific

29

commutation positions are needed in this sensorless method. By comparing the measured

flux-linkage with the flux-linkage obtained at these particular positions, the rotor position

can be obtained. The advantage of this approach is that only several rotor positions need

to be detected which significantly reduce memory space and computational power. The

schematic of this method is shown in Fig. 2.2.
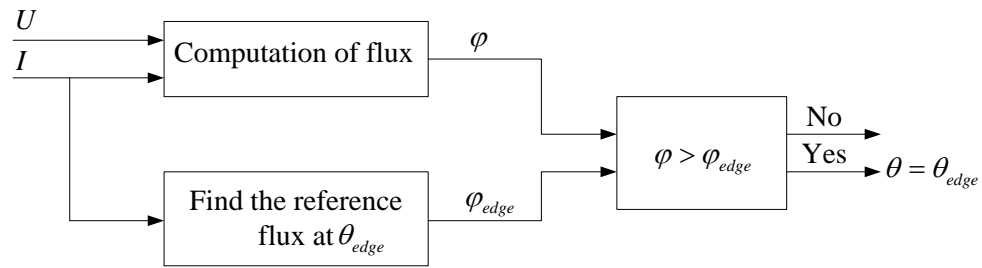
Fig. 2.2 Schematic of improved flux-current method.

Besides, a high-resolution position estimator was proposed in [29]. This method adds a

corrector variable to the primary flux-current sensorless control system, and the corrector

variable can be chosen as either flux-linkage or current, which respectively comprise the

flux observer or current observer, and efficiently contributes to reducing the loss in

accuracy and real-time computation. The main improvement of this method compared

with the above two methods is that the most accurate phase to estimate the rotor position

can be chosen. Moreover, it is suitable for a wide speed range application in four

quadrants, and the load torque transients are also permitted. However, since the real-time

application of this method is based on DSP platform, the real-time calculation is also

limited by the operation speed of DSP. Therefore, the development of more powerful and cheaper DSP is also critical to realize the implementation of this method.

2.2.2. INDUCTANCE BASED METHOD

The inductance-based methods mainly rely on a dynamic model of the SRM drive system to determine the rotor position by utilizing the relationship of the phase inductance, phase current and rotor position [30]. Similar to the flux/current method, this method only needs to measure the real-time current and voltage of active phase. By solving the dynamic equation of the active phase, the rotor position information can be obtained. This dynamic model doesn't need large memory space to store experimental data, and can be easily updated when the magnetic characteristics have changed. However, this method is only suitable for high-speed operation. New analytical model based on this inductance model is proposed in [31]. Combining the other model or method proposed in [27] and [32], the new model can run the SRM from standstill state. The succinct introduction of the new analytic model is as follows.

Based on the voltage equation (1.4), the phase voltage can be simplified by neglecting the term including ω at standstill or low speed [31].

$$U_k = R_k i_k + [L_k(i_k, \theta) + i_k \frac{\partial L_k(i_k, \theta)}{\partial i_k}]\frac{di_k}{dt} = R_k i_k + l(i_k, \theta)\frac{di_k}{dt} \qquad (2.4)$$

where $l(i_k, \theta)$ represents the phase incremental inductance.

Then the phase incremental inductance can be denoted as.

$$l(i_k, \theta) = L_k(i_k, \theta) + i_k \frac{\partial L_k(i_k, \theta)}{\partial i_k} = \frac{U_k - R_k i_k}{\frac{di_k}{dt}} \tag{2.5}$$

The phase incremental inductance model can be developed based on the self-inductance model (1.12). So the functional relationship of incremental inductance, phase current, and rotor position can be expressed below.

$$l(i, \theta) = l_0(i) + l_1(i)\cos(N_r\theta) + l_2(i)\cos(2N_r\theta) \tag{2.6}$$

Where

$$\begin{cases} l_0 = \frac{1}{2}\left[\frac{1}{2}l_p + l_q\right] + L_0(i) \\ l_1 = \frac{1}{2}l_p + L_1(i) \\ l_2 = \frac{1}{2}\left[\frac{1}{2}l_p - l_q\right] + L_2(i) \end{cases}$$

Where

$$l_q = l(\theta = \frac{\pi}{2N_r}) = \sum_{n=0}^{j} nb_n i^n, l_p = l(\theta = \frac{\pi}{N_r}) = \sum_{n=0}^{j} na_n i^n$$

Then substituting (2.6) into (2.5), the voltage equation can be rewritten as,

32

$$\frac{U - Ri}{\frac{di}{dt}} = l_0(i) + l_1(i)\cos(N_r\theta) + l_2(i)\cos(2N_r\theta) \tag{2.7}$$

U, R and i can be measured in advance or by sensors, and $\frac{di}{dt}$ can be calculated using phase current data. Therefore, the rotor position θ can be obtained once the phase current is sampled. So the key point of this sensorless method is that rotor position must have one-to-one relationship with the phase incremental inductance at a given phase current. However, sometimes, the one-to-one relationship will lose its unique property when increasing the phase current for a single phase. Then, the solution to this situation is changing the detecting phase for different rotor position region. Besides, finding a proper startup method at standstill position is also very important.

2.2.3. SIGNAL INJECTION METHOD

When the SRM operates at low speed, the rotor position is estimated by injecting small current detection signals. These signals are inserted into idle phases to sense the rotor position. However, this method isn't suitable for high-speed operation [33].

There are two primary signal injection methods to detect the rotor position. One is high-frequency pulse injection method, and the other one is low-amplitude sinusoidal voltage method.

The high-frequency pulse injection methods inject several short-period diagnostic voltage pulse signals to an idle phase to obtain the rate of change of the phase current. Then the phase inductance can be obtained. The rotor position can be obtained by the pre-stored phase inductance vs. rotor position characteristics [34] [35]. However, since the diagnostic pulse is generated from main converter, the current may produce the negative torque which will affect the operation of the SRM. Besides, the injected current takes time to decay to zero, and the next sensing pulse cannot be injected to the phase before the previous one falling to a negligible level. This situation severely affects the frequency of diagnostic pulse as well as the sampling, resulting in unsuitable for detecting rotor position when SRM is operating at high-speed level. Considering this main drawback, [36] makes some improvements, proposing a new approach by applying a single high-frequency pulse instead of the conventional one, which allows the application to detect the rotor position at high-speed. The duration of the diagnostic pulse is chosen and fixed at which the amplitude of the current is too small to generate the undesired negative torque. By integrating the current through the integrator, the output of integrator can be used to estimate the rotor position by comparing the results with the predefined look-up table.

Applying a small amplitude sinusoidal voltage to an inactive phase is also used as rotor position sensorless control method. Based on the phase and amplitude variation, the phase modulation (PM) and the amplitude modulation (AM) techniques are proposed in

[37]. When a sinusoidal voltage is applied to an idle phase, the current in the phase coil will change with the phase inductance which varies with the rotor position. Since the phase coil is in series with phase resistance and phase inductance varies with rotor position periodically, the angle between applied voltage and corresponding current changes periodically. The PM encoder technique and AM encoder techniques require the measurements of instantaneous phase angle and peak amplitude respectively. And then the instantaneous measurements pass to a demodulator to extract phase inductance information. The demodulator generates a signal of phase inductance which is a function of rotor position and then provides the signal to a converter where the rotor position can be obtained by inverting the function or a conversion table. Meanwhile, as for the demodulator part, PM encode technique uses zero crossing detectors for voltage and current to decode inductance information, and AM encodes technology to detect the envelope of modulated current signal which contains the phase inductance information. However, both of these two techniques need addition voltage source to supply the low-amplitude sinusoidal voltage. But this method has robust to switching noise and keep excellent track and accurate detection of rotor position.

2.2.4. FUZZY LOGIC AND NEURAL NETWORK

Since previous sensorless methods have limitations on operation conditions, such as ineffectiveness as high speed or standstill, and extra hardware or memory space, fuzzy logic based sensorless method can be used under all operating speeds and conditions.

There is no requirement of a mathematical model of the SR motor in this sensorless position scheme. The main idea of fuzzy logic is utilizing the self-learning system to learn the real-time motor characteristics. In this way, all the real-time issues can be considered to make the rotor position estimation more accurate, including saturation effects, mutual inductance, eddy currents and temperature variation [38]. The self-learning system mainly includes two parts, the static motor characteristics, and real-time operating conditions. And the study of latter is used to modify the static model with real-time issues. Besides, expert knowledge can be implemented to choose the best phase to estimate the rotor position when more than one phase is conducting. Consequently, the reliability of the scheme can be improved, and some measurements error can be overcome.

Artificial neural network (ANN) is another ideal candidate for position sensorless control considering the high nonlinear characteristics of SRM system. This method tries to simulate human brain to construct the model structures, including single neuron structure and multi-layer structure. These models can learn from experimental data or simulation to obtain the essential characteristics of the real system. The superior advantage of this learning ability is that it can generalize and induce characteristics to inputs containing irrelative data from previous examples or experience [39]. Proper training is necessary to obtain a model with high accuracy. The neural networks are feedforward networks, allowing signals are flowing from input to output in one direction. In order to improve the

dynamic stability, the output is connected to input by a delay line. Usually, the inputs of ANN training data are current and flux while the outputs are corresponding rotor position and speed [40]. The close-loop ANN system can successfully estimate rotor position.

Moreover, [41] proposed a novel approach of single neural PID control for sensorless rotor position estimation based on the radial basis function (RBF) neural network. RBF network is a three-layer feedforward neural network with linear neuron from the input layer to output layer. With the single neuron which has the ability of self-training and self-adaptive, the whole system has the advantage of structure simplicity, adaptability, and robustness. Training sample can be obtained from off-line training, and then on-line training can be used to adjust network connect weights according to the recursive least square. The on-line identification of system and on-line regulation of controller can improve the reliability and accuracy with excellent dynamic characteristics.

2.2.5. SLIDING MODE OBSERVER METHOD

Sliding mode observer is a novel method to detect rotor position and speed without using any position sensors. This method attracts people's attention due to its robustness and high reliability, especially for high-speed operation [42] [43]. The system characteristics, such as convergence speed and chattering, are controlled by observer gains. So appropriately selecting and designing the observer gains is a primary task when applying sliding-mode observer on rotor position sensorless control.

A novel sliding-mode observer was introduced in [44] with considering the influence of magnetic saturation, load disturbance, parameter variation and model errors. The sliding mode surface was selected as the difference between the estimated and measured phase currents in [44]. And switching gains, like flux-linkage gain, speed gain, and position gain, were determined to keep the system sliding on the sliding surface. In order to satisfy the sliding mode condition, the selection of the value of these gains was quantitatively analyzed and optimized to compensate the system disturbance and parameter variations. Finally, the accuracy of position estimation and the robustness of proposed method were successfully verified.

Different from the sliding mode surface selection in [44], the sliding mode surface was selected as the difference between measured flux-linkage and estimated flux-linkage in [1], [45], [46]. Based on the rotor position estimated from the sliding-mode observer, the method was further evaluated by considering the discrete-time formulation of the observer and analyzing the advantages and limitations of fixed-point and floating points computations in [1]. Besides, the speed feedback was used to modify the conduction angles during transient condition with considering the error of real-time implementation.

Since torque-ripple occurs in the simple control technique, a torque-ripple-minimization controller which suitable for a wide-speed-operation is added on the sliding-mode sensorless method in [45]. The guideline of designing the sliding-mode observer was proposed in [46]. To improve the robustness of the sliding-mode observer, the saturation

function is recommended to replace the sign function. The performance of the well-designed observer was evaluated concerning resolution of position estimation and errors in flux calculation.

Moreover, hybrid observer of CSMO (current sliding mode observer) and FSMO (flux-linkage sliding mode observer) is proposed in [47]. The results show that CSMO is suitable for low speed while FSMO works well for high speed, and hybrid observer shows better performance over wide speed range with high accuracy in rotor position and speed estimation. Furthermore, a four-quadrant sensorless scheme based on sliding-mode observer is considered as practical implementation issues [48] [49] [50]. This method can be used to estimate rotor position when speed command is toggled from one rotational direction to another through zero speed.

Chapter 3

PULSE INJECTION BASED SENSORELESS CONTROL METHOD

3.1. INTRODUCTION

As introduced in the Chapter 2, the signal injection sensorless method is suitable for low-speed operation. High-frequency voltage pulses are periodically injected into three phases in sequence to obtain the information of phase inductance. And then, the rotor position can be calculated based on the value of phase inductance [51]. Voltage pulses are applied to the phases with short duration Δt, and the corresponding current Δi is really small. Then the voltage equation can be simplified as

$$U_L \approx L(\theta)\frac{\Delta i}{\Delta t} \tag{3.1}$$

Where U_L is the voltage drop on the phase inductance, $L(\theta)$ is the phase inductance, Δi is the current difference before and after the injection, Δt is the injected pulse width, and θ is the rotor position. Then the phase inductance can be calculated by inverting (3.1) as

$$L(\theta) \approx U_L \frac{\Delta t}{\Delta i} \qquad (3.2)$$

By measuring the instantaneous phase current, the phase inductance can be calculated. And then phase inductance can be used for obtaining the real rotor position as well as detecting the initial rotor position. In order to clarify the correct sequence and position to inject the pulses, it is important to divide three phases inductance into different sectors.

For a three-phase SRM, the rotor position of 0° (electrical) is synchronized with aligned position of phase A (maximum inductance), and 180° (electrical) is synchronized with unaligned position of phase A (minimum inductance). Then the inductance profile of phase B and phase C are offset from phase A by 240° (electrical) and 120° (electrical), respectively. Then the inductance variation cycles repeat after 360° (electrical). When one phase is under conduction, one of the other two phases is used to detecting the rotor position. In section 1.3.1, the phase inductance is divided into 4 regions with the variation of rotor position. Among these regions, phase inductance increases in region 2 and decrease in region 4. Normally, the phase is used for sensing in region 4, and the phase is used for motoring in region 2. For the three phases SRM system, one electrical period can be divided into 6 sectors, and each sector has specific sensing and motoring phases, as shown in Fig. 3.1.

Motoring	B	C	C	A	A	B
Sensing	A	A	B	B	C	C
Sector	1	2	3	4	5	6
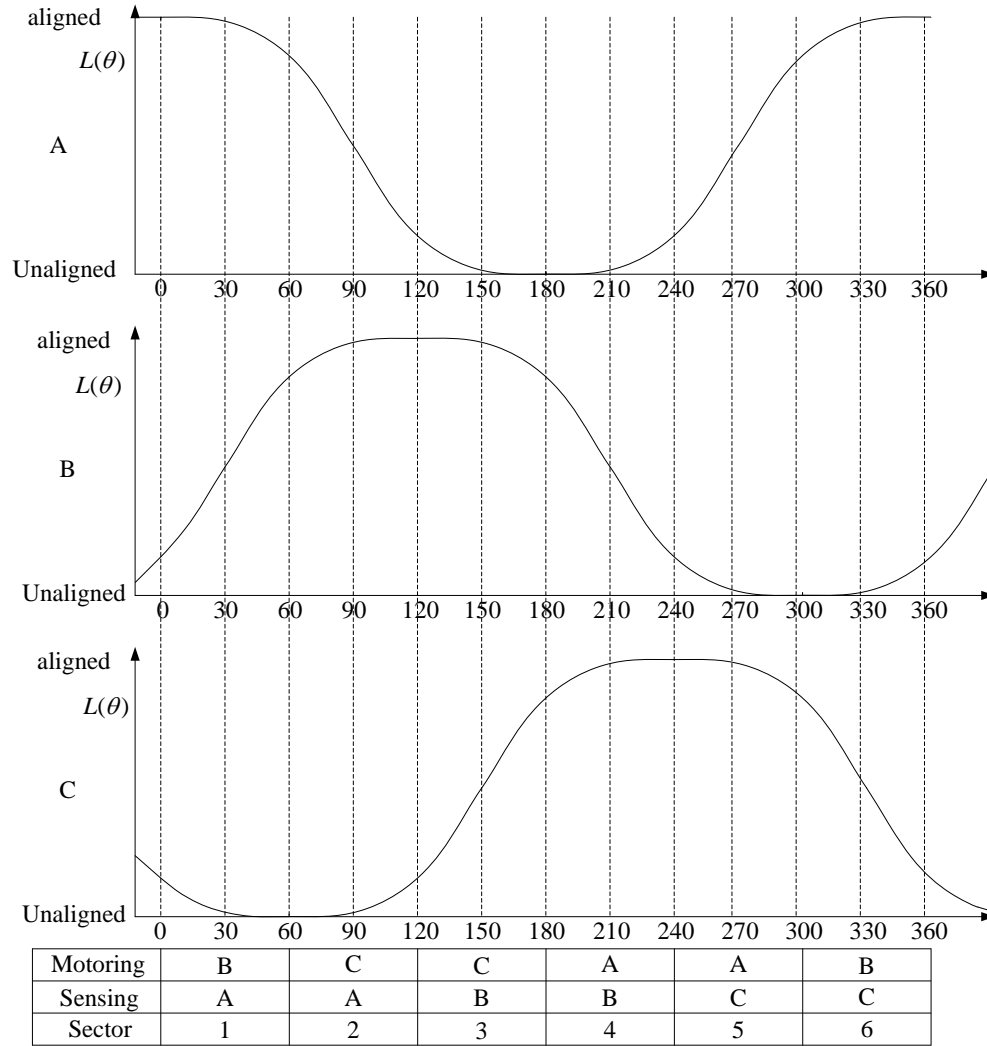
Fig. 3.1 Sectors definition in relation to phase inductance.

In sector 1, the inductance of phase A is decreasing from aligned position. In order to avoid the regenerating torque, phase A cannot be used for producing torque. However, this phase is best for sensing in this section. The inductance of phase B is increasing to

aligned position, while the inductance of phase C remains at the unaligned position. So phase B is used as active phase. In section 2, the inductance of phase C starts to increase from the unaligned position, and the inductance of phase B remain aligned position. In this section, the active phase changes from phase B to C. The inductance of phase A is still decreasing, and this phase is still used for sensing. The analysis of other sections is similar to section 1 and section 2.

The distribution of these sectors not only can be used to determine the initial rotor position, but also is a basic concept for estimating rotor position at low-speed operation using pulse injection method.

3.2.   SENSORLESS TECHNIQUE AT STANDSTILL

Since rotor position has to be estimated from zero speed, the initial rotor position has to be estimated for a smooth and reliable startup [52]. Two methods of estimating initial rotor position are reviewed in this section.

3.2.1.   REVIEW OF INITIAL POSITION ESTIMATION

A. Two current thresholds method

The two-threshold method is widely used to determine the initial position. The inductance of three phases has to be divided into different sectors by two thresholds of

each phase [33]. The low threshold determines when to change the active phase, and the high threshold determines when to change the sensing phase.

Voltage pulses are injected to the three phases simultaneously on all three phases of SRM. Since the current amplitude is inversely proportional to the phase inductance, rotor position sector can be detected by comparing the current amplitude of three phases, which can be obtained from current sensors and the two thresholds.

As we can see from the Fig. 3.1, pulses are injected to the phase A to detect the rotor position and phase B is used for conduction. Since the value of inductance of phase A is high, the corresponding current amplitude is small. The inductance of phase C is minimum and the corresponding current is maximum. And the phase inductance of phase B is between the maximum value and minimum value. Therefore, if the current amplitude of phase A is below the low threshold and the current amplitude of phase C is above the high threshold and the current amplitude of phase B is between the two thresholds, it means that the initial rotor position is located at sector 1. In this way, the corresponding sensing and motoring phase can be found. Similarly, if the current amplitude of phase A is between the two thresholds and the current amplitude of phase B is below the low threshold and the current amplitude of phase C is above the high threshold, it means that the phase inductance of phase A is between the maximum and minimum value, phase B is the maximum value, and phase C is the minimum value. In this situation, the rotor position is located at sector 2. In the similar analysis, the sector division scheme by

inductance profiles and initial current pulse amplitude are shown in TABLE 3.1. With this scheme, the initial position can be detected. Besides, when detecting the initial position, the speed of SRM should be zero.

TABLE 3.1 Sector Initialization in Relation to the Current Pulse Amplitude

Sector	Phase A	Phase B	Phase C
1	$I_A <$ Low Threshold	Low Threshold $< I_B <$ High Threshold	$I_C >$ High Threshold
2	Low Threshold $< I_A <$ High Threshold	$I_B <$ Low Threshold	$I_C >$ High Threshold
3	$I_A >$ High Threshold	$I_B <$ Low Threshold	Low Threshold $< I_C <$ High Threshold
4	$I_A >$ High Threshold	Low Threshold $< I_B <$ High Threshold	$I_C <$ Low Threshold
5	Low Threshold $< I_A <$ High Threshold	$I_B >$ High Threshold	$I_C <$ Low Threshold
6	$I_A <$ Low Threshold	$I_B >$ High Threshold	Low Threshold $< I_C <$ High Threshold

B. One current threshold method

One current threshold method is proposed in [52]. This method utilizes the time required for current to reach the threshold and phase inductance profile to determine the initial rotor position region.

As is known, the inductance profile of the stator phases in an SRM is periodic functions of the rotor position, and inductance profile exhibits its maximum and minimum at the aligned position and unaligned position respectively. Besides, the nonlinear region exists in the vicinity of the aligned and unaligned position. As shown in Fig. 3.2, the inductance profile of three-phase 6/4 machine in one electrical period can be divided into six regions by comparing the magnitude of inductances. The position information needs to be extracted in a target region. Each phase of stator needs to be excited with a voltage pulse. When the phase is excited with voltage pulse, the value of current is increased. And once the current reaches a threshold, the voltage needs to be reversed to remove the current and the time required reaching the threshold are recorded. And the comparison method and region division are shown in TABLE 3.2.
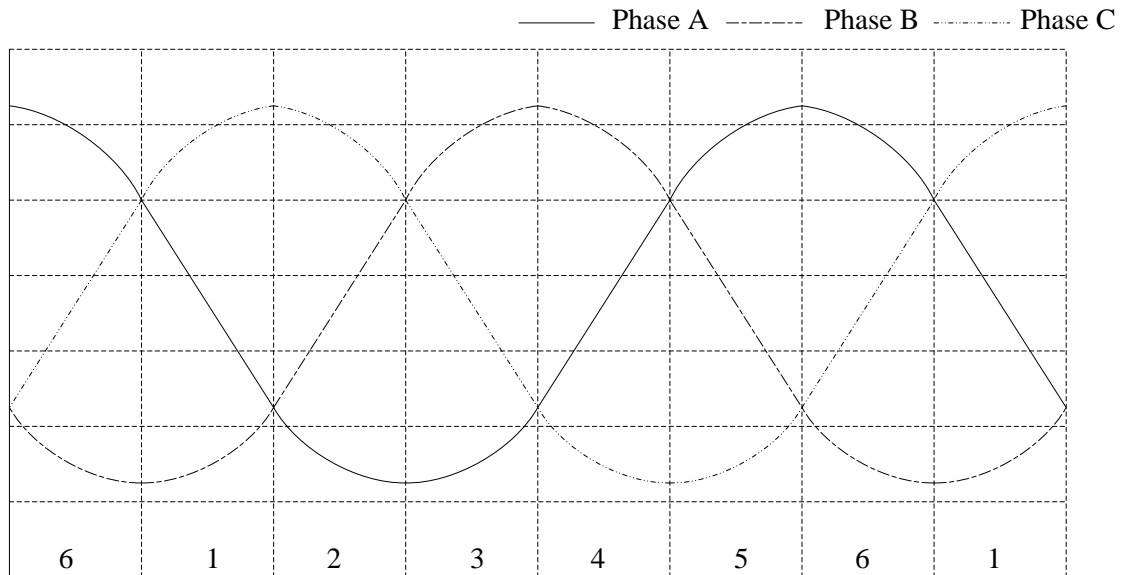

Fig. 3.2 Inductance profile of an 6/4 SRM along with the linear region

46

TABLE 3.2 Summary of rotor position region vs. inductance relationship

Order of time magnitude	Order of inductances	Rotor position (electrical degree)	Region	Phase linear region chosen
$\delta_1 > \delta_3 > \delta_2$	$L_A > L_C > L_B$	0° to 60°	6	C
$\delta_3 > \delta_1 > \delta_2$	$L_C > L_A > L_B$	60° to 120°	1	A
$\delta_3 > \delta_2 > \delta_1$	$L_C > L_B > L_A$	120° to 180°	2	B
$\delta_2 > \delta_3 > \delta_1$	$L_B > L_C > L_A$	180° to 240°	3	C
$\delta_2 > \delta_1 > \delta_3$	$L_B > L_A > L_C$	240° to 300°	4	A
$\delta_1 > \delta_2 > \delta_3$	$L_A > L_B > L_C$	300° to 360°	5	B

3.2.2. APPLIED INITIAL POSITION ESTIMATION METHOD

The disadvantage of current threshold method is that it requires much effort to judiciously select the value of threshold. However, the basic idea of current threshold method can still be used. Instead of comparing the phase current with the current threshold, the phase inductance magnitude of three-phases can be directly compared to locate the initial rotor position in specific region.

As shown in Fig. 3.1, the inductance profiles have been divided into six regions. In each region, the magnitudes of inductances can be calculated by (3.2) when injecting the same pulses into three phases simultaneously. By comparing the magnitude of the inductance three phases, the region with a length of 60° can be uniquely detected within which the

rotor position is located. And then the corresponding sensing phase and active phase can be chosen.

TABLE 3.3 shows the relationship of inductance comparison and sensing phases. The inductance of each phase is calculated by injecting current pulses to three phases simultaneously.

TABLE 3.3 Initial position detection by comparing phase inductance.

Inductances comparison	Rotor position (electrical degree)	Sensing phase
$L_A > L_B >= L_C$	$0° =< \theta_{initial} < 60°$	A
$L_B > L_A >= L_C$	$60° = < \theta_{initial} < 120°$	A
$L_B > L_C >= L_A$	$120° =< \theta_{initial} < 180°°$	B
$L_C > L_B > =L_A$	$180° =< \theta_{initial} < 240°$	B
$L_C > L_A >= L_B$	$240° =< \theta_{initial} < 300°$	C
$L_A > L_C > =L_B$	$300° =< \theta_{initial} < 360°$	C

Compared with current threshold method, the advantage of this method is that there is no need to select the value of threshold. Besides, there is no need to know the exact initial rotor position, either. With the information of initial position region, the sensing phase is selected. Then, position estimation technique is applied to estimate the rotor position.
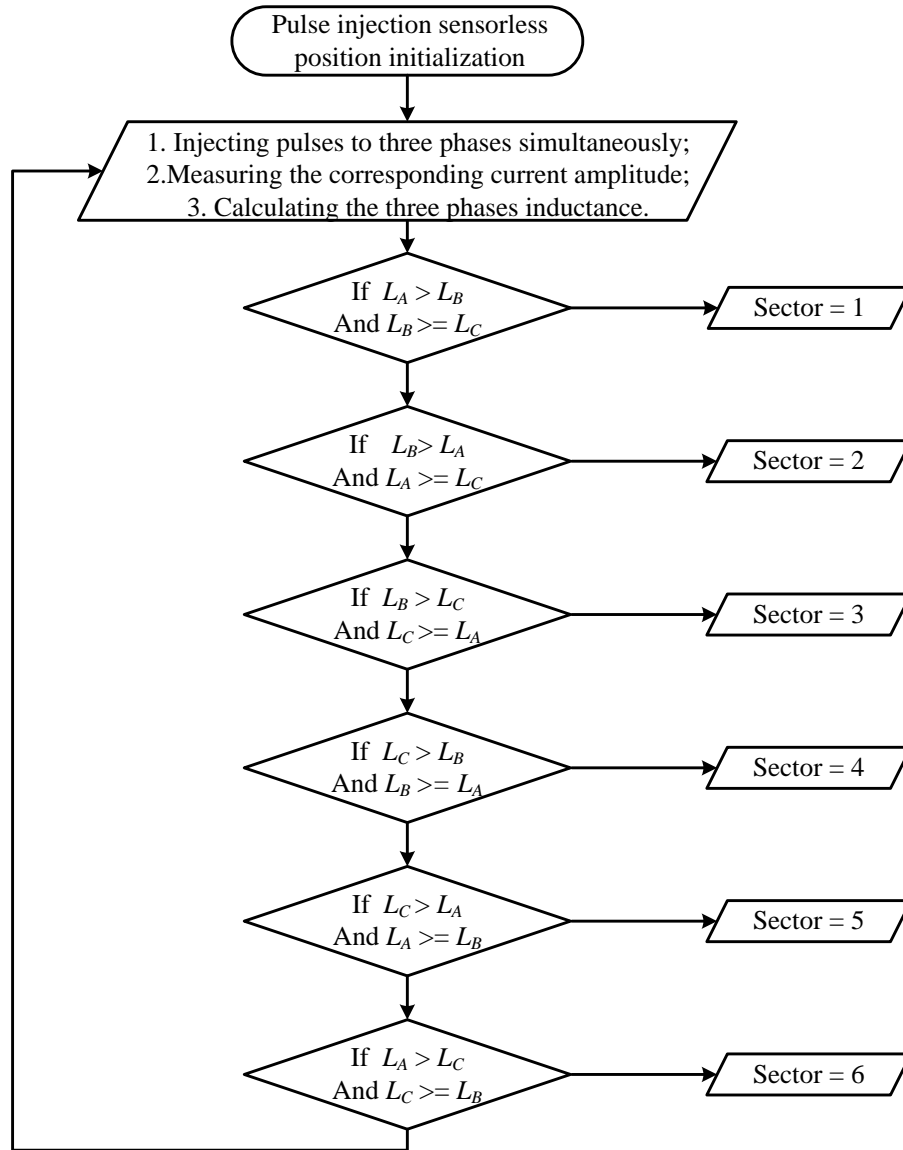
Fig. 3.3 Pulse injection initial position sensorless technique flowchart.

The flowchart of this initial position detecting method is shown in Fig. 3.3. This flowchart gives the idea of how to apply this sensorless method to the software. Fig. 3.3

describes the logic of the application to position initialization, and it is suitable for any repetition of three-phase machines. Furthermore, for machines with a high number of phases, such as 8/6 four-phase machine, the sector arrangement has to be changed to match the phase detection requirement. However, the sector arrangement will still be similar to the three-phase implementation.

3.3. SENSORLESS TECHNIQUE AT LOW SPEED OPERATION

3.3.1. ROTOR POSITION ESTIMATION TECHNIQUE

Assuming that the phase inductance is unsaturated, Fig. 3.4 shows the linearized relationship of phase inductance and rotor position. For each phase, the phase inductance decreasing region is between 0° and 120° (electrical degree), and the high-frequency pulses should be injected to this region to sense the rotor position.

Fig. 3.4 Phase Inductance vs. rotor position.

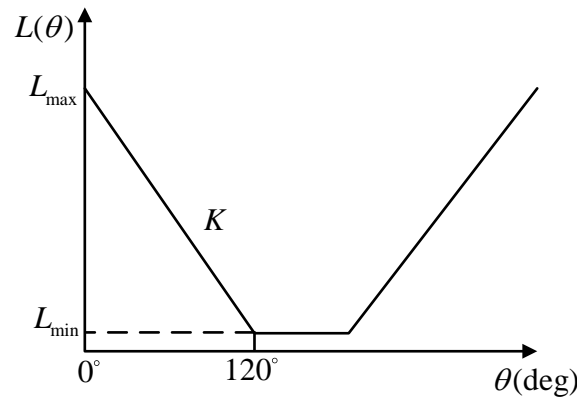As presented in Fig. 3.1, with the data of phase inductance obtained from experiment and phase current detected by current sensors, the slope of phase inductance decreasing region K is calculated. Since instant phase inductance is calculated from (3.2), the instantaneous rotor position for phase A is calculated by the following equation.

$$\theta_{rA} = \frac{L_{max} - L(\theta)}{K} + \theta_1 \qquad (3.3)$$

Where K is defined in (1.11), and $K = (L_{max} - L_{min})/120°$ in this case. θ_1 is an initial position for sensing phase.

Therefore, since phase A is sensed between 0° and 120°, the initial position for sensing is 0°, and then θ_1 is equal to 0°. Similarly, phase B is sensed between 120° and 240°, and θ_1 is equal to 120°; phase C is sensed between 240° and 360°, and θ_1 is equal to 240°. Then the rotor position for phase A is estimated by sequentially injecting the high-frequency pulses to idle phases. Once the rotor position for phase A is determined precisely, the rotor position for phase B and C can be calculated by the following expressions.

$$\begin{cases} \theta_{rB} = \theta_{rA} + 240° \\ \theta_{rC} = \theta_{rA} + 120° \end{cases} \qquad (3.4)$$

Fig. 3.5 describes the control scheme for one electrical cycle. The current for active phase and idle (sensing) phase are given, and corresponding estimated positions are depicted. It

is evident to see how the algorithm (3.3) and (3.4) work to determine rotor position for three phases SRM.
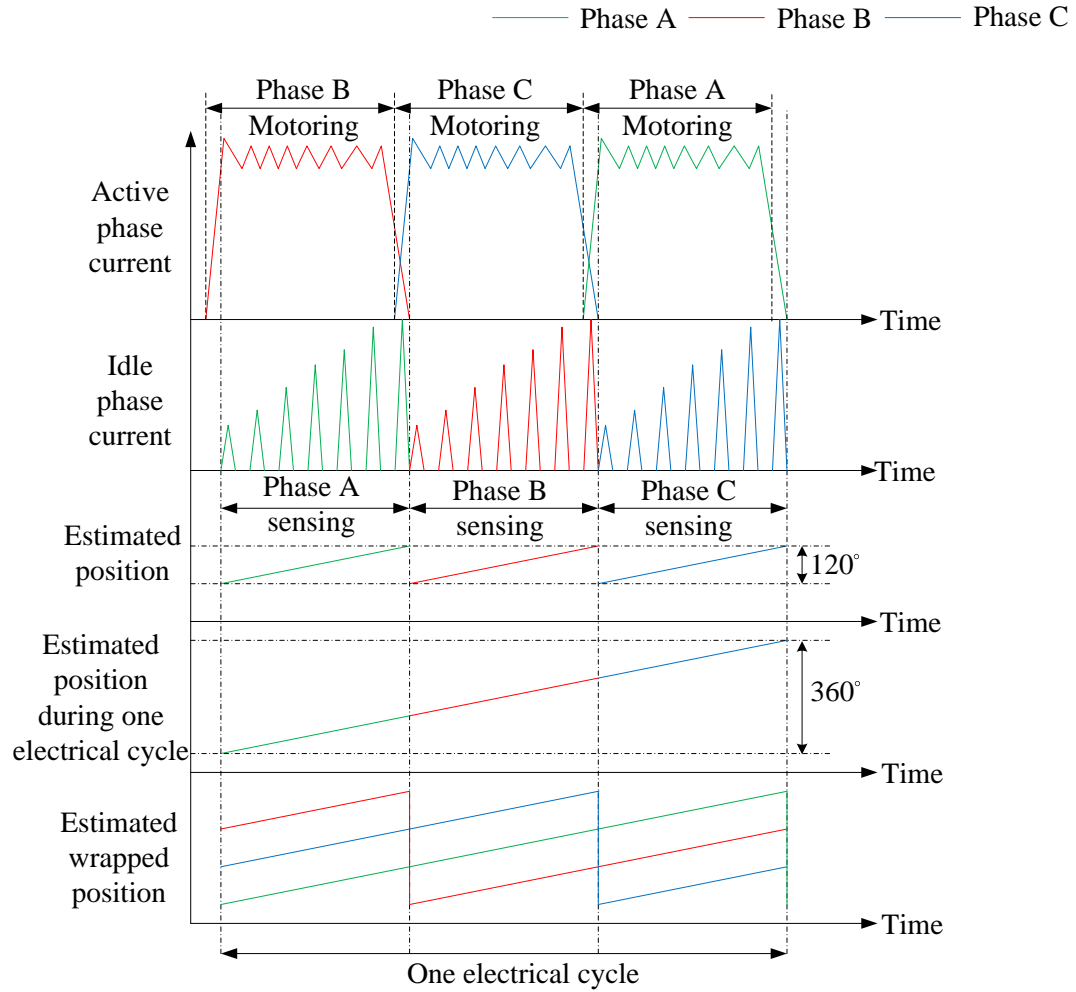

Fig. 3.5 Active and sensing currents, and estimated position during one electrical cycle

for 3 phases SRM.

In conclusion, the mathematic model of pulse-injection method can be listed in the following expressions.

52

$$\theta_{rA} = \begin{cases} \dfrac{L_{\max} - L_a(\theta)}{K}, L_a(\theta) = U_a \dfrac{T_s}{\Delta i_a} & 0 \le \theta < 120 \\[3mm] \dfrac{L_{\max} - L_b(\theta)}{K} + 120, L_b(\theta) = U_b \dfrac{T_s}{\Delta i_b} & 120 \le \theta < 240 \\[3mm] \dfrac{L_{\max} - L_c(\theta)}{K} + 240, L_c(\theta) = U_c \dfrac{T_s}{\Delta i_c} & 240 \le \theta < 360 \end{cases} \qquad (3.5)$$

Where U_a, U_b, U_c are phase voltages; Δi_a, Δi_b, Δi_c are current variations; T_s is the sample time. By combining (3.5) and (3.4) together, the rotor position of three phases at low speed can be precisely detected.

3.3.2. PROPOSED PULSE INJECTION METHOD FOR SRM

The pulse injection method to estimated rotor position is introduced in the previous section. However, the drawback is that the saturation of phase inductance hasn't been considered. So considering the saturation region of phase inductance, a new algorithm is proposed as follows.

As shown in Fig. 3.6 (a), the profile of phase inductance varies with rotor position under different currents is presented. From this figure, it is obvious that the phase inductance has saturation region no matter what the value of phase current is. In this case, the value of slope K in (3.3) cannot be used to precisely calculate the rotor position. To solve the saturation problem of phase inductance, the phase inductance decreasing region can be

divided into two parts, and the slopes of these two parts are K_1 and K_2, as shown in Fig. 3.6 (b). Assuming that the saturation region is before θ_s, (3.5) can be improved as

$$
\theta_{rA} = \begin{cases}
\left.\begin{array}{l} \dfrac{L_{\max}(i) - L_a(\theta)}{K_1} \\[2ex] \dfrac{L_{as}(i) - L_a(\theta)}{K_2} + \theta_s \end{array}\right\} L_a(\theta) = U_a \dfrac{T_s}{\Delta i_a} & \begin{array}{l} 0 \le \theta < \theta_s \\[1ex] \theta_s \le \theta < 120 \end{array} \\[6ex]
\left.\begin{array}{l} \dfrac{L_{\max}(i) - L_b(\theta)}{K_1} + 120 \\[2ex] \dfrac{L_{bs}(i) - L_b(\theta)}{K_2} + \theta_s + 120 \end{array}\right\} L_b(\theta) = U_b \dfrac{T_s}{\Delta i_b} & \begin{array}{l} 120 \le \theta < \theta_s + 120 \\[1ex] \theta_s + 120 \le \theta < 240 \end{array} \\[6ex]
\left.\begin{array}{l} \dfrac{L_{\max}(i) - L_c(\theta)}{K_1} + 240 \\[2ex] \dfrac{L_{cs}(i) - L_c(\theta)}{K_2} + \theta_s + 240 \end{array}\right\} L_c(\theta) = U_c \dfrac{T_s}{\Delta i_c} & \begin{array}{l} 240 \le \theta < \theta_s + 240 \\[1ex] \theta_s + 240 \le \theta < 360 \end{array}
\end{cases}
\tag{3.6}
$$

Where L_{as}, L_{bs}, and L_{cs} are phase inductance at position θ_s. $L_{\max}(i)$, $L_{as}(i)$, $L_{bs}(i)$, and $L_{cs}(i)$ vary with the phase current. K_1 and K_2 can be defined as

$$
\begin{cases}
K_1 = \dfrac{L_{\max}(i) - L_s(i)}{\theta_s} \\[3ex]
K_2 = \dfrac{L_s(i) - L_{\min}}{120 - \theta_s}
\end{cases}
\tag{3.7}
$$

For different phase current values, the inductance waveforms are different. So in order to precisely detect the rotor position, it is important to locate the corresponding inductance waveform according to simultaneous phase current. As shown in Fig. 3.6 (c), several phase inductance profiles of various current values are depicted. Assuming that θ_s is

selected as shown in the figure, it is obvious that the phase inductance at θ_s ranges from $L_{s\,min}$ to $L_{s\,max}$. Besides, the L_{max} also ranges from $8 \times 10^{-3}\,\mathrm{H}$ and $11 \times 10^{-3}\,\mathrm{H}$. To obtain the correct value of K_1 and K_2, the look-up tables with phase current and corresponding phase inductance at $0°$ and θ_s have to be respectively constructed. By measuring the instantaneous phase current, $L_{max}(i)$, $L_{as}(i)$, $L_{bs}(i)$, and $L_{cs}(i)$ can be obtained by searching the look-up table. From the Fig. 3.6 (c), it can be seen that the phase inductance for all current values are the same at $120°$. So there is no need to construct the look-up table for L_{min}. Then the slope K_1 and K_2 can be correctly calculated, and the rotor position can also be precisely estimated.

Moreover, it is clearly that the phase inductance is flat at aligned position when the phase current is high, which makes it more difficult to correctly calculate K_1. So the injected current should be small. In this way, the operation of the system would not be affected, and the rotor position can be calculated with high accuracy.
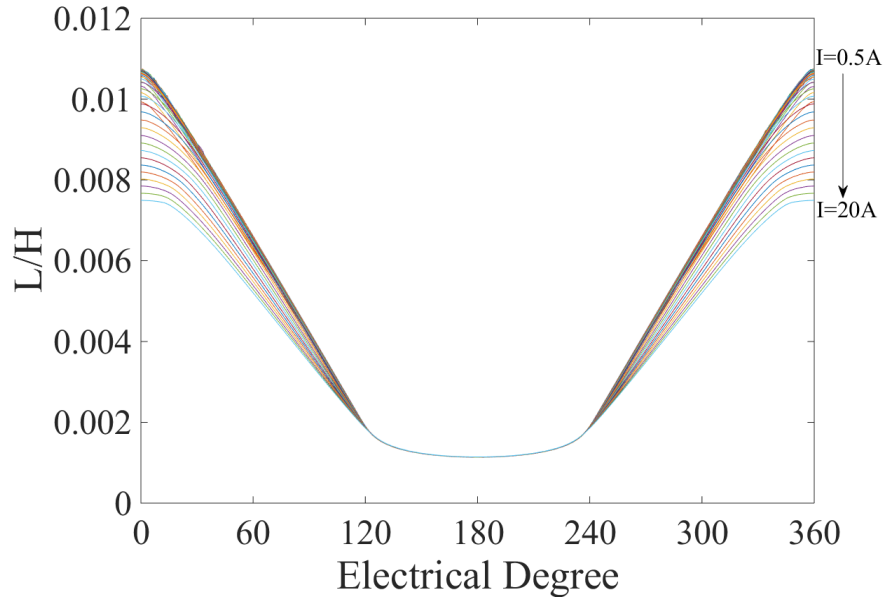
(a) Phase inductance vs. rotor position under different currents.
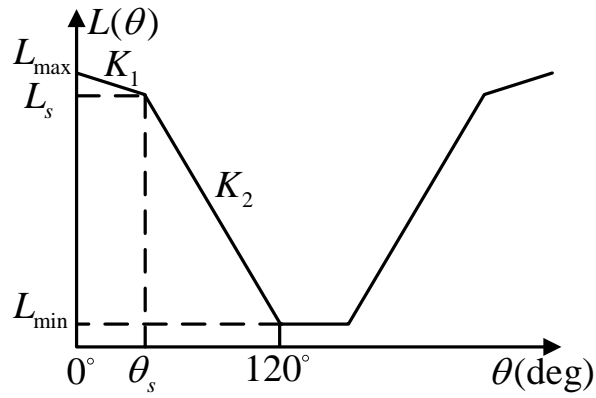
(b) The division of phase inductance region.
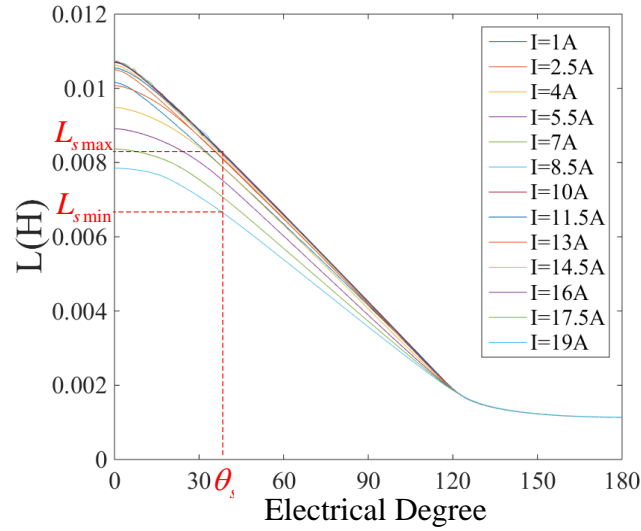
(c) Application of division of phase inductance.

Fig. 3.6 The profile of phase inductance.

3.3.3. ROTOR SPEED ESTIMATION TECHNIQUE

Then, it is possible to estimate the rotor speed every rotor step (120° electrical degree or 30° mechanical degree for 12/8 SRM). During every 30° movement, the rotor positions at two specific points are sampled. And then, it is important to measure the time difference between these two points. The rotor position can be calculated by the following equation.

$$\omega = \Delta\theta \, / \, \Delta t \tag{3.8}$$

The flowchart of algorithm to estimate the rotor speed is shown in Fig.3.7. This speed estimation method may lose accuracy during high-speed operation. However, the advantage is that the noise can be overcome and the impact of time delay is insignificant.

```
┌─────────────────────────────┐
│  Input: rotor position signal │
└─────────────────────────────┘
              │
              ▼
┌─────────────────────────────┐
│  Measure the rotor position at specific │
│  position for every 30 degree movement │
└─────────────────────────────┘
              │
              ▼
┌─────────────────────────────┐
│  Record and calculate the time difference at │
│  these two rotor positions │
└─────────────────────────────┘
              │
              ▼
┌─────────────────────────────┐
│       ω = Δθ / Δt           │
└─────────────────────────────┘
              │
              ▼
┌─────────────────────────────┐
│  Use the present speed value until the new │
│  speed calculation │
└─────────────────────────────┘
              │
              ▼
┌─────────────────────────────┐
│            End              │
└─────────────────────────────┘
```
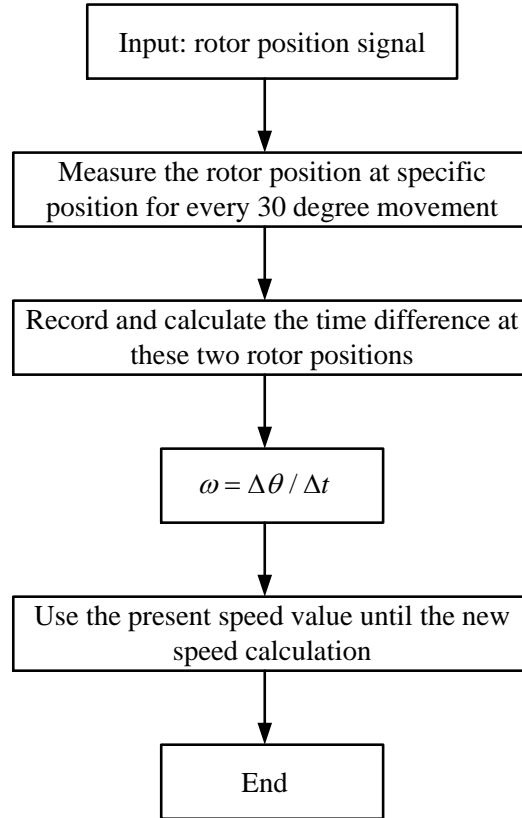
Fig. 3.7 Flowchart of speed estimation.

However, another problem of this speed estimation method is that estimated speed cannot track the actual speed precisely during acceleration period. To solve this problem, three-

order phase locked loop (PLL) is used to calculate the rotor speed. A third-order PLL is designed as follows.

$$\theta_{PLL} = \omega_{PLL}t + K_{\theta_P}e \tag{3.9}$$

$$\omega_{PLL} = a_{PLL}t + K_{\omega_p}e \tag{3.10}$$

$$a_{PLL} = K_{\alpha_p}e \tag{3.11}$$

Where K_{θ_P}, K_{ω_p}, and K_{α_p} are the PLL gains. And e is the error between the estimated rotor position and the output rotor position of PLL. The definition of e is presented as follow.

$$e = \theta_e - \theta_{PLL} \tag{3.12}$$

To minimize the error e, the accuracy of estimated rotor position can be greatly improved. And the estimated rotor speed can track the actual speed during acceleration period.

Chapter 4

SLIDING-MODE-OBSERVER BASED SENSORLESS CONTROL METHOD

4.1. INTRODUCTION

The observer-based method, which is another effective way to detect rotor position, makes use of state-space equations to derive an observer with the measurements of phase voltage and current. Generally, the variables of an observer are flux-linkage, rotor position, and rotor speed.

Sliding mode controllers have excellent robustness and performance for specific nonlinear systems tracking problems [53]. The basic idea of sliding mode control algorithm is to drive the state variables sliding on the given sliding surface [54]. Based on sliding-mode controllers, the sliding-mode observers were proposed to estimate the rotor position and speed of switched reluctance motor.

4.1.1. SLIDING-MODE CONTROL

The sliding-mode control (SMC) can also be defined as variable structure control (VSCS). Sliding mode theory is developing fast recently. The applications of SMC receive

practical success in many control systems, such as SISO system, MIMO system, and nonlinear system [55] [56] [57]. As for the design of SMC, there are two points need to be considered. The first point is the design of a stable sliding mode surface, and the other point is the design of control law to force the system states reaching the designed surface with finite time [58] [59]. The design of sliding mode surface has to meet all the requirements optimally with considering all the constraints and specifications.

4.1.2. SLIDING MODE SURFACE

The control problem is to get the state x of the plant track a specific desired time varying state x_d in the presence of model impression and parameter variation [54]. Both

$x = \begin{bmatrix} x & \dot{x} & \ddot{x} & ... & x^{(n-1)} \end{bmatrix}^T$ and $x_d = \begin{bmatrix} x_d & \dot{x}_d & \ddot{x}_d & ... & x_d^{(n-1)} \end{bmatrix}^T$ are vectors.

The tracking error vector $\tilde{x}$ can be defined as

$$\tilde{x} = x - x_d = \begin{bmatrix} \tilde{x} & \dot{\tilde{x}} & \ddot{\tilde{x}} & ... & \tilde{x}^{(n-1)} \end{bmatrix}^T \tag{4.1}$$

And then the time-varying surface $S(t)$ in the state-space $\mathbb{R}^{(n)}$ can be defined by the scalar equation $s(\tilde{x};t) = 0$ with

$$s(\tilde{x};t) = \left(\frac{d}{dt} + \lambda \right)^{n-1} \tilde{x} \tag{4.2}$$
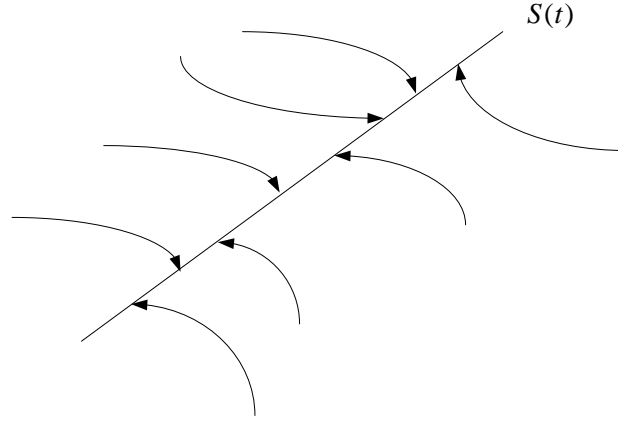
Where λ is a constant.

Fig. 4.1 The sliding condition.

For the tracking problem $x \equiv x_d$, it mains that the state remains on the sliding surface $S(t)$ for all $t > 0$, indicating that $\tilde{x} \equiv 0$ and $s(\tilde{x};t) \equiv 0$. However, when $s(\tilde{x};t) > 0$, the control law need to manipulate the state x to drive the system back to the sliding surface, and the oppose occurs when $s(\tilde{x};t) < 0$. Given these conditions, the control law outside of $S(t)$ can be chosen as [54]

$$\frac{1}{2}\frac{d}{dt}s^2(\tilde{x};t) \leq -\eta|s| \tag{4.3}$$

Where η is a strictly positive constant. According to the control law (4.3), the sliding condition can be described in Fig. 4.1. The control law constrains all the trajectories to point towards the surface.

4.1.3. CHATTERING PHENOMENON

The perfect sliding mode is hard to realize in practice because of the fast commute frequency. Since there are also some switching imperfections, such as switching time delays, the discontinuity in the feedback control will produce chattering, which is a particular dynamic behavior in the vicinity of the sliding surface [60], as shown in Fig. 4.2.
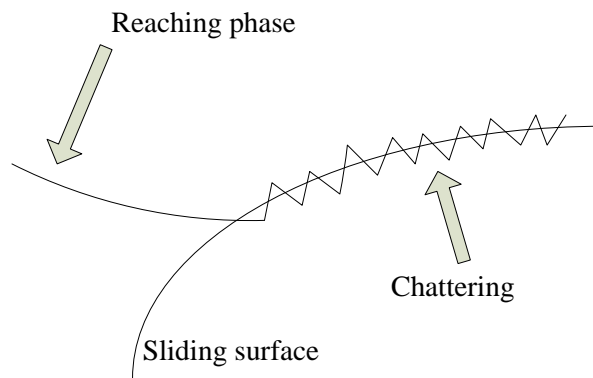

Fig. 4.2 Chattering phenomenon.

Chattering is undesirable in the sliding mode control since it may excite un-modeled high-frequency dynamics [61]. The consequence is that the performance of the system may be degraded and even be unstable. Chattering may also lead to high wear of moving mechanical structure and high heat losses in electrical power system [60]. Many solutions were proposed to eliminate the chattering phenomenon, and one of them is replacing the signum function in the control scheme by saturation function with appropriate boundary layer, as shown in Fig. 4.3. This improvement will help smooth out the control

discontinuity. As for how to use this replacement, it will be mentioned in the following sections.
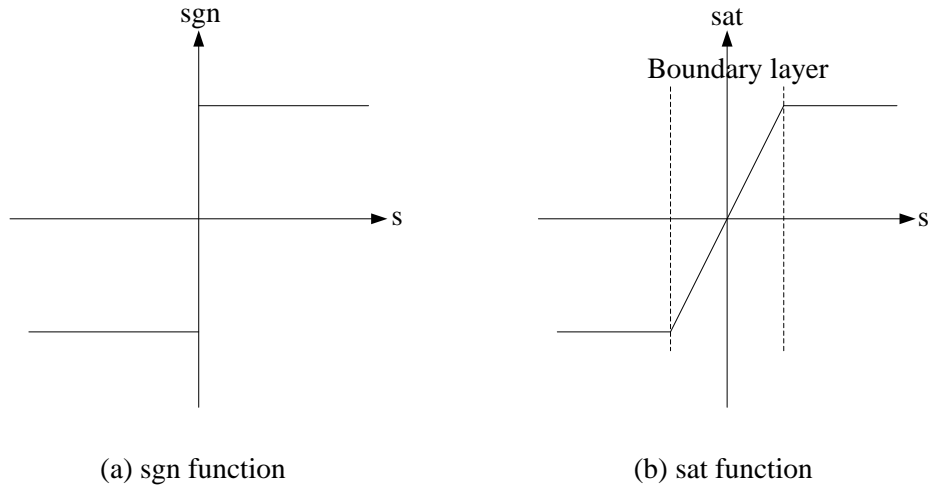

(a) sgn function   (b) sat function

Fig. 4.3 sgn function vs. sat function.

4.1.4. BASIC CONTROL ISSUES

Considering linear system firstly, the linear system with multi-input is defined as follow [60].

$$\dot{x} = Ax + Bu \qquad (4.4)$$

Where $x \in \mathbb{R}^n$, $u \in \mathbb{R}^n$ and rank $B = m$. Then the sliding surface can be defined as

$$S = \left\{ x \in \mathbb{R}^n : s(x) = Cx = 0 \right\} \qquad (4.5)$$

Where C is a full rank matrix. Assuming that CB is invertible, the equivalent control which will affect the sliding motion is defined as

$$u_e = -(CB)^{-1}CAx \tag{4.6}$$

Consequently, the equivalent dynamics is defined by

$$\dot{x}_e = \left[I - B(CB)^{-1}C \right] Ax_e = A_e x_e \tag{4.7}$$

The model and m switching surface for the nonlinear systems is defined as follows,

$$\dot{x} = f(x) + g(x)u(t) \tag{4.8}$$

$$S = \left\{ x \in \mathbb{R}^n : s(x) = \left[s_1(x), ..., s_m(x) \right]^T = 0 \right\} \tag{4.9}$$

And associated equivalent control and resulting dynamics are as follows.

$$u_e = -\left[\frac{\partial s}{\partial x} g(x) \right]^{-1} \frac{\partial s}{\partial x} f(x) \tag{4.10}$$

$$x_e = \left[I - g(x_e) \left[\frac{\partial s}{\partial x_e} g(x_e) \right]^{-1} \frac{\partial s}{\partial x_e} \right] f(x_e) \tag{4.11}$$

Either linear system or nonlinear system, the control function can be expressed as follows.

$$u(x,t) = \begin{cases} u^+(x,t) & s(x) > 0 \\ u^-(x,t) & s(x) < 0 \end{cases} \tag{4.12}$$

65

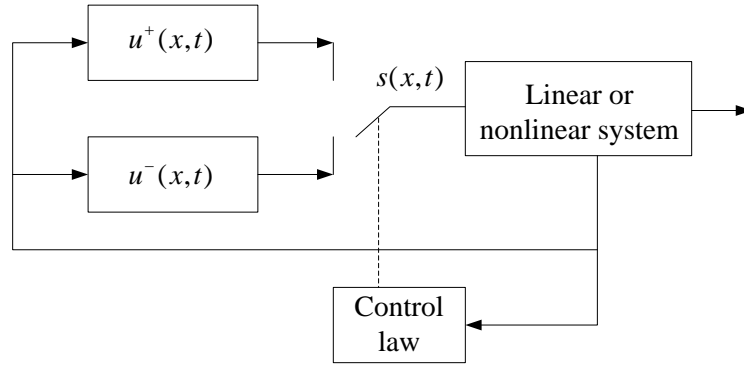Where $u^+(x,t) \neq u^-(x,t)$. The diagram is shown in Fig. 4.4.

Fig. 4.4 Sliding Mode control law.

To realize the sliding mode control, several basic issues have to be ensured, including existence, reachability and stability. To ensure the existence of sliding mode control, the sign of $s(x)$ and $\dot{s}(x)$ should be opposite.

$$\lim_{s \to 0_+} \dot{s} < 0 \qquad (4.13)$$

$$\lim_{s \to 0_-} \dot{s} > 0 \qquad (4.14)$$

At an arbitrary initial condition, to ensure the state reaching the sliding surface within finite time, the following condition has to be satisfied.

$$s\dot{s} < 0 \qquad (4.15)$$

The above condition is also called reachability condition. And this condition is one of the design considerations when to apply the sliding mode control to the system. Besides, as for the control system, the sliding motion has to be asymmetry stable, and the sliding surface has to pass the balance point.

Alternatively, a control law can be obtained by a reaching law. There are three reaching law which can be considered to be used to get control law[58].

a. The constant rate reaching law:

$$\dot{s} = -Q \operatorname{sgn}(s) \qquad (4.16)$$

b. The constant plus proportional rate reaching law:

$$\dot{s} = -Ks - Q \operatorname{sgn}(s) \qquad (4.17)$$

c. The power rate reaching law:

$$\dot{s}_i = -\bar{Q} |s_i|^{a_i} \operatorname{sgn}(s_i), i = 1, 2, 3...m \qquad (4.18)$$

Where Q and K are diagonal matrices with positive elements, $\bar{Q}$ is a positive scalar and $a_i \in (0,1)$.

4.2. SLIDING-MODE OBSERVER

Based on the technique of sliding-mode control, the sliding-mode observer was developed to control nonlinear systems due to its computational simplicity and robust properties. Fox example, the technology of sliding mode observer can be used to detect the SRM position. There are several advantages of developing the sliding-mode observer for sensorless control [60]. Firstly, it has excellent robustness under parameter variation and model uncertainty, and the observation error dynamics can be significantly reduced. Secondly, all the observer states could converge to the steady-state with finite time. Thirdly, as for design, the observer can be designed for the non-smooth system.

Several sensorless control for SRM based on sliding mode observer is introduced in Chapter 2. Based on the fundamental principle of these methods, a new sensorless control method to detect rotor position using sliding-mode observer is proposed. An estimation of speed acceleration is introduced to reduce the dynamic error. Combining with the nonlinear model (1.14), the movement equations for the new sensorless method can be expressed as follows by modifying (1.15) and (1.16).

$$\frac{d\theta(t)}{dt} = \omega(t) \tag{4.19}$$

$$\frac{d\omega(t)}{dt} = \alpha(t) \tag{4.20}$$

where θ and ω are the rotor position and angular speed, respectively. α is the angular speed acceleration. The flux-current-position characteristic of SRM is shown in Fig. 4.5.
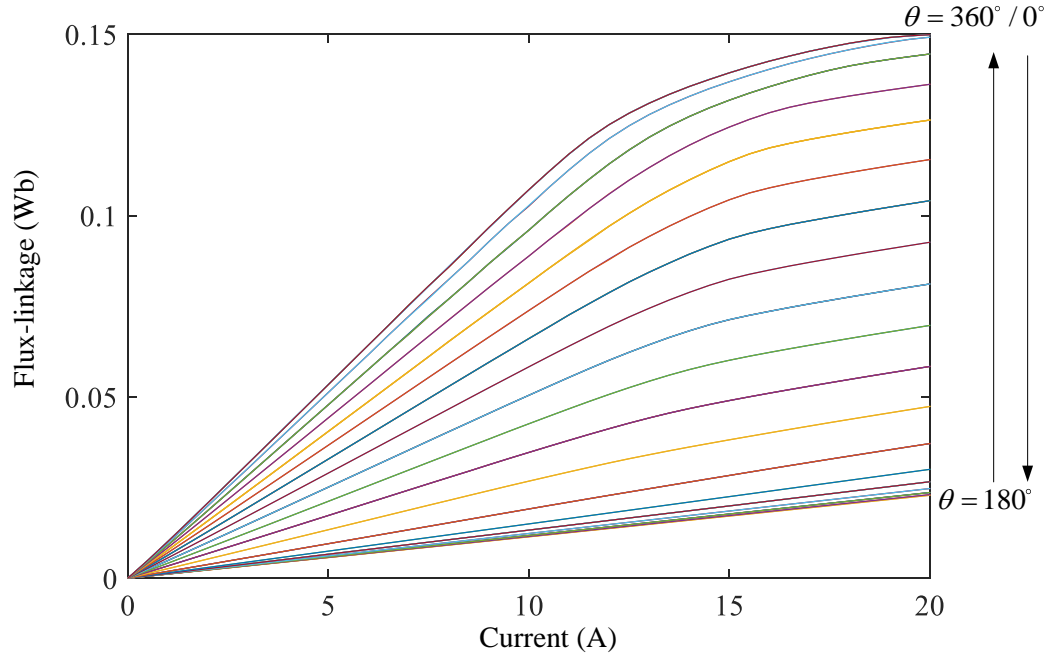
68

Fig. 4.5 Flux-current-position characteristic of SRM.

By neglecting the variation of the value of phase resistance, the measured flux-linkage can be obtained by integrating the voltage drop on the phase winding. The predetermined tabular form, which includes the characteristics of phase flux-linkage, phase current, and rotor position, is required to get the estimated flux linkage.

$$\lambda_n(t) = \int_0^t (v_n(\xi) - i_n(\xi) r_n) d\xi \tag{4.21}$$

$$\hat{\lambda}_n(t) = \hat{\lambda}_n(i_n(t), \hat{\theta}(t)) \tag{4.22}$$

Where λ_n and $\hat{\lambda}_n$ are measured flux-linkage and estimated flux-linkage, respectively.

69

4.2.1. PROPOSED SMO POSITION DETECTION FOR SRM

In order to build a sliding-mode observer, an appropriate sliding-mode surface should be designed first as shown in the following equation [62].

$$s = 0 \tag{4.23}$$

The difference between measured flux-linkage and estimated flux-linkage is selected as the error correction term. The flux-linkage estimation error of each phase e_n is defined as,

$$e_n = \lambda_n(t) - \hat{\lambda}_n(t), n = 1, 2, \ldots, m \tag{4.24}$$

As shown in Fig. 4.5, for a particular current, when the rotor position moves from unaligned position 0° to aligned position 180°, the flux-linkage is monotonically increasing with θ, and when the rotor position moves from aligned position 180° to unaligned position 360°, the flux-linkage is monotonically decreasing with θ. The sliding-mode surface, which will vary with the rotor position, is related to the total estimation error. In this case, the sliding-mode surface should be adjusted as

$$s = \frac{1}{n} \sum_{\xi=1}^{n} p \cdot e_\xi(t) \tag{4.25}$$

where p is a factor that keeps s being monotonically increasing with θ for certain current. p is defined as

$$p = \begin{cases} 1, \hat{\theta} \in (180,360] \\ -1, \hat{\theta} \in (0,180] \end{cases} \tag{4.26}$$

From (4.25) and (4.26), it is clear that sliding-mode surface is defined as total error function of active phases. And for each active phases, the estimation error is multiplied by 1 when rotor position belonged to (0,180], and is multiplied by -1 when rotor position belongs to (180,360]. Then equation (4.23) needs to be satisfied to design the sliding-mode observer.

As introduced in section 1.3.1, during the region 2 (phase inductance increasing region), when measured flux-linkage is larger than estimated flux-linkage ($e_\lambda > 0$), it indicate that estimated rotor position is lag behind actual position, so positive correction item need to be added up to observer to increase the estimated value, and vice versa. During the region 4 (phase inductance decreasing region), when measured flux-linkage is larger than estimated flux-linkage ($e_\lambda > 0$), it indicate that estimated rotor position is leading the actual position, so negative correction item need to be added to observer to decrease the estimated value, and vice versa. It demonstrates that the design of sliding-mode surface can be appropriately applied to the proposed model. Then the observer can be designed as follows by using the constant reaching law (4.16).

$$\dot{\hat{\theta}}(t) = \hat{\omega}(t) + k_\theta \operatorname{sgn}(s) \tag{4.27}$$

$$\dot{\hat{\omega}}(t) = \hat{\alpha}(t) + k_\omega \operatorname{sgn}(s) \tag{4.28}$$

$$\dot{\hat{\alpha}}(t) = k_\alpha \, \text{sgn}(s) \qquad (4.29)$$

Where $\hat{\theta}$ and $\hat{\omega}$ are the estimated rotor position and speed, respectively. k_ω, k_θ, and k_α are SMO gains and have to be chosen appropriately for accurate estimation. The block diagram of the SMO is shown in Fig.4.6.
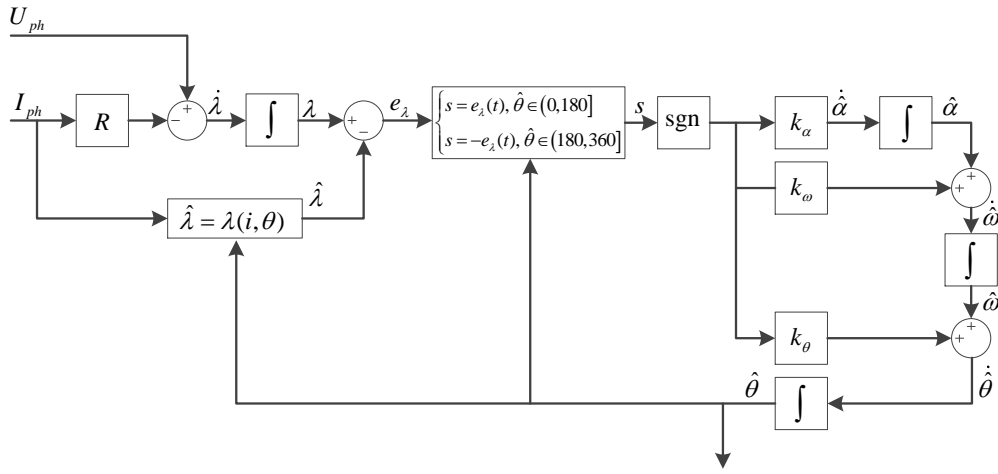

Fig. 4.6 Block diagram of the sliding-mode observer.

Since the chattering is unavoidable when SMO is applied, as introduced in section 4.1.3, the saturation function is used to replace the signum function in the observer to decrease the chattering. Assuming the boundary layer of the linear region is μ, a modified observer can be expressed by modifying (4.27) -(4.29) as

$$\dot{\hat{\theta}}(t) = \hat{\omega}(t) + k_\theta \text{sat}(s) \qquad (4.30)$$

$$\dot{\hat{\omega}}(t) = \hat{\alpha}(t) + k_\omega \text{sat}(s) \qquad (4.31)$$

$$\dot{\alpha}(t) = k_{\alpha}\mathrm{sat}(s) \tag{4.32}$$

Where "sat" function is defined as

$$\mathrm{sat}(s) = \begin{cases} \mathrm{sgn}(s), & |s| > \mu \\ s/\mu, & |s| \le \mu \end{cases} \tag{4.33}$$

Since the flux-linkage estimation error is small in the linear region, the value of correction item is greatly reduced. Thus, the amplitude of chattering can be minimized. However, when the states don't enter the linear region, the correct items are large enough to ensure the convergence speed. Hence, not only the stability and robustness of observer is greatly improved, but also the convergence speed is maintained. Besides, by adjusting the boundary layer, the accuracy and robustness of SMO method is enhanced.

4.2.2. DESIGN GAINS FOR SMO

Given that the SRM system is a nonlinear system, the stability of system under the selection of observer gains can be analyzed by describing function. The basic block structure of describing function is shown in Fig. 4.7.
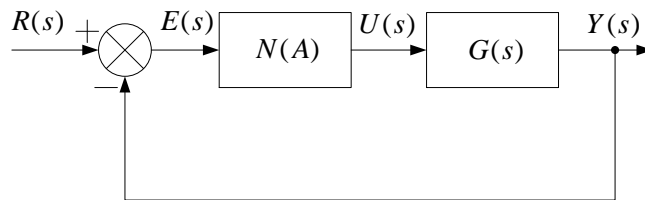
Fig. 4.7 Nonlinear block structure of describing function.

The characteristics of the nonlinear part can be expressed by describing function $N(A)$. And the transfer function $G(s)$ represents the linear parts of the system. $R(s)$, $Y(s)$, $E(s)$, and $U(s)$ respectively denote the input, output, error, and the output of nonlinear parts.

The nonlinearity of sliding mode observer is clearly shown in Fig. 4.8 (a). The nonlinear system is divided into three parts in this structure, including two nonlinear systems and a linear system. The first nonlinear system is the saturation function, and the second nonlinear system is the relationship between flux-linkage, phase current, and rotor position. And the linear system is the process of calculating the rotor position. The block diagram of SMO nonlinear structure can be transformed into Fig. 4.8 (b).

(a)

(b)
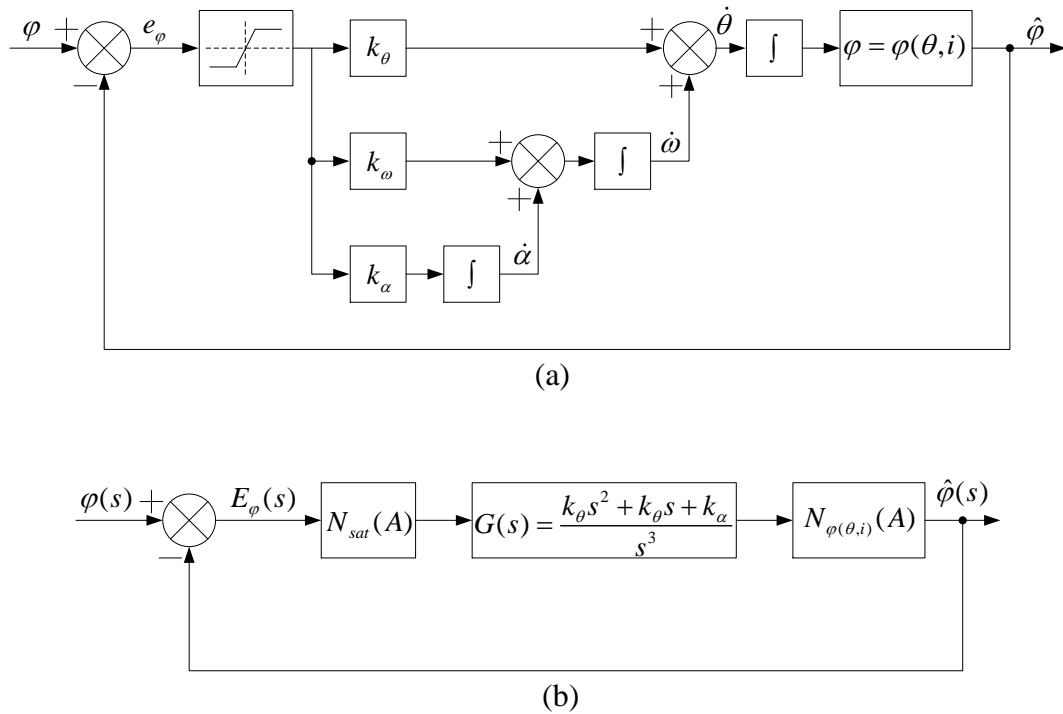
Fig. 4.8 Nonlinear block structure of sliding mode observer.

The transfer function of linear system can be expressed by the following equation.

$$G_L(s) = \frac{k_\theta s^2 + k_\theta s + k_\alpha}{s^3} \tag{4.34}$$

And the open-loop transfer function for the whole system can be expressed as,

$$G(s) = K_{sat} K_\varphi G_L \tag{4.35}$$

Where K_{sat} is the gain of $N_{sat}(A)$, and K_φ is the gain of $N_{\varphi(\theta,i)}$.

According to the frequency characteristic analysis method of linear system, the analysis method can also be applied to the nonlinear system. Therefore, the close-loop frequency characteristics of the system can be denoted as,

$$\frac{\hat{\varphi}(j\omega)}{\varphi(j\omega)} = \frac{N_{sat}(A)N_{\varphi(\theta,i)}(A)G_L(j\omega)}{1 + N_{sat}(A)N_{\varphi(\theta,i)}(A)G_L(j\omega)} \tag{4.36}$$

The characteristics function of system is,

$$1 + N_{sat}(A)N_{\varphi(\theta,i)}(A)G_L(j\omega) = 0 \tag{4.37}$$

So the major task is determining the expression and value range of two nonlinear systems. Firstly, for the saturation characteristics, the describing function can be expressed as,

$$N_{sat}(A) = \begin{cases} \dfrac{2k}{\pi}\left[\arcsin\dfrac{a}{A} + \dfrac{a}{A}\sqrt{1-(\dfrac{a}{A})^2}\right] & A > a \\ k & A \leq a \end{cases} \tag{4.38}$$

Where a is the layer boundary for the linear region, k is the slope of the linear region, and A is the amplitude of input waveform. As determined before, $k = 400$ and $a = 0.0025$. So substitute these values into (4.38), the saturation function characteristics can be revised as,

$$N_{sat}(A) = \begin{cases} 254.77\left[\arcsin\dfrac{1}{400A} + \dfrac{1}{400A}\sqrt{1-(\dfrac{1}{400A})^2}\right] & A > 0.0025 \\ 400 & A \leq 0.0025 \end{cases} \tag{4.39}$$

If $A \to \infty$, $N_{sat}(A) \to 0$. Then the gain range of saturation function is

$$N_{sat}(A) = (0, 400] \tag{4.40}$$

Secondly, the nonlinear part of flux-linkage, rotor position, and phase current has to be expressed by describing function. The characteristics of rotor position with the variation of flux-linkage at different currents are given in Fig. 4.9. It is obvious that $180°$ is unaligned position and $360°$ is aligned position. In order to calculate $N_{\varphi(\theta,i)}(A)$, the gradient of flux-linkage with the variation of rotor position at different currents is found first. Fig. 4.10 shows the maximum values and minimum values of gradients at each value of phase currents. By measuring the maximum value of the curve of the maximum

gains and minimum value of the curve of minimum gains, the value range of $N_{\varphi(\theta,i)}(A)$

can be found, and value range is

$$N_{\varphi(\theta,i)}(A) = [0.0012, 1.8022] \times 10^{-3} \qquad (4.41)$$

Then, substituting the maximum value of $N_{sat}(A)$ and $N_{\varphi(\theta,i)}(A)$ into (4.35), the transfer

function can be expressed as,

$$G(s) = \frac{0.72(k_\theta s^2 + k_\theta s + k_\alpha)}{s^3} \qquad (4.42)$$

Next, after properly estimating and selecting three SMO gains, the stability of the system

is analyzed by plotting the bode diagram of the transfer function (4.42). By calculating

the magnitude margin and phase margin of different groups of SMO gains, the most

suitable range of SMO gains can be determined.
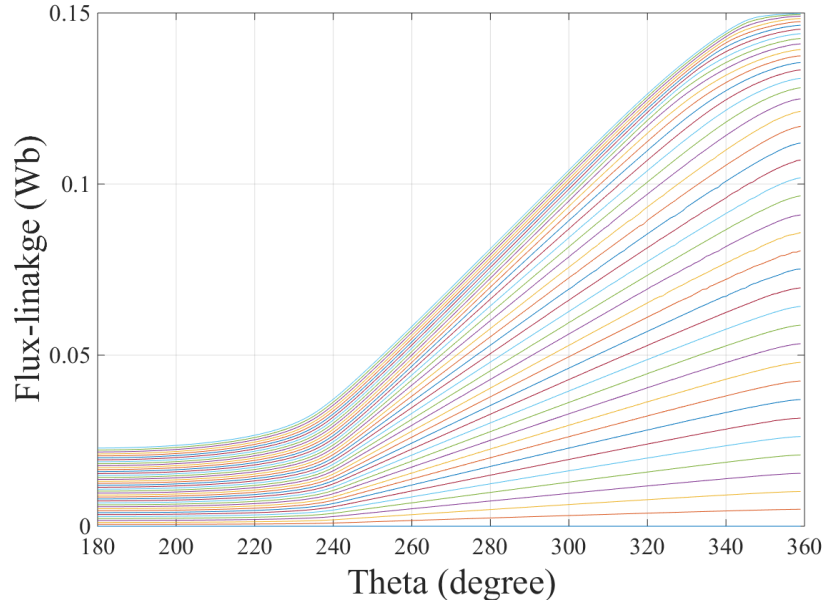
Fig. 4.9 The characteristics of flux-linkage-position-currents.
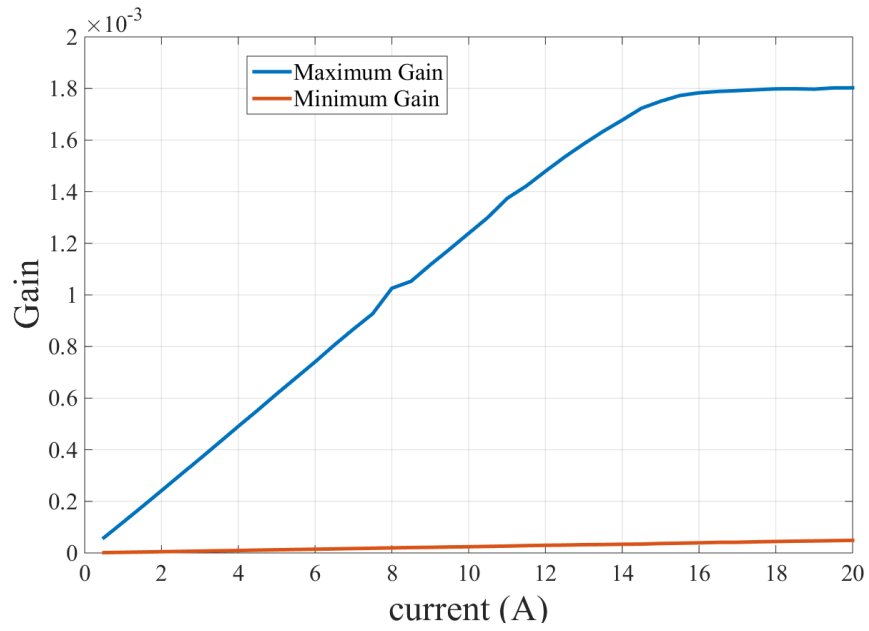
Fig. 4.10 The variation of $N_{\varphi(\theta,i)}(A)$ with phase current.

Several groups of SMO gains are listed in TABLE 4.1, and the Bode Diagram for each group of gains is given in Fig. 4.11.

TABLE 4.1 Comparison of stability of four groups of SMO gains

	SMO Gains Selection			Stability of the system		
	k_θ	k_ω	k_α	Gain Margin	Phase Margin	Stability
1	1000	100000	10000000	-17.2 dB	81.9°	Stable
2	10000	100000	10000000	-37.2 dB	89.9°	Stable
3	1000	1000000	10000000	-37.1 dB	45	Stable
4	1000	100000	100000000	2.58 dB	-28.2°	Unstable

First of all, by observing and comparing the Bode magnitude plot in Fig. 4.11, it can be seen that each gain is related to a specific range of frequency characteristics. If only modify the value of k_θ, comparing the Bode magnitude plot of group1 (blue line) with group 2 (orange line), the high-frequency characteristics are different (start from around 20 rad/s) while other ranges of frequency characteristics keep the same. Similarly, if only modify the value of k_ω, comparing the Bode magnitude plot of group 1 with group 3 (yellow line), the characteristics of middle-frequency range (from around 20 rad/s to 700 rad/s) have changed, and others stay the same. And if only change the value of k_α, comparing the Bode magnitude plot of group 1 with group 4 (purple line), the low-

frequency characteristics (from initial frequency to about 700 rad/s) are different and other ranges of characteristics will not change. Although the value of three SMO gains are in charge of different ranges of frequency characteristics, they have some common points, that is, the response will be faster when increasing the gains' value, and vice versa.
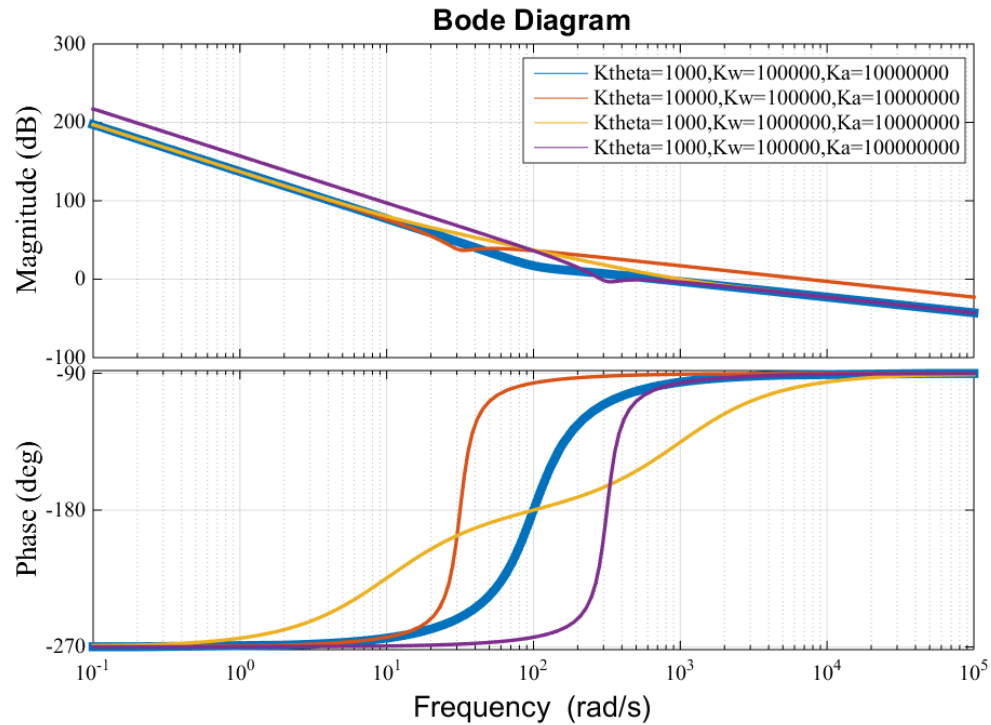

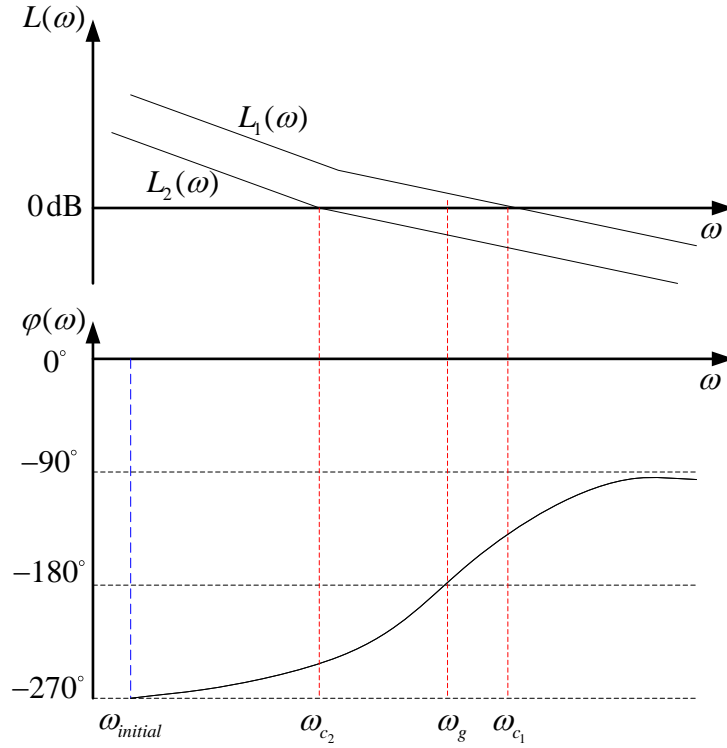Fig. 4.11 Bode Diagram of the comparison of four groups SMO gains.

Fig. 4.12 Bode Diagram of the initial magnitude and phase plot.

Secondly, it is important to demonstrate that the system is stable. According to the Nyquist stability criterion and logarithmic Nyquist plots, the logarithmic phase frequency characteristics have to cross the $-180°$ after the point where gain margin equals to 0, or the times of positive crossing need to equal to the times of negative crossing. Fig. 4.11 doesn't indicate the initial situation of phase frequency characteristics, so the magnitude and phase plot of the initial frequency are given in Fig. 4.12 $\omega_{initial}$, ω_c, and ω_g are defined as follows.

$$\omega_{origin} = 0 \qquad (4.43)$$

$$\angle G(j\omega_g) = -180°$$ (4.44)

$$-20\lg|G(j\omega_c)| = 0$$ (4.45)

The blue line indicates that phase frequency characteristics positively cross $-180°$ when the frequency equals to zero. For the same phase frequency characteristic, if the magnitude frequency characteristic is shown as $L_1(\omega)$, the phase frequency crosses $-180°$ before magnitude frequency reaching 0 dB. So the phase frequency crosses $-180°$ twice, the system is stable. Otherwise, if the magnitude frequency characteristic is shown as $L_2(\omega)$, the magnitude frequency reaches 0 before the phase frequency crossing $-180°$.

In this situation, the phase frequency only crosses $-180°$ once before magnitude frequency characteristic equals to 0 dB, so the system is unstable.

For a minimum-phase system, we can determine the stability by calculating the gain margin (GM) and phase margin (PM). If GM<0 and PM>0, the close-loop system is stable; if not, the close-loop system is unstable.

It is clearly shown in Fig. 4.11 that the phase frequency characteristics of group 1, group 2 and group 3 cross the $-180°$ before the corresponding magnitude frequency reaching 0 dB. And from TABLE 4.1, we can observe that all of the GMs of these three groups are smaller than zero, and the PMs are bigger than zero. It means that the systems with these three groups of SMO gains are stable. However, it is hard to compare the value of ω_g and

ω_c of the fourth group. By calculating the GM (GM>0) and PM (PM<0) of the fourth group, it shows that system with these three SMO gains cannot be stable. So when selecting the value of k_α, the designed value cannot be too large. Otherwise, the stability of the system will be affected.

In a word, by properly estimating and selecting the SMO gains, the sensorless control of detecting the rotor position can be realized with high accuracy and satisfying robustness.

Chapter 5

SIMULATION VERIFICATION

5.1. SIMULATION SETUP

In this chapter, the position sensorless control methods proposed in Chapter 3 and Chapter 4 are verified by simulation. Simulations are performed in MATLAB/Simulink environment. And simulation results of pulse injection method, sliding-mode observer method, and the combination of these two methods are presented.

The proposed position sensorless methods to estimate rotor position is applied on a 12/8 three-phase SRM. The combination of pulse injection method and SMO method is simulated for the entire speed range. At low speed, the pulse injection method is tested, while the SMO was verified at high speed. In the simulations, the load is adjusted to control the speed of the tested SRM.

The characteristics of the SRM are given in TABLE 5.1, and the parameters of controller are given in TABLE 5.2.

TABLE 5.1 System parameters of SRM drive

Power	2 kW
Rated speed	2,000 RPM
Stator resistance	0.05Ω
Stator poles	12
Rotor poles	8
Friction	0.002N·m·s
Inertia	0.005kgm^2

TABLE 5.2 Controller parameters

Turn-on angle	208°
Turn-off angle	340°
Proportional gain	0.03
Integral gain	0.1
Reference phase current	10A
DC-link voltage	150V
PWM switching frequency	10 kHz

5.2. SIMULATION RESULTS

5.2.1. LOW-SPEED OPERATION WITH PULSE INJECTION METHOD

At low speed operation, the rotor position and speed estimation is realized by pulse injection method. Fig. 5.1 shows the control structure of SRM based on pulse injection method. In order to determine the initial rotor position, pulses have to be injected to three phases simultaneously to calculate the inductance amplitude. According to TABLE 3.3, the initial position can be found by comparing the values of inductance of the three phases. And as introduced in section 3.3.2, pulses are injected to three phases in sequence at low-speed operation, and the rotor position can be calculated by (3.6). The parameters of pulse injection module are listed in TABLE 5.3. And the sample time of the position calculation module is $1\times10^{-4}s$.

TABLE 5.3 Parameters of pulse injection module

Initial position detection	Pulse frequency	1 kHz
	Pulse amplitude	150V
	Pulse width	$5\times10^{-4}s$
Turn-on angle		0°
Turn-off angle		120°
θ_s		40°
Low-speed position detection	Pulse frequency	5 kHz
	Pulse amplitude	150V
	Pulse width	$4.5\times10^{-5}s$
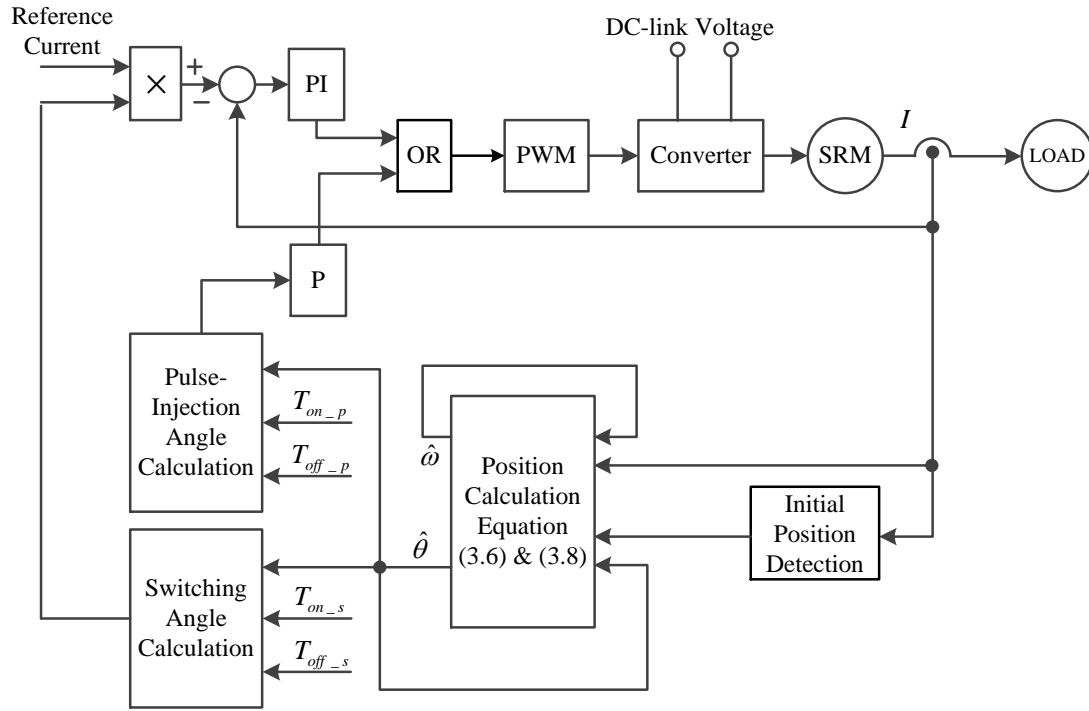
Fig. 5.1 Control structure of SRM based on pulse injection method.

Fig. 5.2 shows current waveforms of three phases with pulse injection. As shown in Fig. 3.1 and Fig. 3.5, for each position region, it has specific sensing phase and active phase. So from Fig. 5.2 (a), when the pulses are injected into phase A to detect the rotor position, phase B is under conduction firstly, and the active phase is switched to phase C. There are two reasons to explain why the turn-off angle for active phase has to be ahead of turn-on angle of sensing phase. Firstly, before the pulses injecting to one phase, the phase current has to be zero. Secondly, it takes time for phase current dropping to zero, so certain time has to be kept put to ensure that the phase current drops to zero before injecting the current. When the current of phase B drops to zero, the pulses are injected into phase B to

sense the rotor position. The phase C is still used as active phase in the first half part, and then the active phase is switched to phase A. And conditions of the phase C can be deducted with the same analysis. It is shown that the current of active phases is regulated at 10A when SRM operates at the low speed of 275 RPM. The magnitude of pulse injection current varies from 0.5A to 3.5A, and it is relatively small compared to active phase current. However, the disadvantage of injected pulse current is that this current produces a negative torque.

The amplitude of the injected pulse current represents the variation of phase inductance, and the position information can be detected by phase inductance. Equation (3.6) is used to calculate the relative phase inductance and rotor position by the measurement of injected pulse current. Fig. 5.2 (b) shows the current waveform of phase A with the variation of phase A rotor position. As designed previously, the normal conduction angle is from 208° to 340°, and the pulse injected angle is from 0° and 120°.

Fig. 5.3 (a) shows the comparison of actual position and estimated position without considering the saturation region of phase inductance (the algorithm is equation (3.5)). It is shown that there is mismatching between actual and estimated position. The position error is shown in Fig. 5.3 (b), and the average error is around 6°. Comparatively, Fig. 5.4 shows the comparison of actual position and estimated position under consideration of the saturation region of phase inductance. It is shown that the position error is reduced by using the algorithm that considers the saturation region.

(a)

(b)
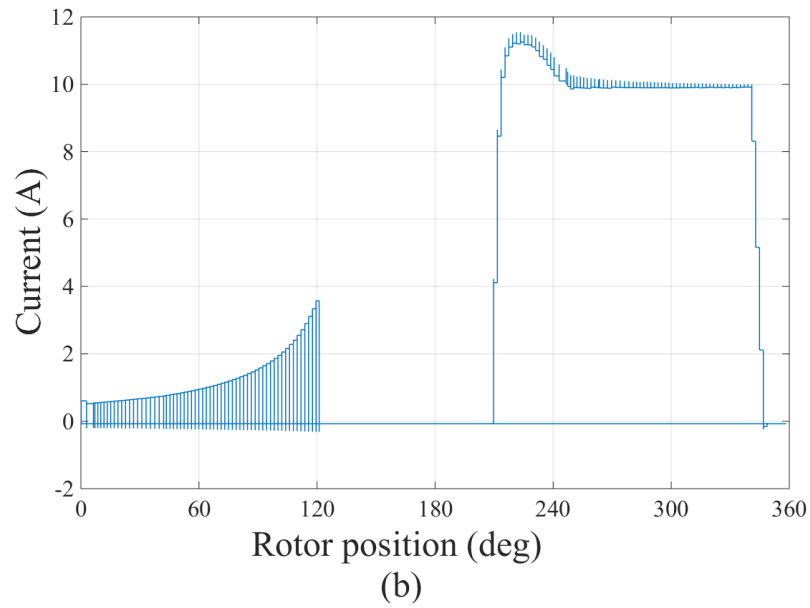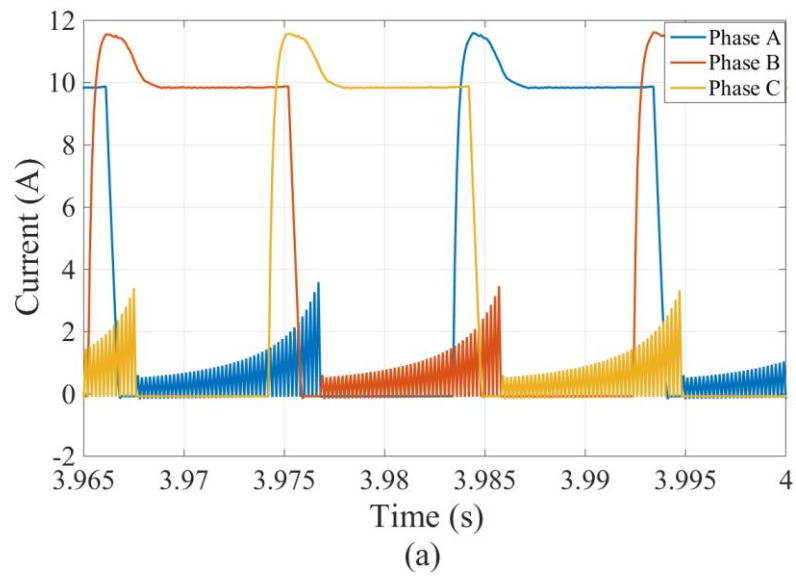
Fig. 5.2 (a) Three phases current profiles of pulse injection method at steady-state; (b)

Phase A current profiles versa Phase A rotor position.
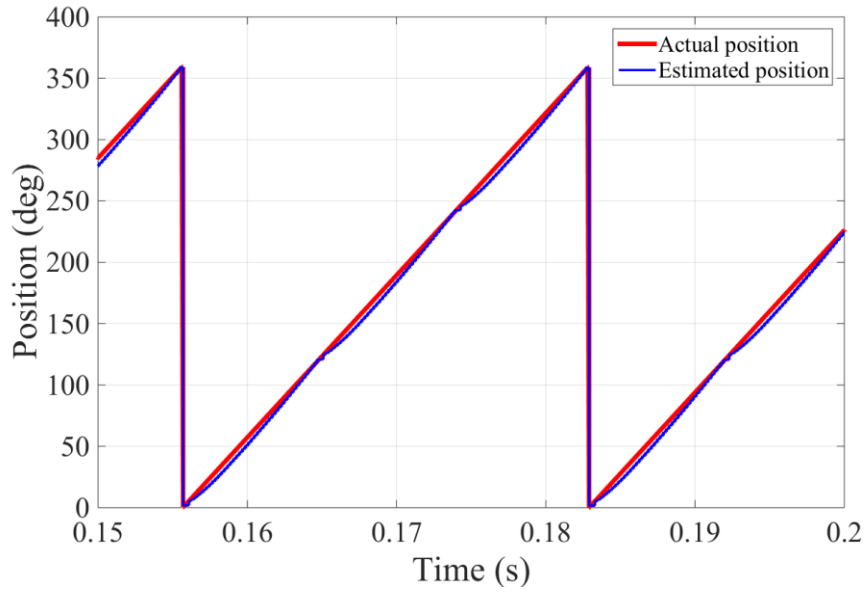
(a) Comparison of actual and estimated position region.
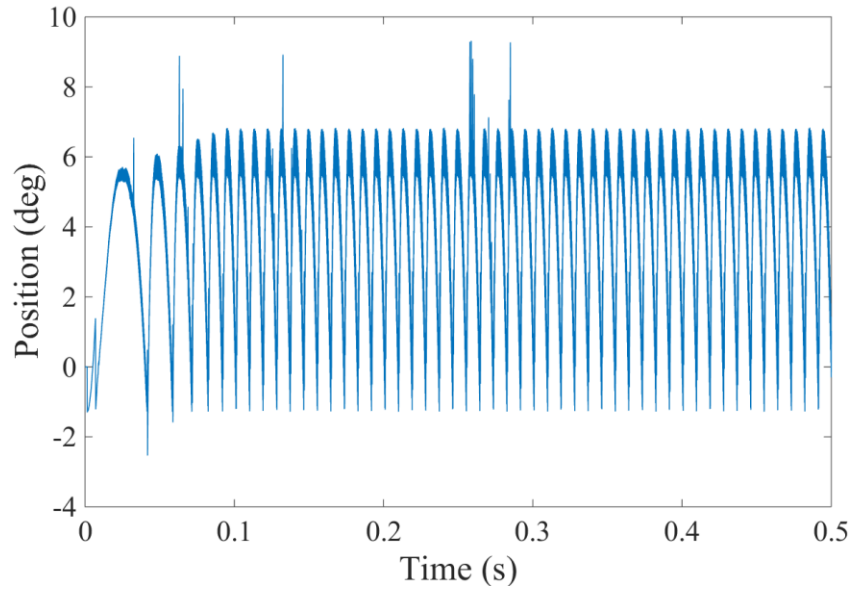
(b) Corresponding position error.

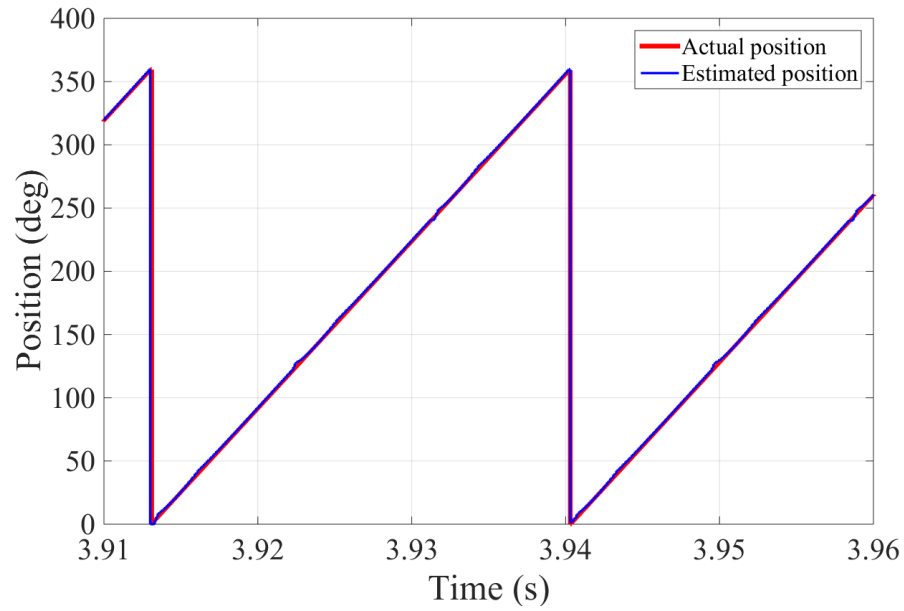Fig. 5.3 Simulation results at 275 RPM without considering saturation.

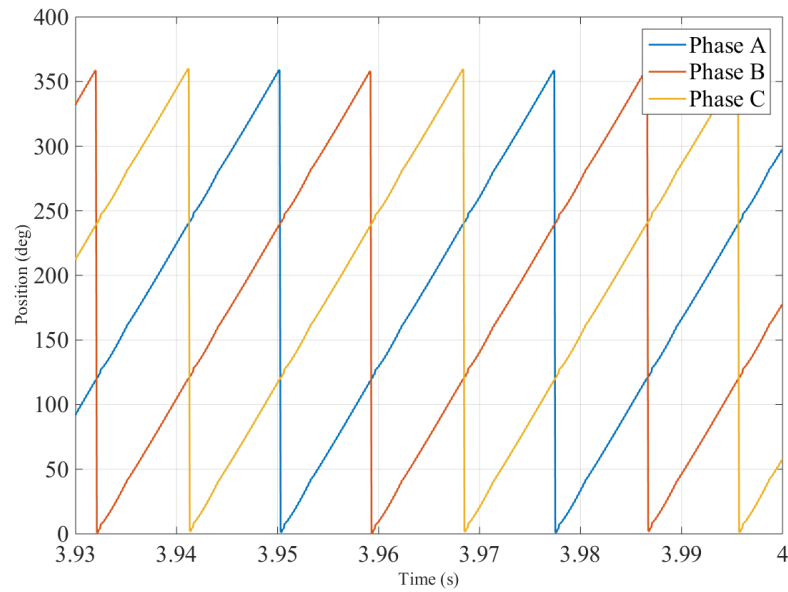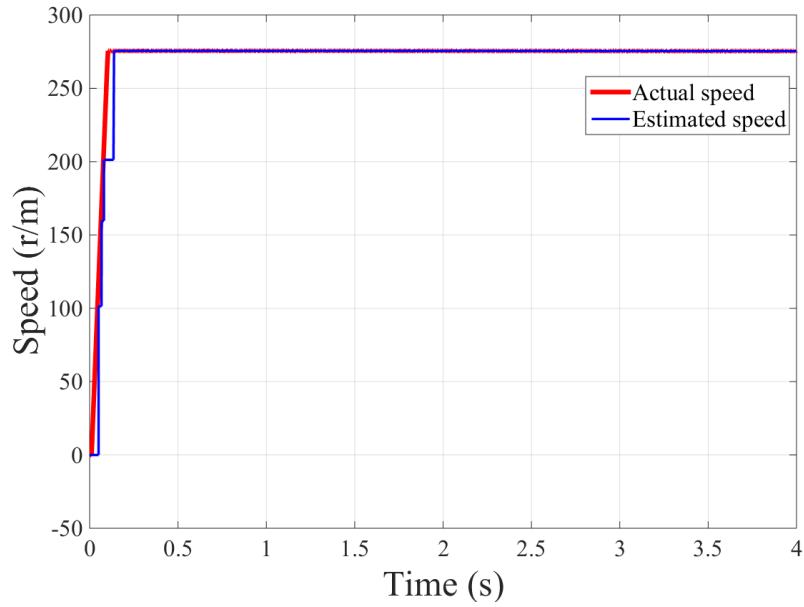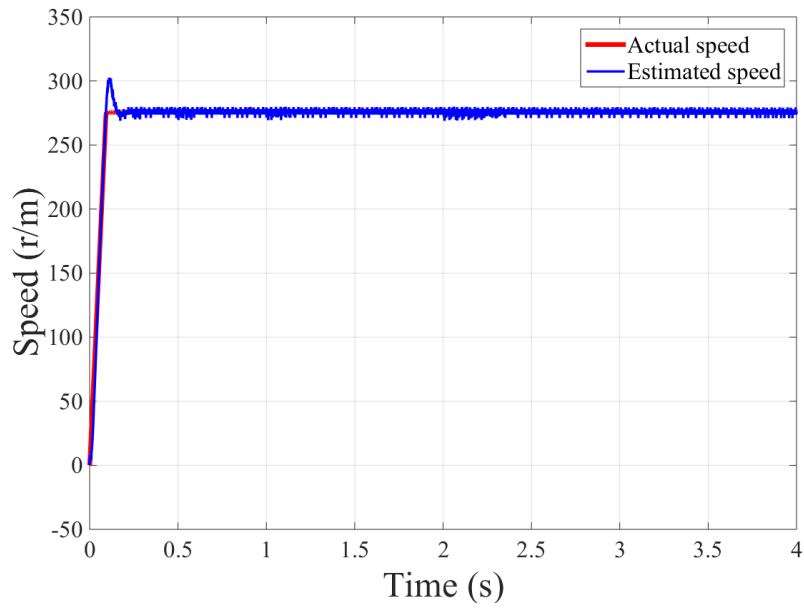Fig. 5.4 Simulation results of the rotor position estimation at 275 RPM.

Fig. 5.5 Three phases estimated rotor position profiles at 275 RPM.

(a) rotor speed estimation at 275 RPM without PLL.

(b) rotor speed estimation from 0 RPM to 275 RPM by PLL.

Fig. 5.6 Simulation results of the rotor speed estimation at 275 RPM.
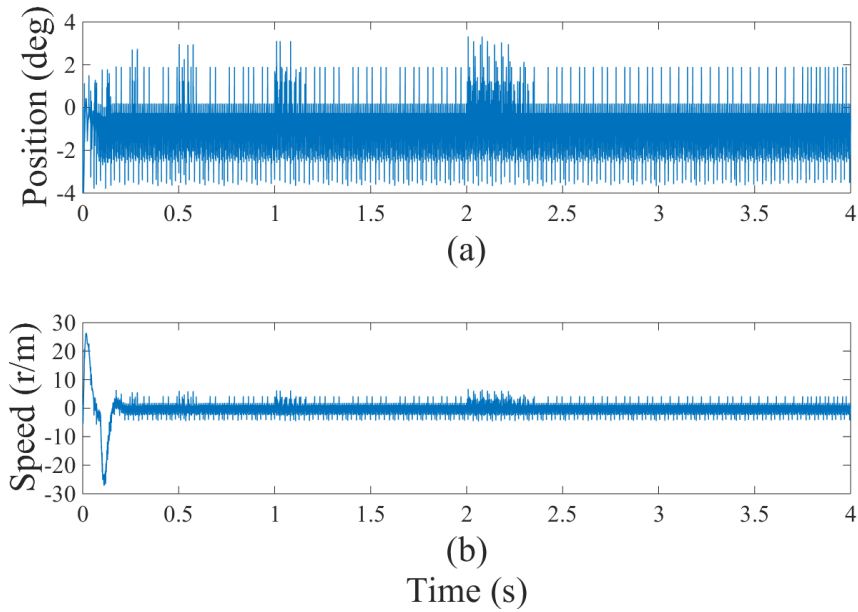
Fig. 5.7 Simulation results of the estimation error of the position and speed at 275 RPM

(a) position error; (b) speed error.

Fig. 5.5 shows the estimated rotor position information of three phases, which verifies the control scheme in Fig. 3.5. Fig. 5.6 shows the simulation results of speed estimation. Fig. 5.6 (a) shows the rotor speed estimation results using equation (3.8) while Fig. 5.6 (b) shows the results from PLL. Since the speed is estimated by a step of 30° mechanical degree from Fig. 5.6 (a), the estimated speed did not track actual speed well during accelerating region. When the SRM operates at 275 RPM, the estimated speed can perfectly match the actual speed. However, the result from PLL can almost exactly track actual speed except overshoots. The overshoots occur when the system operates from the standstill and reaches 275 RPM. However, the overshoot has little effect on the stability

of the whole system. The disadvantage of PLL method is that the chartering is higher compared with the speed estimation method using (3.8). By examining the merits and shortages of these two approaches, speed estimation using PLL is more suitable to be applied to this system.

Fig. 5.7 describes the estimation error of position and speed obtained from PLL. Both the position error and speed error are comparatively small at steady-state. The position error varies between -4° to 2° except some spikes to around 3.5°. The speed error ranges from -5 RPM to 3 RPM at steady state, and the maximum overshoot reaches 26 RPM.

There are some spikes appearing in the position error. The reason for this phenomenon is that the algorithm needs response time when switches from one active phase to another. However, the response time is short, and the position error is not significant. In this case, the accuracy of pulse injection method to detect rotor position is acceptable, and it is desired to be applied to the low-speed operation.

5.2.2. HIGH-SPEED OPERATION WITH SLIDING MODE OBSERVER METHOD

At high-speed operation, the sensorless position detection is realized by sliding mode observer. The control structure block diagram of the whole system is shown in Fig. 5.8. The selection of observer gains is listed in TABLE 5.4, and the Bode diagram of the system with these gains is presented in Fig. 5.9. Since the GM<0 and PM>0, it means that the system is stable. So the selection of SMO gains is reasonable.
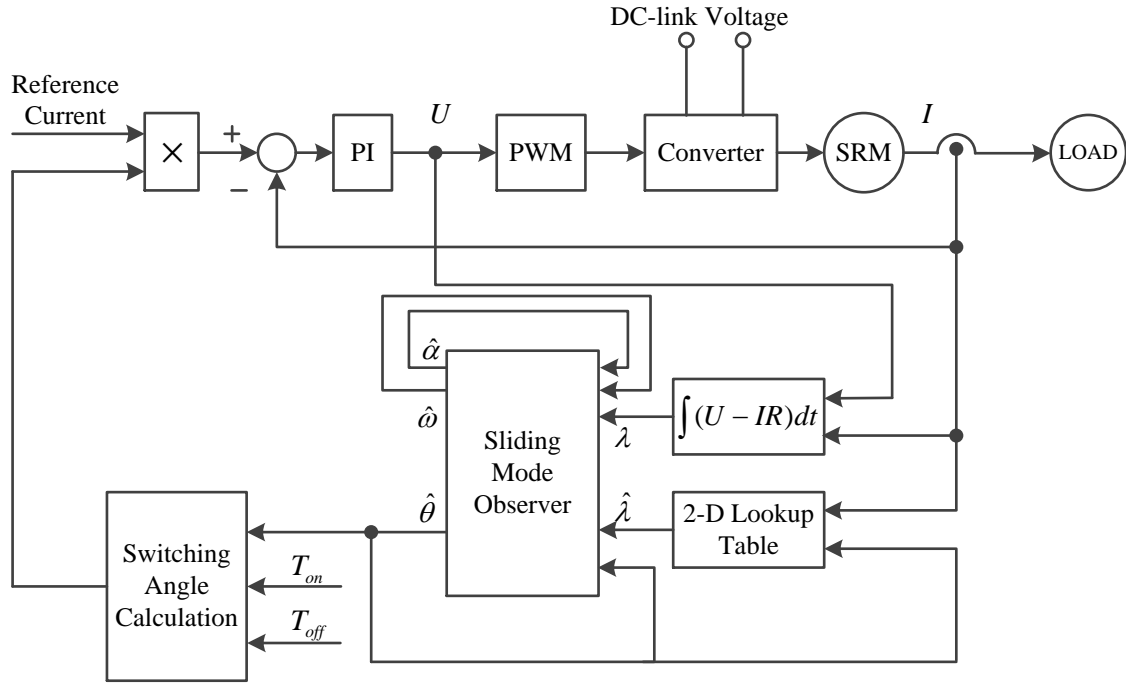
Fig. 5.8 Control structure of SRM based on SMO.

TABLE 5.4 Design of observer gains

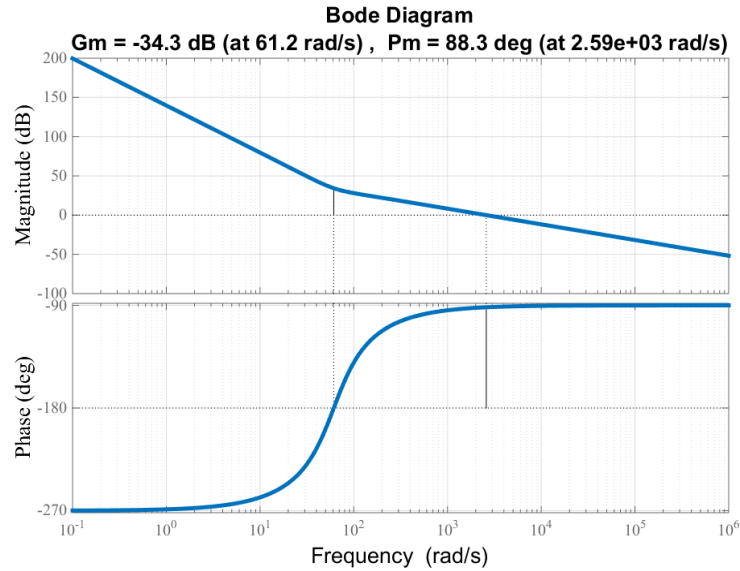| Parameter	Value	Unit
k_θ	3600	Deg/s
k_ω	2.7×10^5	Deg/s^2
k_α	1.35×10^7	Deg/s^3

Fig. 5.9 Bode diagram of the system with the selection of SMO gains in TABLE 5.4.

The simulations are performed at a mechanical speed of 2,000 RPM to verify the effectiveness and accuracy of the proposed SMO method. Since it is a 12/8 SRM, the electric speed reference is set to 16,000 RPM and the SRM is driven from 0 RPM to an electric speed of 16,000 RPM with the acceleration of 19,200 Deg/s^2.

The actual flux-linkage can be calculated by inverting (1.14). And the estimated flux linkage can be obtained from 3D look-up table. This 3D look-up table needs information of phase currents and rotor position to search the corresponding phase flux-linkages. Phase currents are measured by current sensors, and the current rotor position estimated from former moment is the input of the look-up table. In this way, the flux-linkage can be obtained. Fig. 5.10 shows the comparison of estimated flux-linkage and actual flux-linkage at steady state. It is shown that the estimated and actual flux-linkage are almost

overlapped. Although there are some errors between estimated flux-linkage and actual flux-linkage, these errors will be minimized by SMO algorithm, and flux-linkage errors are important items to calculate the estimated rotor position and speed. Fig. 5.11 depicts the current profiles of three phases. The current reference is set to 10A, and it is clear that the current is regulated around 10A at steady state.

Fig. 5.12 shows the estimated position and actual position at steady state and Fig. 5.13 shows the comparison of estimated speed and actual speed. Fig. 5.14 shows the position error and speed error during the whole executing period. Although both the position error and speed error oscillate during acceleration period, the maximum errors are acceptable, and they are about 20° and 40 RPM, respectively. Both the speed error and position error occurs at the beginning of acceleration. The estimated position and actual position are overlapped well when the system operates at high-speed steady state. The average position error at steady state is around 1° with chattering from 0° to 2°. When the speed reaches 2,000 RPM, the average speed error is 0 RPM with chattering between -1 RPM to 1 RPM.

Simulation results demonstrate the effectiveness of SMO method to estimate the position and speed at high-speed operation. When the system operates at steady state, the position error and speed errors are 0.56% and 0.05%, respectively. The estimated results can precisely track the actual value with short response time. Therefore, the SMO estimation is achieved with high accuracy and fast convergence. The chattering of estimated position

and speed are comparatively insignificant, and they do not have much influence on the performance of the whole system.
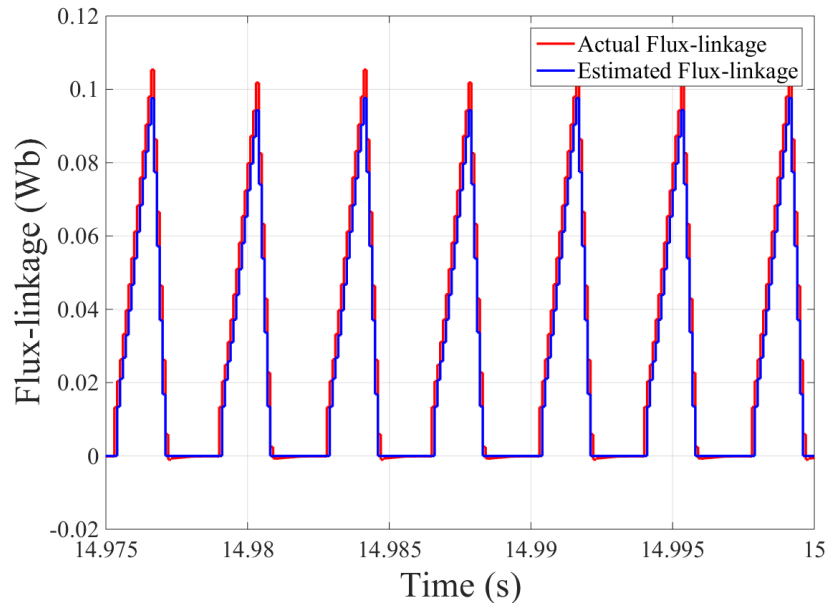
Fig. 5.10 The comprison of actual flux-linkage and estimated flux-linkage at steady-state.
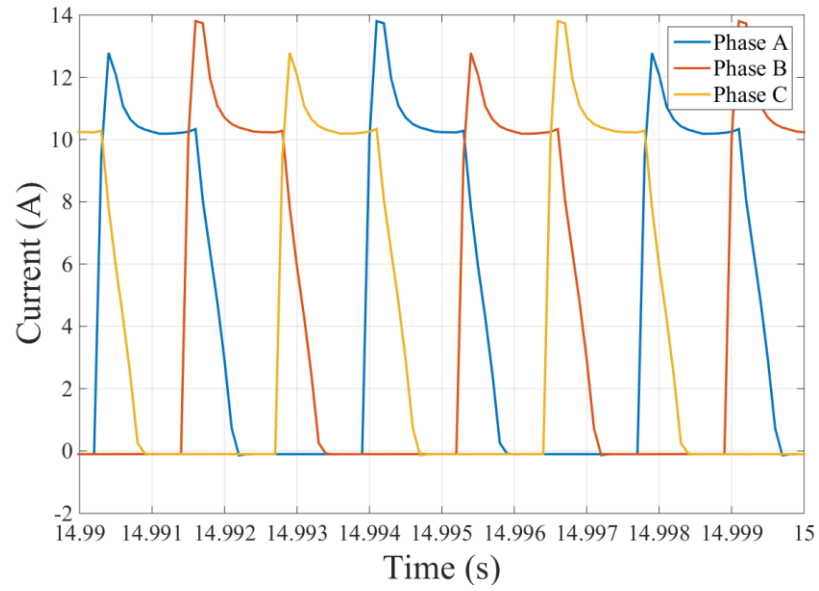
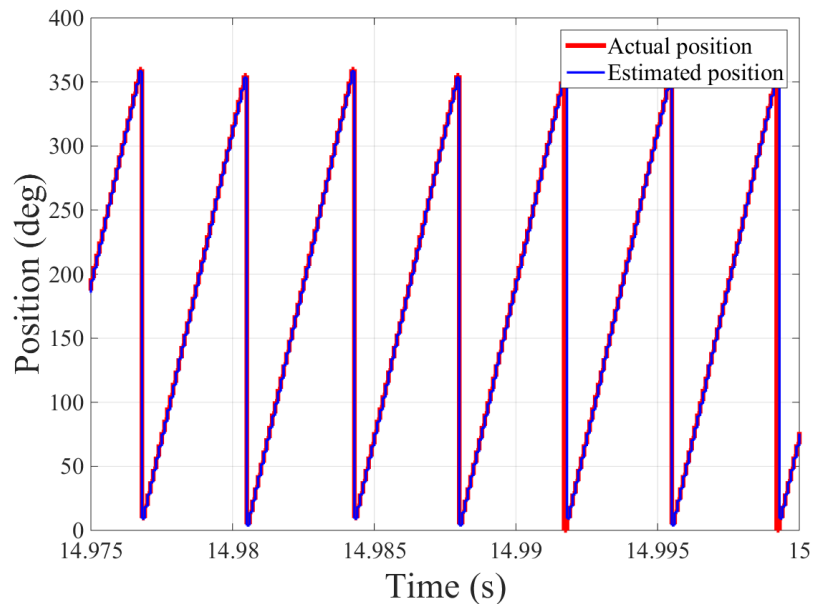Fig. 5.11 The mesurements of three phases currents at steady-state.

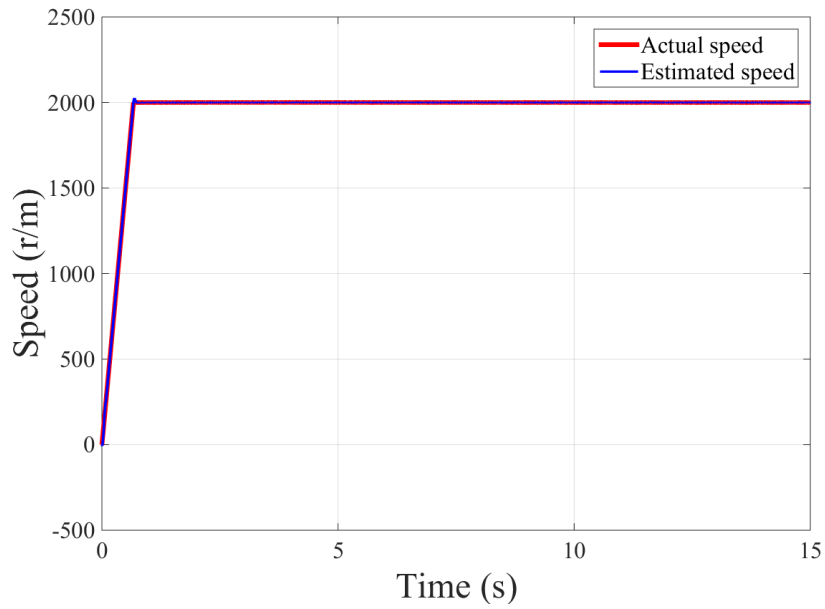Fig. 5.12 Simulation results of the rotor position estimation at 2,000 RPM.

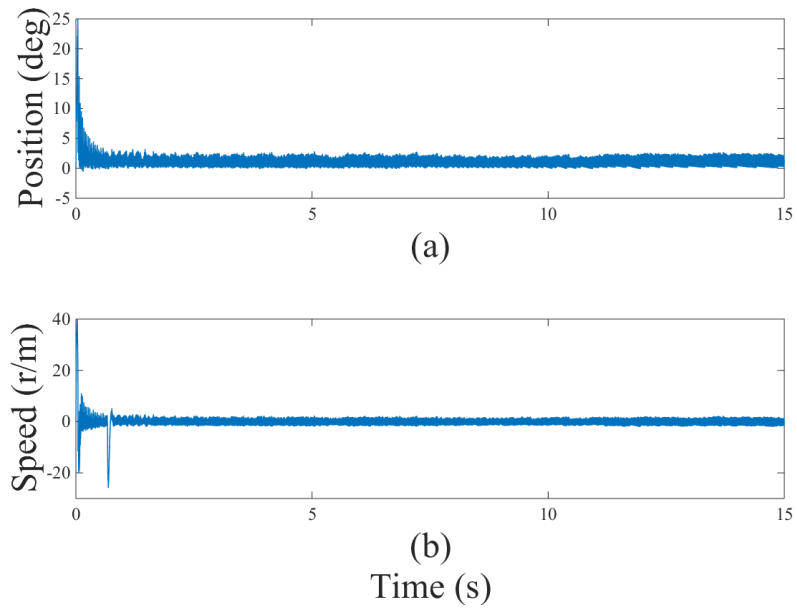Fig. 5.13 Simulation results of the rotor speed estimation at 2,000 RPM.

Fig. 5.14 Simulation results of the estimation error of the position and speed at 2,000

RPM (a) position error; (b) speed error.
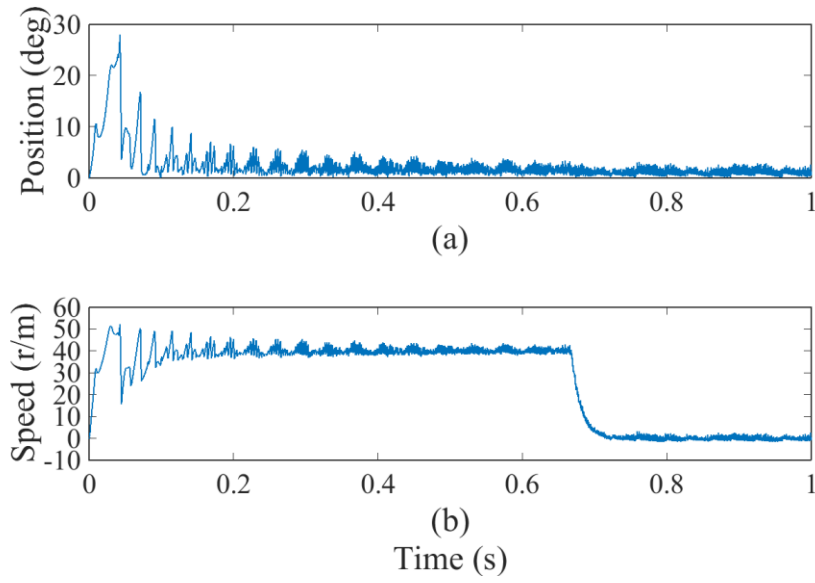
Fig. 5.15 Position and speed error of 2-order sliding-mode observer.
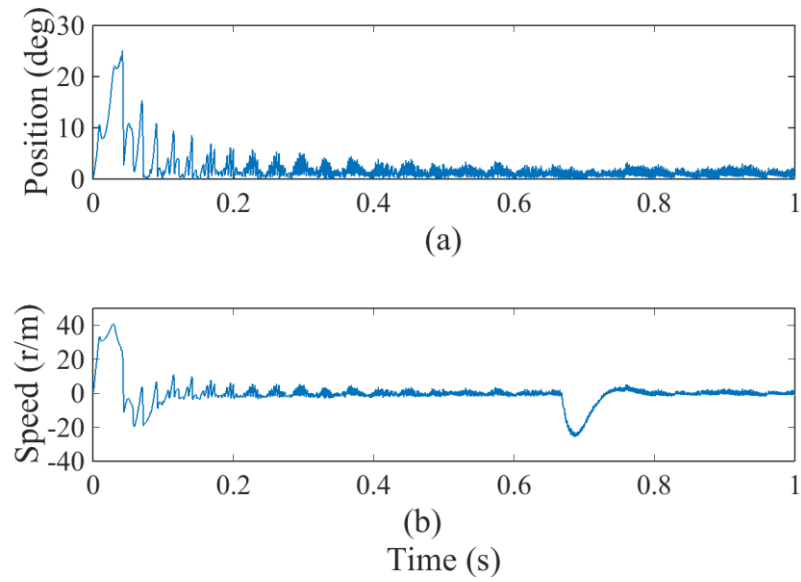
Fig. 5.16 Position and speed error of 3-order sliding-mode observer.

A sliding-mode observer with second order PLL is tested to show the improvement of the proposed third order sliding-mode observer. The position errors and speed errors are shown in Fig. 5.15 and Fig. 5.16, respectively. It is shown that during acceleration period, and the speed error keeps around 40 RPM. However, when the third order SMO is applied, the estimated speed can well track the actual speed during acceleration period. The accuracy of the third order SMO also shows a little improvement over the second order SMO.

5.2.3. THE COMBINATION OF THE TWO ESTIMATION METHOD FOR ENTIRE SPEED RANGE

Both pulse injection method and sliding-mode observer have their advantages at particular speed range. Therefore, it is reasonable to combine these two methods together to detect rotor position of the entire speed range. Pulses are injected to idle phases to get the rotor position information when SRM operate at low speed, and the control method switches to sliding-mode observer when the speed exceeds a certain speed. In this way, the rotor position and speed are precisely estimated.
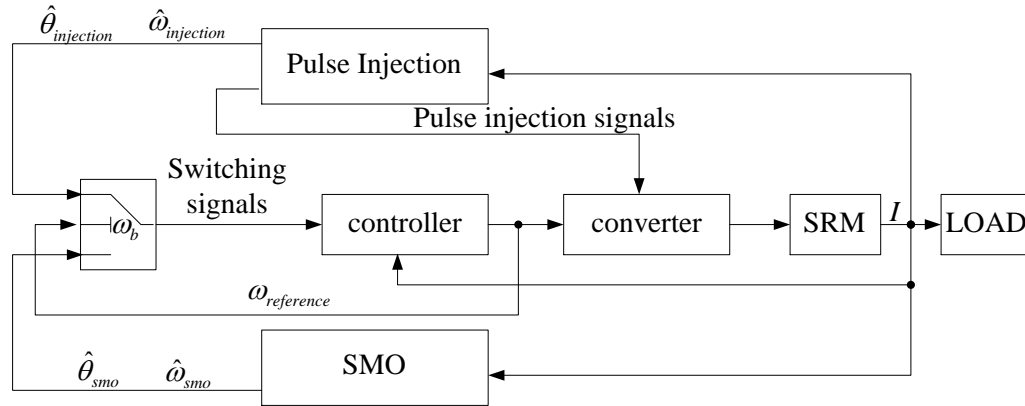
Fig. 5.17 control structure of hybrid sensorless control method.

Fig. 5.17 shows the control structure of the whole system by combining the two sensorless control methods together. Where ω_b is the preset speed. When rotor speed is below ω_b, pulse injection method is applied to detect the rotor position and speed. When rotor speed exceeds ω_b, sliding mode observer is utilized. The speed threshold ω_b is set to 500 RPM.

Fig. 5.18 (a) illustrates the comparison of estimated and actual position during acceleration period. It is shown that the estimated and actual positions are almost overlapped. Pulse injection method can precisely estimate the rotor position during low-speed operation. And Fig. 5.18 (b) shows the simulation results at 1000 RPM. Since the estimated and actual positions are overlapped well, the SMO method is proved to be able to estimate rotor position with high accuracy at high-speed operation.
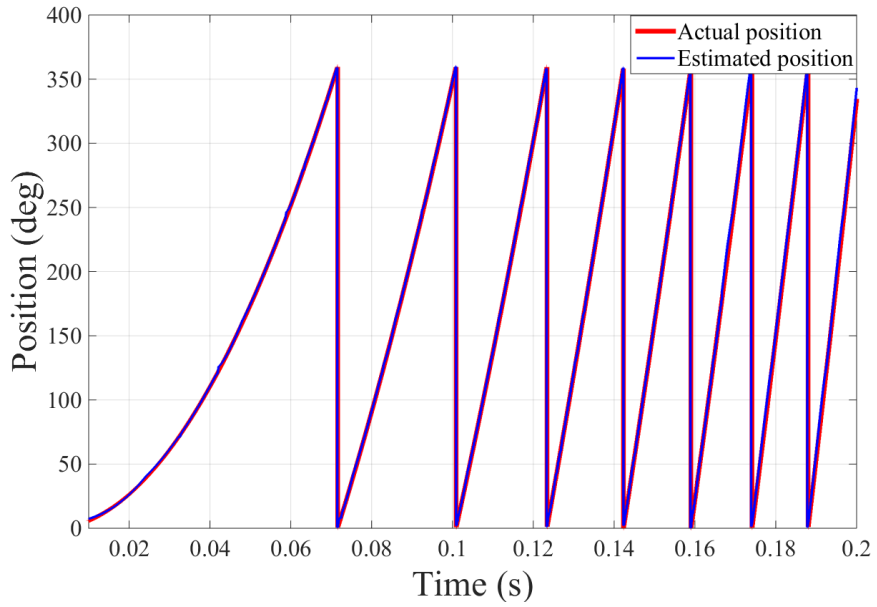
(a) Simulation results of the rotor position estimation by pulse injection method.
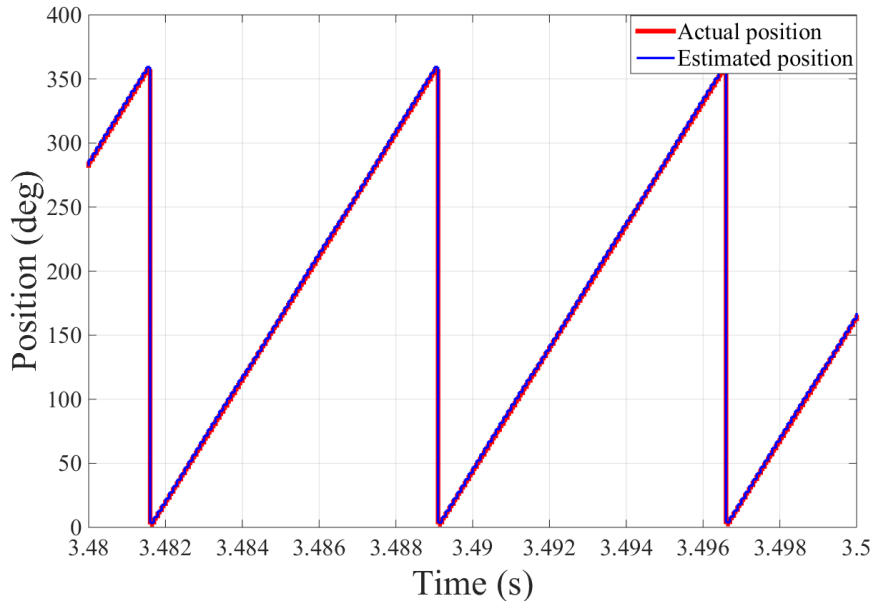
(b) Simulation results of the rotor position estimation by sliding mode method.

Fig. 5.18 Simulation results of rotor position estimation.

Fig. 5.19 shows the simulation results of estimated and actual speed. As is shown, estimated speed precisely tracks the actual speed except a slight overshot when the speed reaches the steady-state speed. Since the estimated and actual speeds are almost overlapped during the whole period, high speed accuracy of both the pulse injection method and the SMO method is indicated.
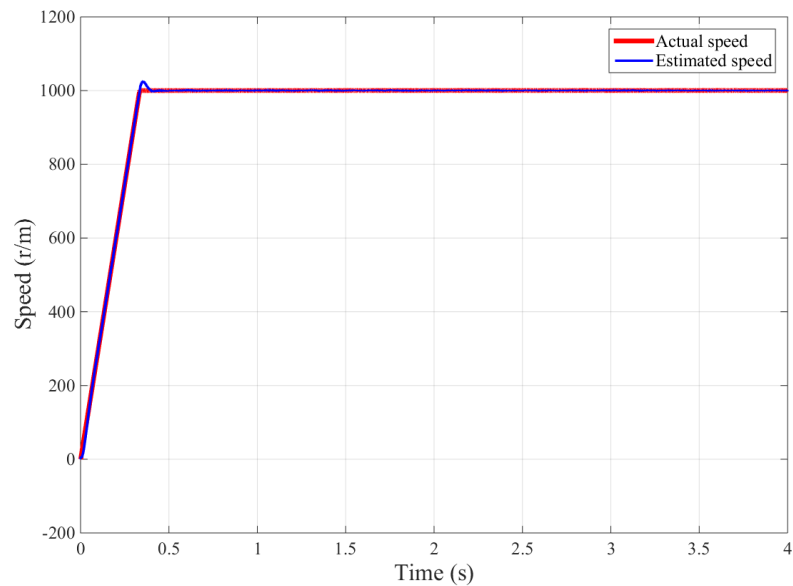
Fig. 5.19 Simulation results of the rotor speed estimation from 0 RPM to 1000 RPM.

Fig. 5.20 shows the position error and speed error. It is shown that both the position error and speed error are insignificant. For every electrical cycle (360°), the average position error at acceleration period with pulse injection method is about -0.3°. When switching the pulse injection method to SMO method, the position error reaches its maximum value about -9.5°. After convergence, the average position error using SMO method is about -

1.2° with chattering from -0.5° to -3.5°. The speed error of pulse injection method oscillates between 4 RPM and -6 RPM except the overshot to 28 RPM at startup point. When the speed reaches the steady state speed, the overshot of speed error reaches -28 RPM. And then the speed error of SMO method is about 0.5 RMP with chattering from 1.5 RPM to -2 RPM.
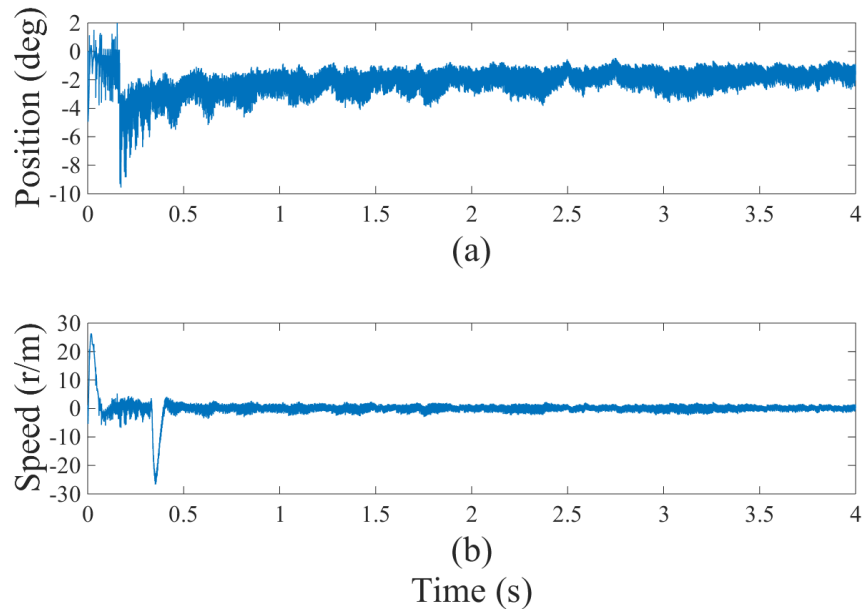

Fig. 5.20 Simulation results of the estimation error of the position and speed from 0 RPM to 1000 RPM (a) position error; (b) speed error.

In order to verify the effectiveness of proposed combination method, simulation results at different speeds are given. The simulation results at the speed of 2000 RPM are shown in Fig. 5.21 to Fig. 5.23 and the simulation results at the speed of 4000 RPM are shown in Fig. 5.24 to Fig. 5.26.

Fig. 5.21 and Fig. 5.24 show the comparison of actual and estimated rotor position at the speed of 2000 RPM and 4000 RPM respectively. No matter at what speed the system operates, the estimated position and actual position are overlapped well. High accuracy of rotor position estimation is indicated.

Fig. 5.22 and Fig. 5.25show the comparison of estimated and actual speed at 2000 RPM and 4000 RPM respectively. It is shown that estimated speed can track actual speed precisely when the steady-state speed is either at 2000 RPM or 4000 RPM.

Fig. 5.23shows the position error and speed error when the steady-state speed of the system is 2000 RPM. The average position error at 2000 RPM is about -0.6° with chattering from -1.4° to – -0.2°. And the speed error is about 0.1 RPM with chattering from 1 RPM and -1 RPM at steady state.

Fig. 5.26 shows the position and speed errors at 4000 RPM. The average position error at 4000 RPM is about -0.1° with chattering from -0.4° to -0.2°. And the speed error is about 0.05 RPM with chattering from 0.6 RPM and -0.6 RPM at steady state.

So the simulation results verify that the combined sensorless control method, namely pulse-injection for low speed and SMO for high speed, have the capability to estimate rotor position and speed with high reliability.
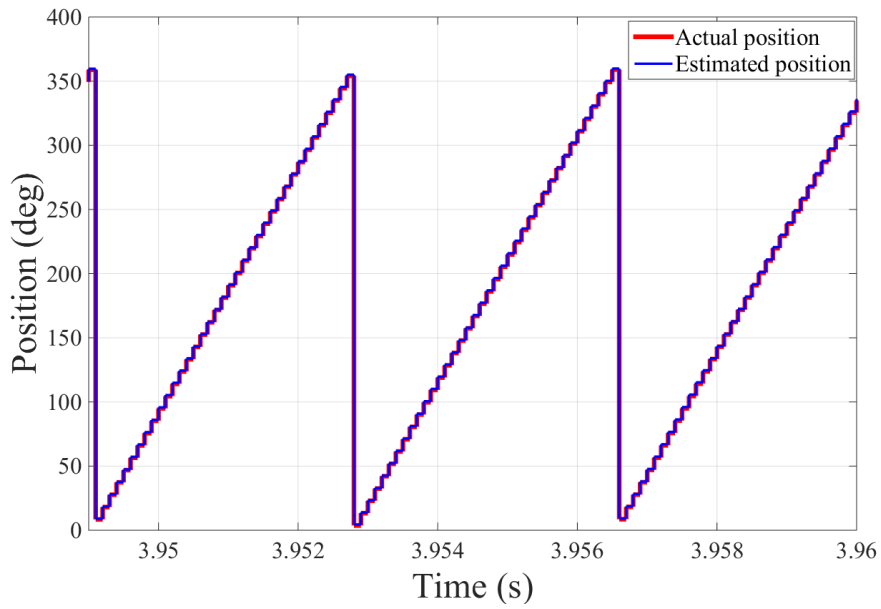
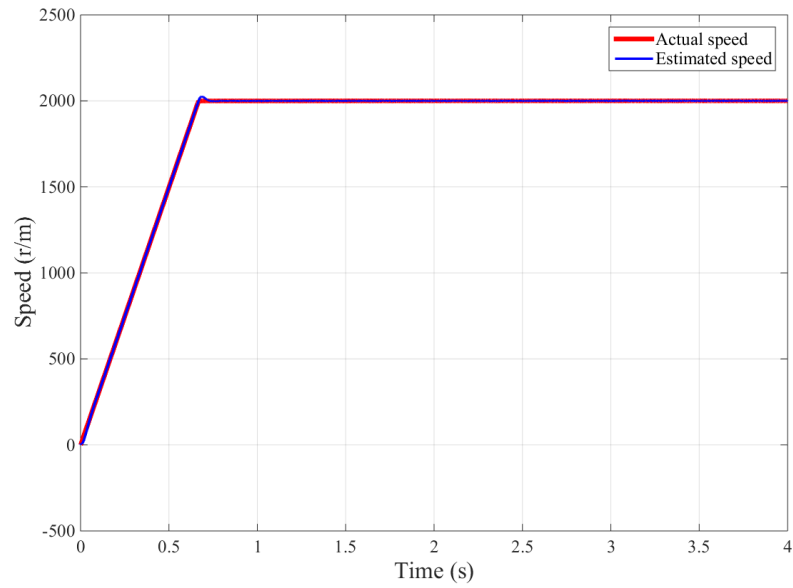Fig. 5.21 Simulation results of rotor position estimation at the speed of 2000 RPM.

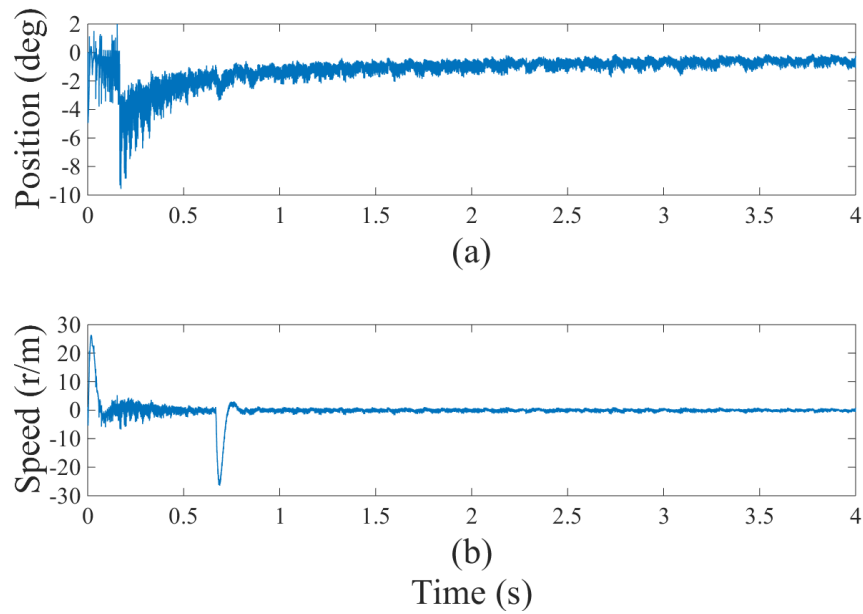Fig. 5.22 Simulation results of the rotor speed estimation from 0 RPM to 2000 RPM.

Fig. 5.23 Simulation results of the estimation error of the position and speed from 0 RPM

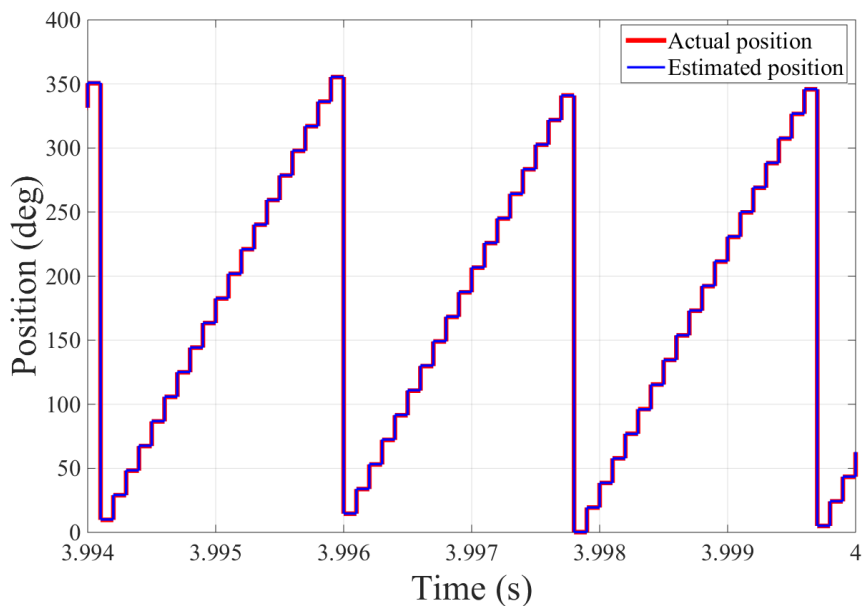to 2000 RPM (a) position error; (b) speed error.

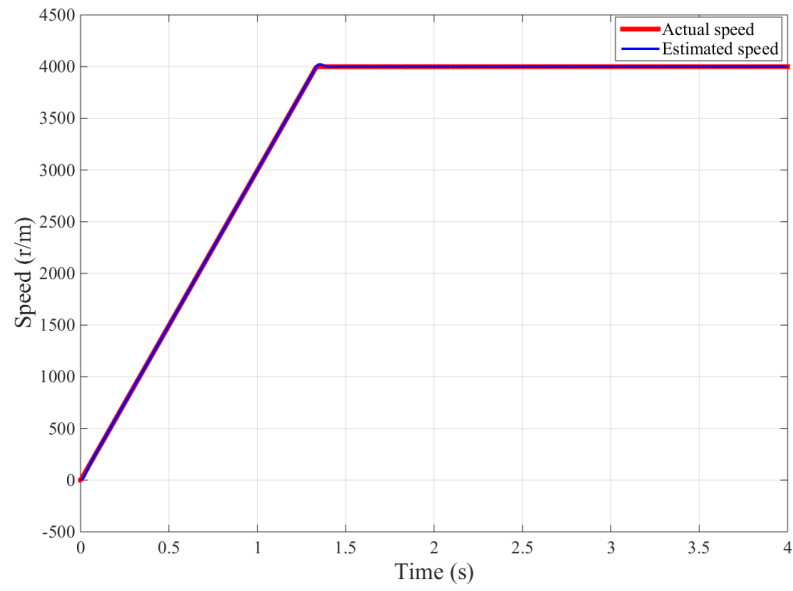Fig. 5.24 Simulation results of rotor position estimation at the speed of 4000 RPM.

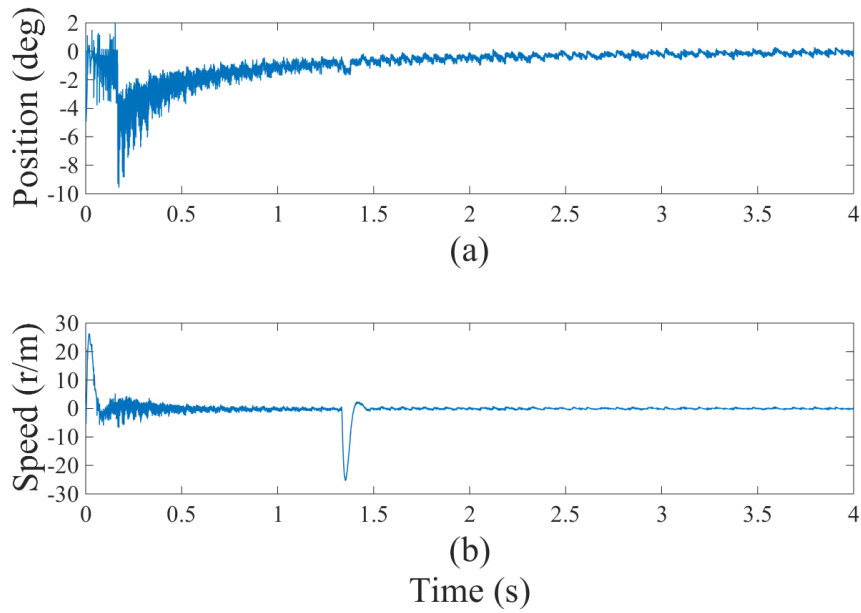Fig. 5.25 Simulation results of the rotor speed estimation from 0 RPM to 4000 RPM.

Fig. 5.26 Simulation results of the estimation error of the position and speed from 0 RPM

to 4000 RPM (a) position error; (b) speed error.

In order to test the transient response of the proposed combination sensorless control method, simulation results of changing the speed during operation period are given. As shown in Fig. 5.27, the speed changes several times during operation period. In the beginning, the speed accelerates to 300 RPM, and after a short time operation, it continues to accelerate to 2000 RPM. The system operates at 2000 RPM for a few seconds, and then the rotor starts to slow down. The speed decreases back to 300 RPM. In the whole process, the estimation method switches from pulse injection to SMO (or from SMO to pulse injection) at 500 RPM.

A group of figures in Fig. 5.28 show the comparison of estimated and actual positions, including the whole operation period and the points starting to accelerate and decelerate. Fig. 5.28 (a) shows the comparison of estimated and actual positions for the whole operation period. It is shown that the actual and estimated positions are almost overlapped both at low-speed and high-speed operation. Fig. 5.28 (b) shows the rotor position estimation results when the speed starts to accelerate from 300 RPM. It also includes the moment when the sensorless control method is switching from pulse-injection to SMO. Furthermore, Fig. 5.28 (c) presents the comparison of estimated and actual rotor positions when the speed starts to decelerate from 2000 RPM. And Fig. 5.28 (d) describes the simulation results when the speed stabilizes at 300 RPM. It is evident to observe that the estimated and actual positions are always almost overlapped no matter what state of the system it is.

Fig. 5.29 describes the estimation errors during the whole process. The rotor position error is shown in Fig. 5.29 (a). The rotor position errors oscillate from -4° to 2° when the pulse injection method is applied. And when the SMO method is used to detect rotor position and speed, the position error is minimized when increasing the rotor speed and the position error is enlarged when decreasing the rotor speed. It is shown in this figure that the position error of high-speed operation is smaller than that of low-speed operation. It further demonstrates the previous comments that the position error is reduced when increasing the rotor speed. The speed error is shown in Fig. 5.29 (b). It is shown that the overshoots occur when the rotor starts to accelerate and reach the setting speed. The absolute value of overshoots is about 27 RPM. Besides, the speed error at different speeds can be explicitly compared when the SMO is applied. And it is shown that the speed error at high-speed operation is smaller than that at low-speed operation.
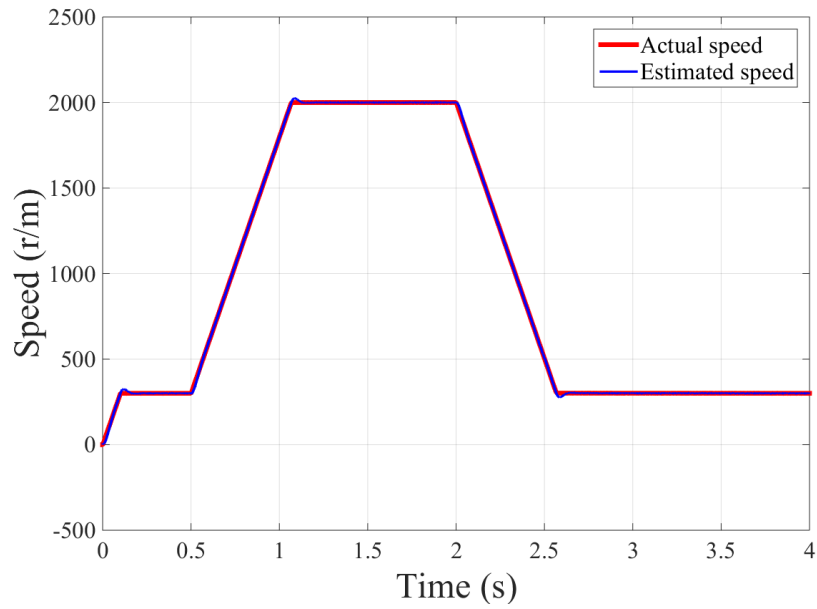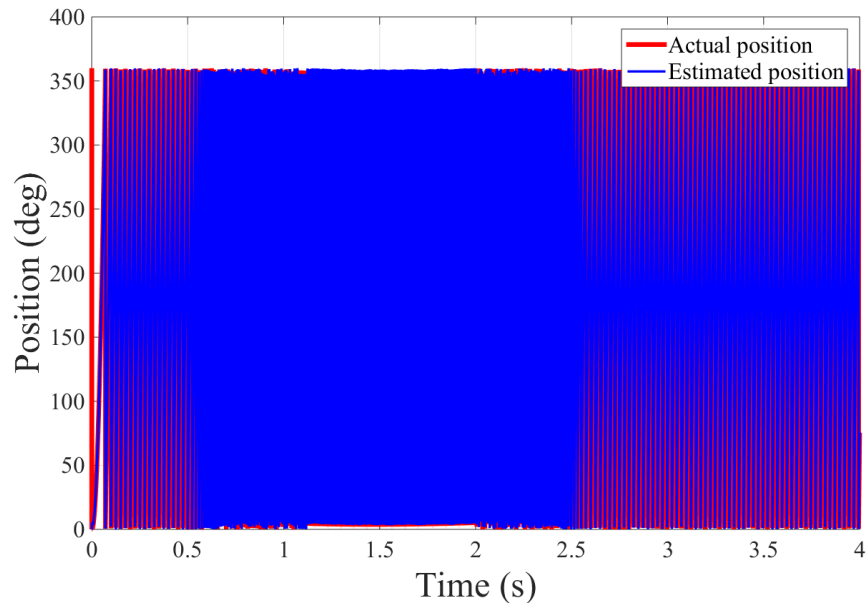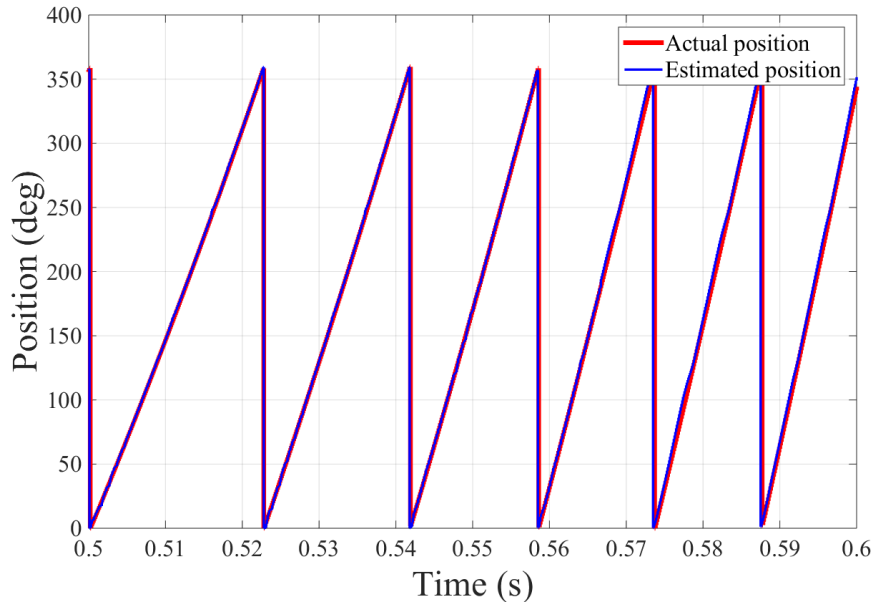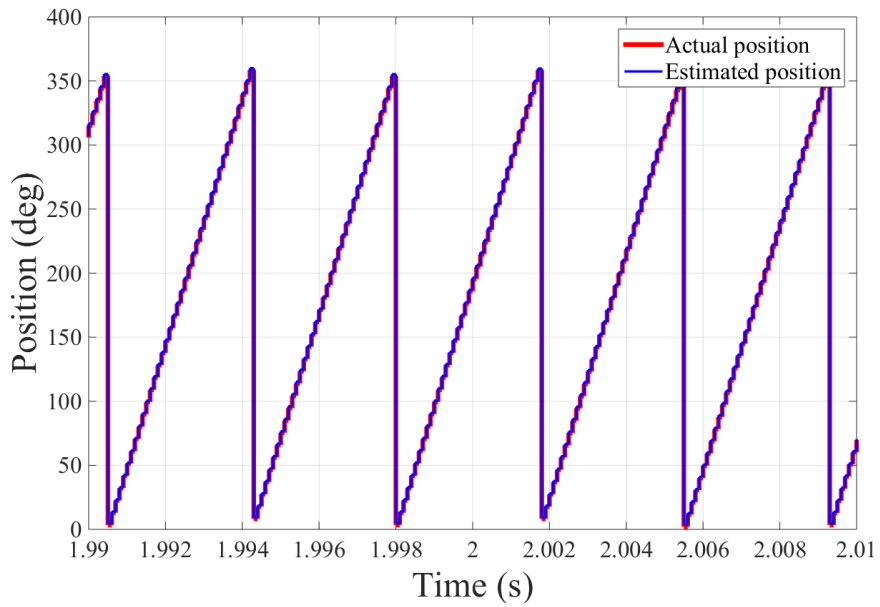
Fig. 5.27 Simulation results of rotor speed estimation at various speeds.

(a) Rotor position estimation for the whole operation period.

(b) Rotor position estimation when accelerating form 300 RPM.

(c) Rotor position estimation when decelerating from 2000 RPM.

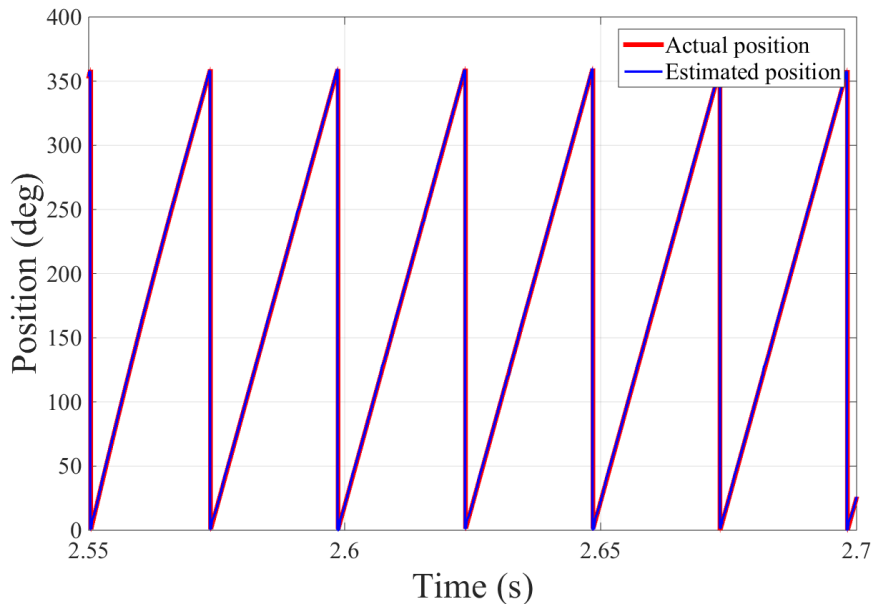(d) Rotor position estimation at the speed of 300 RPM.

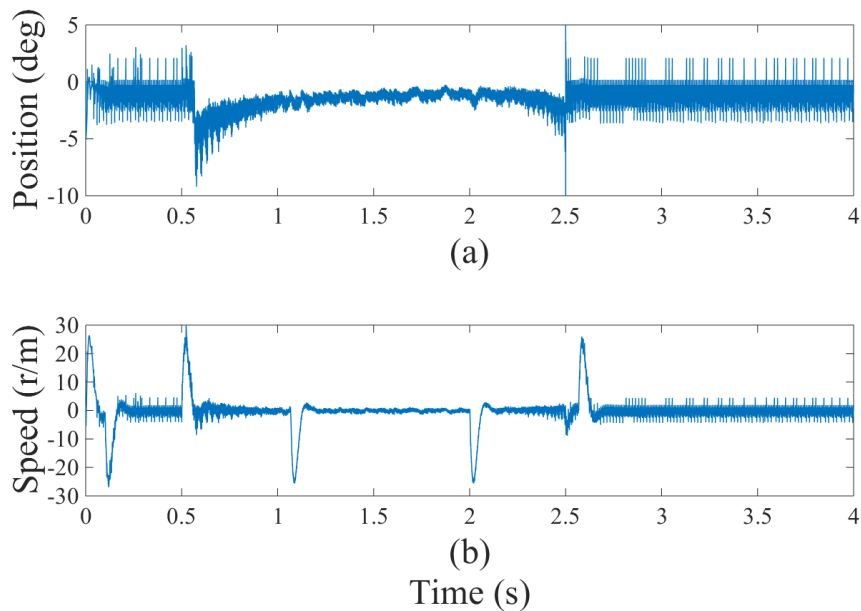Fig. 5.28 Simulation results of rotor position estimation.

Fig. 5.29 Simulation results of the estimation error of the position and speed (a) position

error; (b) speed error.

Chapter 6

EXPERIMENTS RESULTS

6.1. EXPERIMENTS SETUP

The effectiveness and robustness of proposed methods are verified by experiments in this chapter, including pulse injection method, SMO method, and the combination method.

The diagram of the experimental setup is shown in Fig. 6.1. The system setup consists of a controller, a DC-DC converter, a rectifier, the tested SRM, and the load BLDC. The control algorithm of pulse-injection and SMO are implemented by the controller board with TI's DSP TMS320F28335 on it. The switching signals are generated by the current controller and PWM modulator programmed in the DSP. These switching signals are sent to an asymmetric half-bridge converter to control the tested SRM. The tested SRM and the load brush-less DC (BLDC) machine are connected by shaft. The output of the BLDC is successively connected to the passive rectifier, DC/DC converter, and load resistor. Fig. 6.2 shows the experimental setup. In the experiments, the duty ratio of the DC/DC converter is adjusted to change the load torque on the tested SRM. As shown in Fig. 6.2 (b), the duty ratio is adjusted by tuning the variable resistor.

The value of the observer gains and reference parameters are the same as that of the simulation, and they are listed in TABLE 6.1.

TABLE 6.1 Experimental parameters

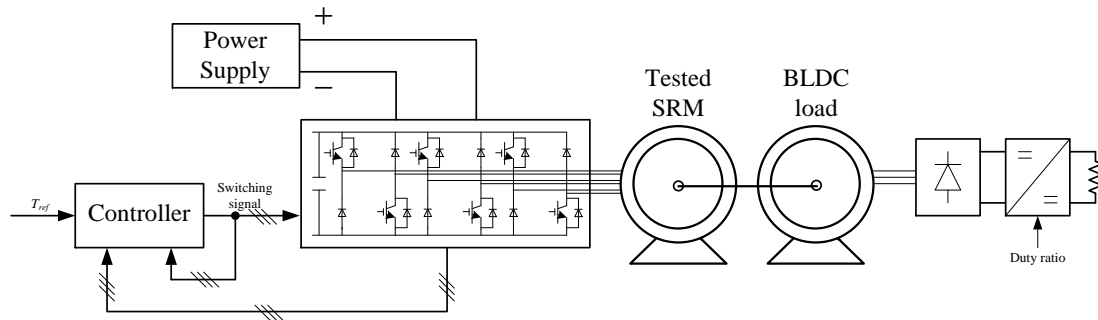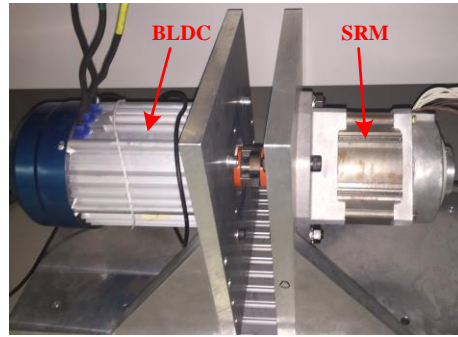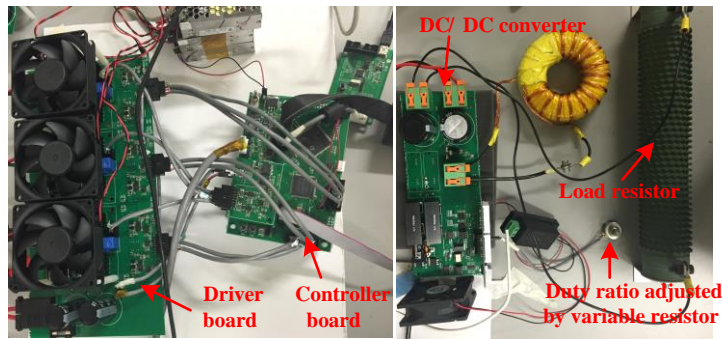| Parameters	Value
Reference current	10A
Rated DC power-supply	150V
Position gain k_θ	4500
Speed gain k_ω	2.7×10^5
Acceleration gain k_α	1.35×10^7
Sample frequency	10KHz
DSP frequency	150MHz

Fig. 6.1 Diagram of the experimental setup.

(a) Tested SRM and its load

(b) Digital controller and DC/DC convertor

Fig. 6.2 Experimental setup.

6.2. EXPERIMENTAL RESULTS

6.2.1. EXPERIMENTAL RESULTS AT LOW-SPEED OPERATION

In this section, the effectiveness and reliability of pulse injection method at low-speed operation is verified, and the experiment is performed at 275 RPM. The actual position and speed measured by the resolver are recorded for comparison. In order to easily observe and analyze, the waveform of rotor position and corresponding error are enlarged by zooming in several electrical periods. The rotor position estimation results are shown

in Fig. 6.3, including the comparison of actual and estimated position and the position error. Fig. 6.4 shows the experimental results of rotor speed estimation.

Two electrical circles are selected to show the comparison between the actual position and estimated position clearly. It is shown that the estimated position and actual position are almost overlapped at steady state. From the position error, we can see that the average position error is around 5°, and the maximum position error is about 30°. The percentages of position error in an electrical cycle are 1.38% and 8.33% respectively. Although sometimes the absolute value of position error is kind of high, the stability of the whole system will not be affected. And from the experimental results of speed estimation, it is clearly that the estimated speed can correctly track the actual speed. Overall, the pulse injection method is suitable for detecting rotor position and speed at low-speed operation with desirable accuracy.
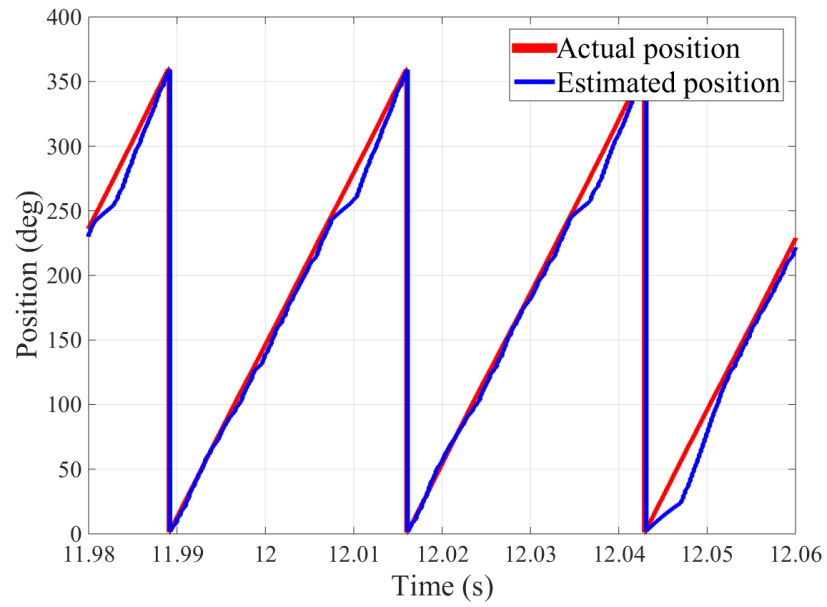
(a) Actual position vs. Estimated position.
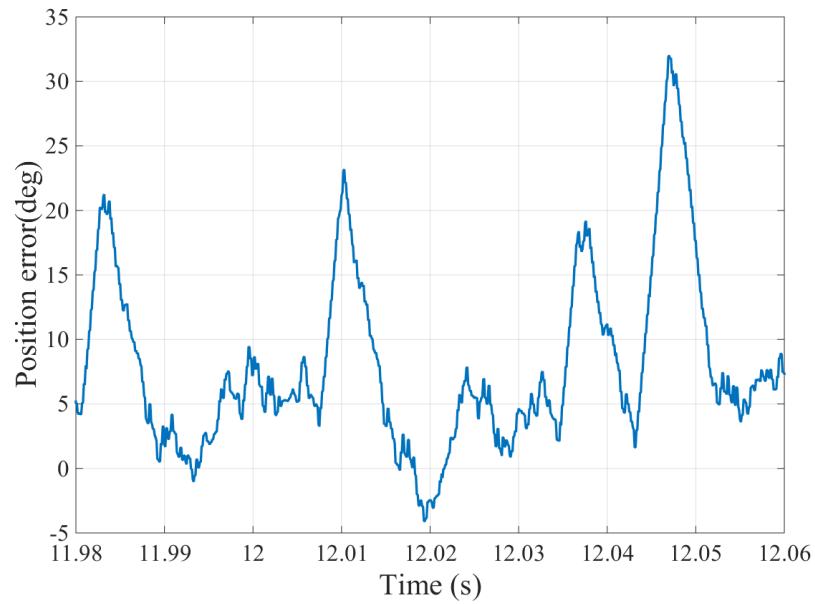
(b) Rotor postion errors.

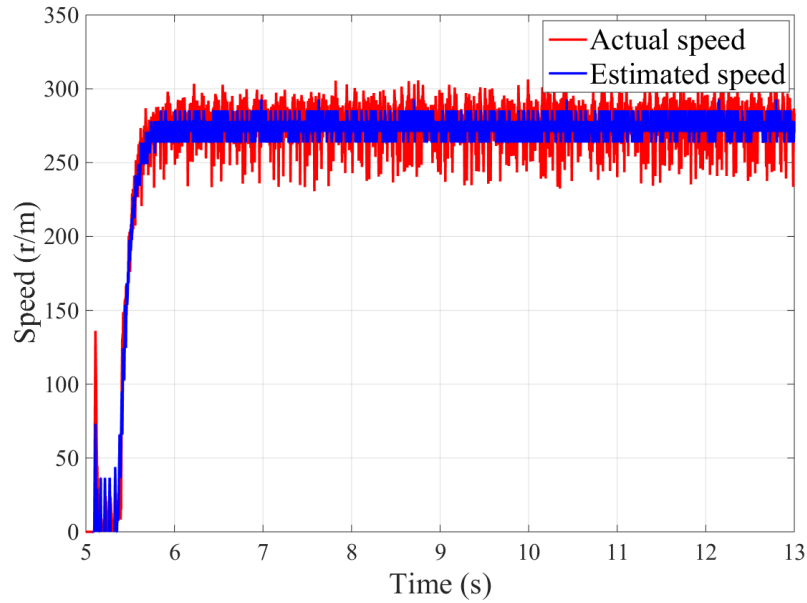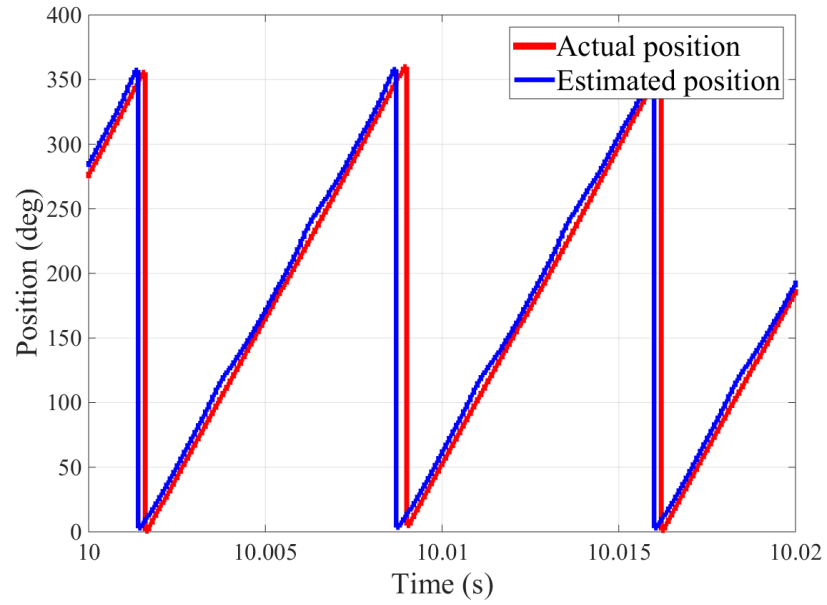Fig. 6.3 Experimental results of rotor position estimation at 275 RPM.

Fig. 6.4 Experimental results of rotor speed estimation at 275 RPM.

## 6.2.2. EXPERIMENTAL RESULTS AT HIGH-SPEED OPERATION

The SMO method is verified by experiments in this section. The actual position and speed are measured from the encoder and are recorded and compared with the estimation results. Fig. 6.5 (a) shows the comparison of actual and estimated position at 1000 RPM, and Fig. 6.5 (b) shows the corresponding position error. The rotor speed estimation result at 1000 RPM is shown in Fig. 6.6. Similarly, the experimental results of rotor position estimation and corresponding position error at 2000 RPM and 4000 RPM are shown in Fig. 6.7 and Fig. 6.9, respectively. And the comparison of actual and estimated speeds of 2000 RPM and 4000 RPM are respectively presented in Fig. 6.8 and Fig. 6.10.

Although there is a little shift between estimated position and actual position at 1000 RPM in Fig. 6.5 (a), the average position error is only about -9° with chattering from -6° to -14°. As we can see from Fig. 6.7, when increasing the rotor speed to 2000 RPM, the average position is about -7° with chattering from -5° to -10°. It is clearly shown in Fig. 6.9 (a) that estimated position ideally matches the actual position, and they are almost overlapped at 4000 RPM. The corresponding position error shown in Fig. 6.9 (b) is around -1°. The percentages of position error at three speeds are 2.5% (1000 RPM), 1.9% (2000 RPM), and 0.3% (4000 RPM). From the figures and data, it is shown that both the average position error and chattering of position error decreases with the increase of rotor speed. From Fig. 6.6, Fig. 6.8, and Fig. 6.10, it is shown that the estimated speed can perfectly track the actual speed.

From these experimental results, the rotor position and speed can be precisely estimated with an acceptable error. Besides, since the position error and chattering are smaller at high-speed operation, it demonstrates that the proposed SMO method is more suitable to be applied for detecting rotor position at high-speed operation with desirable accuracy.

(a) Actual position vs. Estimated position.
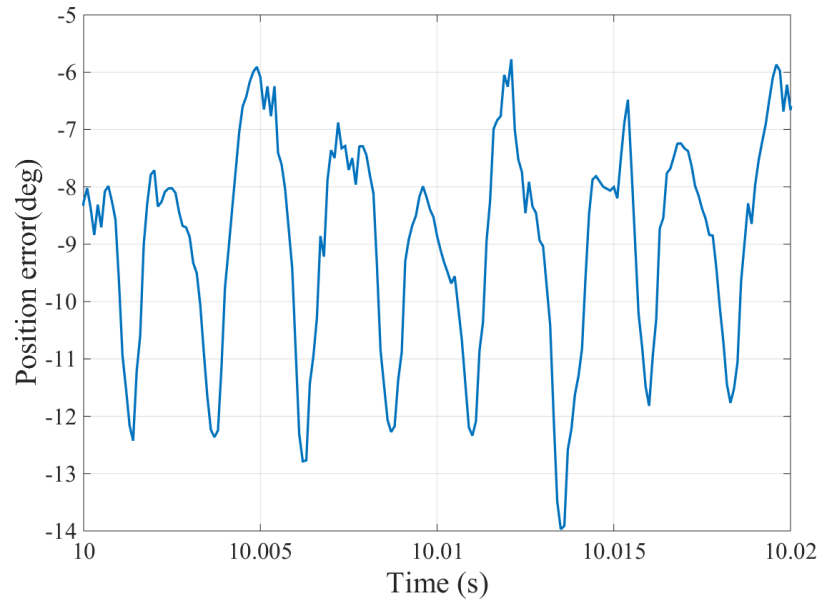
(b) Rotor position errors.

Fig. 6.5 Experimental results of rotor position estimation at 1000 RPM.

Fig. 6.6 Experimental results of rotor speed estimation at 1000 RPM.

(a) Actual position vs. Estimated position.

(b) Rotor position errors.

Fig. 6.7 Experimental results of rotor position estimation at 2000 RPM.
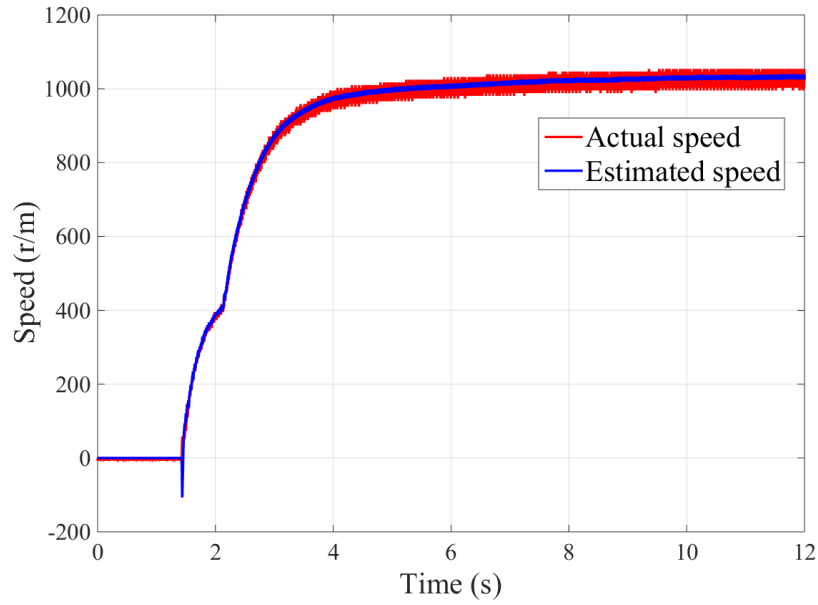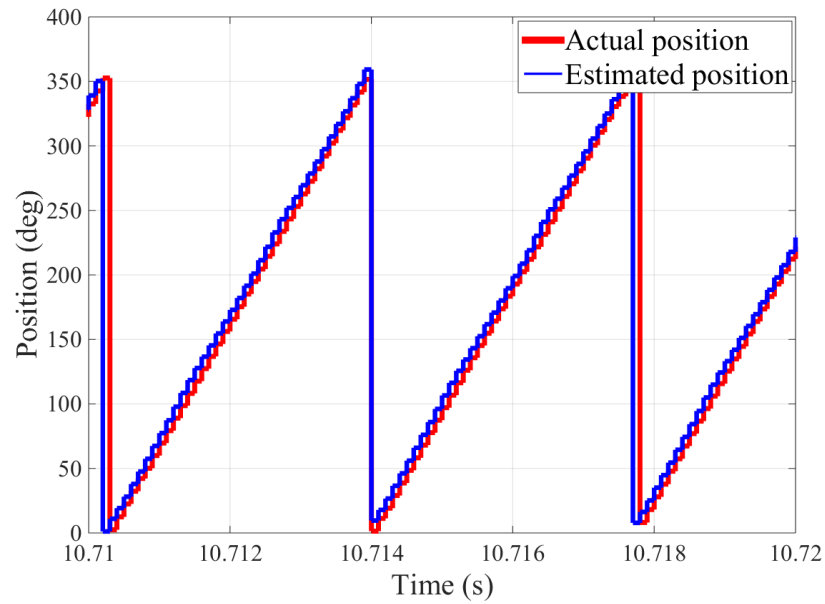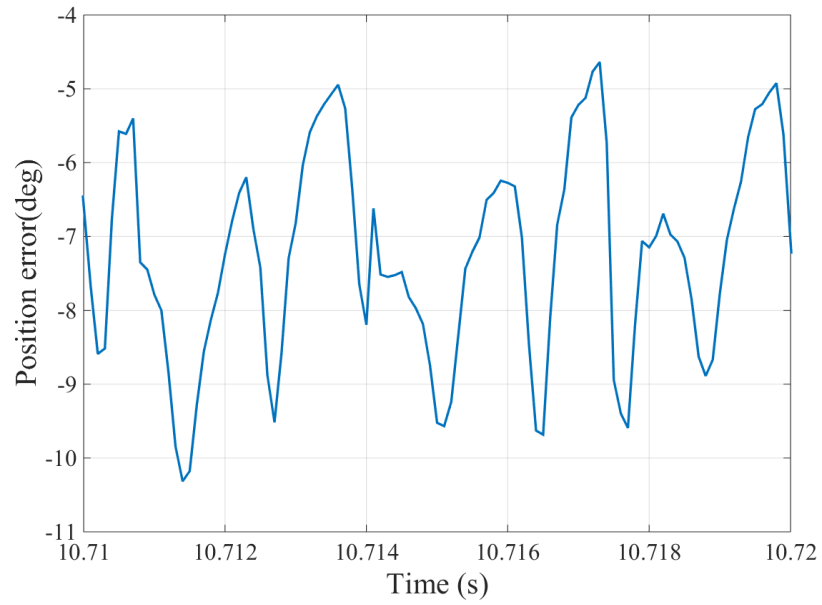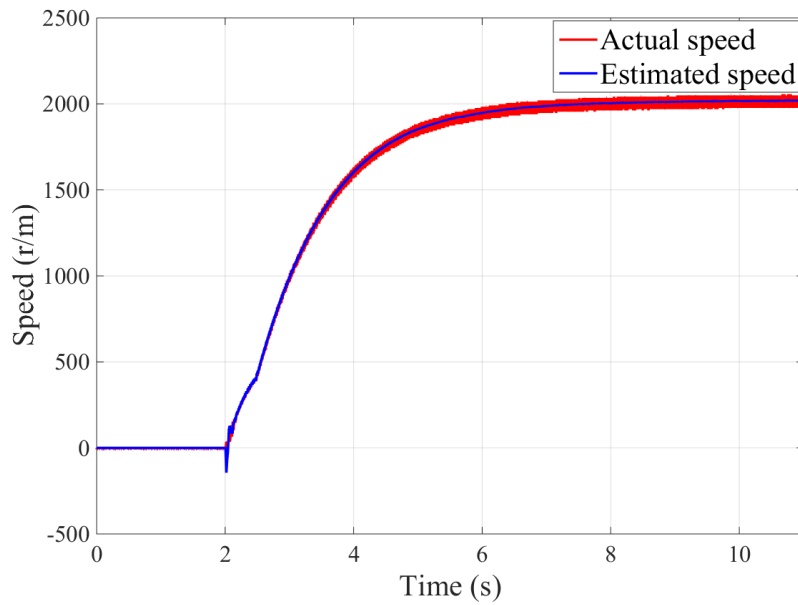

Fig. 6.8 Experimental results of rotor speed estimation at 2000 RPM.

(a) Actual position vs. Estimated position.
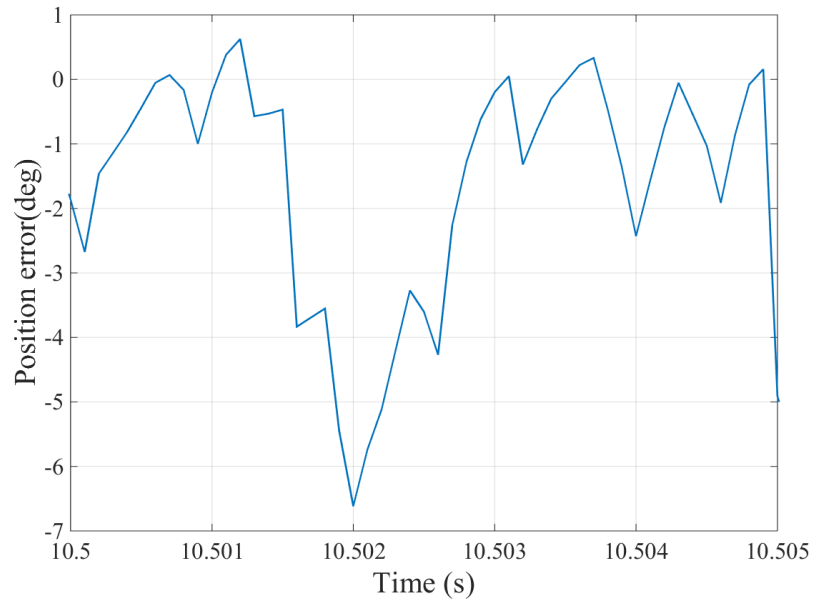
(b) Rotor position errors.

Fig. 6.9 Experimental results of rotor position estimation at 4000 RPM.
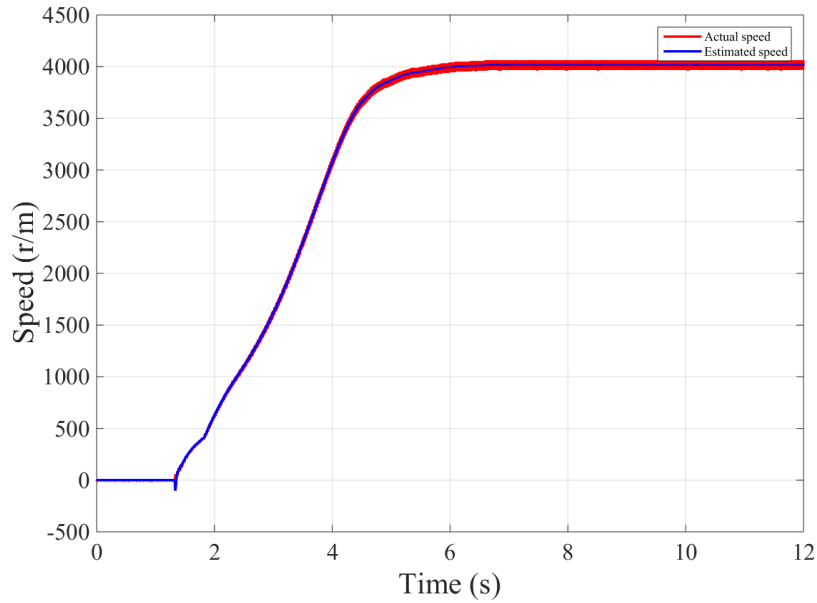
Fig. 6.10 Experimental results of rotor speed estimation at 4000 RPM.

6.2.3. EXPERIMENTAL RESULTS OF THE ENTIRE SPEED RANGE

The combination sensorless control method with pulse injection and SMO method is tested by changing the speeds during the whole executing period. The profile of actual and estimated speed is shown in Fig. 6.11. It indicates that the system operates around 300 RPM between 2s to 8s, and the rotor starts to accelerate from 7.8s; and then, the rotor speed reaches 2000 RPM at 15s; after that, the rotor starts to decelerate and stabilizes at 300 RPM at around 16s. And the comparison of actual and estimated position and its corresponding error at acceleration and deceleration points are described in Fig. 6.12 to Fig. 6.14.

Fig. 6.12 depicts the comparison results when rotor starts to accelerate from 300 RPM to 2000 RPM. The estimation method switches from pulse injection to SMO at 500 RPM. So the estimation method of the selected period is pulse injection method. The average position error is around 5° to 10° with maximum error to 20° or 35°. The estimated rotor position and actual rotor position are almost overlapped, and this shows the accuracy of pulse injection method when changing the value of speed during operation.

Fig. 6.13 describes the comparison results when rotor starts to decelerate from 2000 RPM to 300 RPM. And Fig. 6.14 shows the comparison of measured and actual rotor position when the speed reaches to 300 RPM. From these figures, it is obvious that the estimated position and actual position are almost overlapped, and the rotor position errors are insignificant.

From the experiments, when changing the rotor speed, namely acceleration or deceleration, the estimated rotor speed can smoothly track the actual speed, and the rotor position can still be detected with high accuracy by estimation methods. It demonstrates that proposed position sensorless methods can efficiently estimate rotor position and speed when changing the rotor speed during operation. Besides, the sensorless control method can smoothly switch between pulse injection method and SMO method without significant transit transient process.
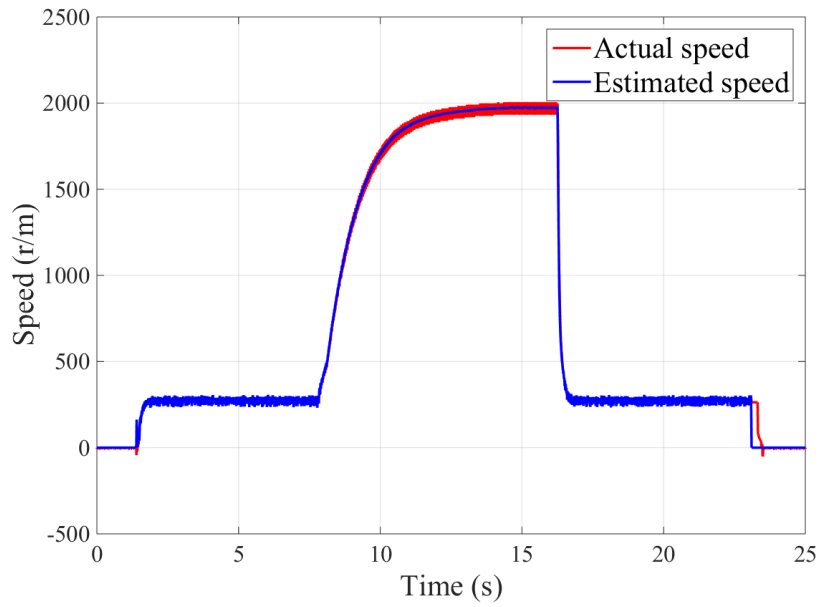
Fig. 6.11 Experimental results of speed with variation of speed.
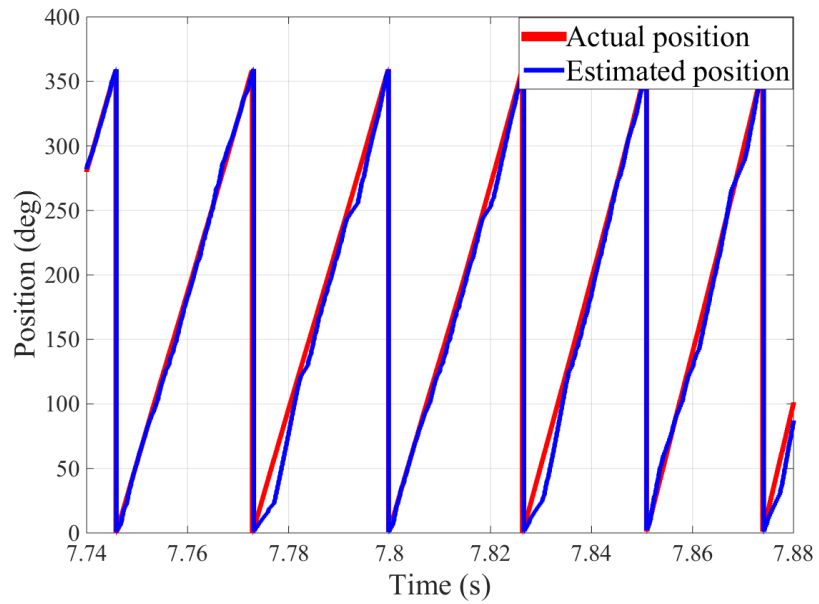
(a) Actual position vs. estimated position.
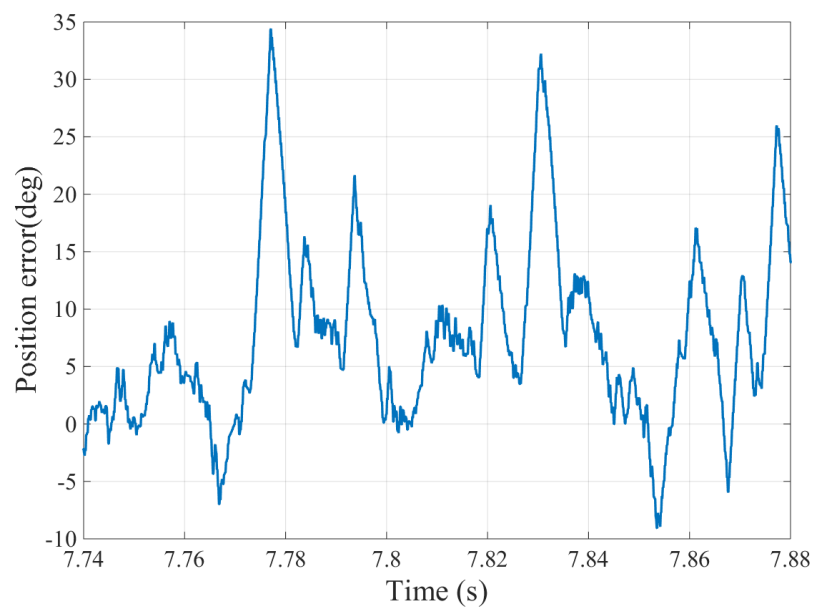
(b) Rotor position error.

Fig. 6.12 Experimental results of rotor position when rotor accelerates from 300 RPM.
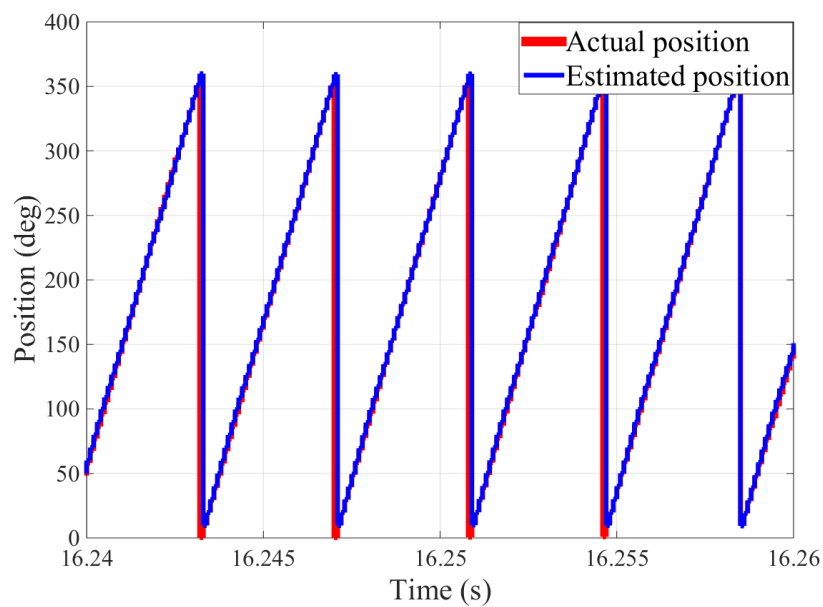
(a) Actual position vs. estimated position.
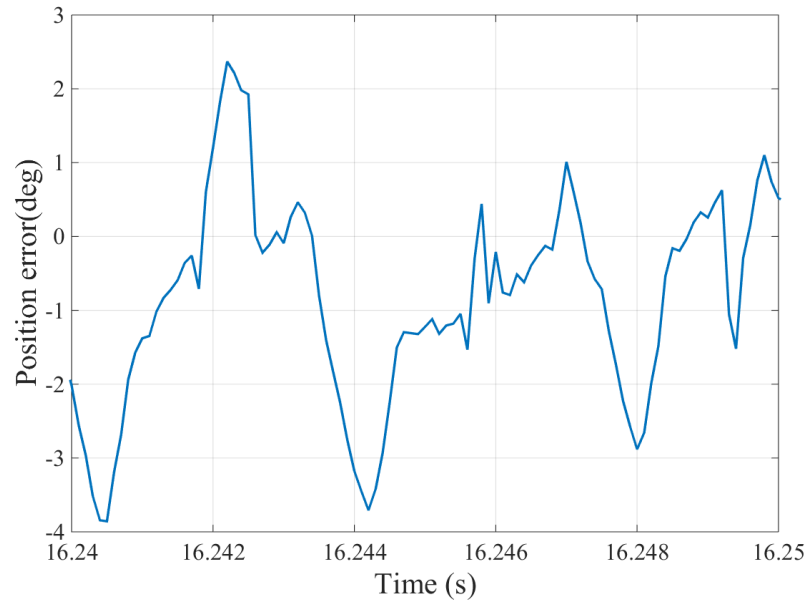
(c) Rotor position error.

Fig. 6.13 Experimental results of rotor position when rotor decelerates from 2000 RPM.
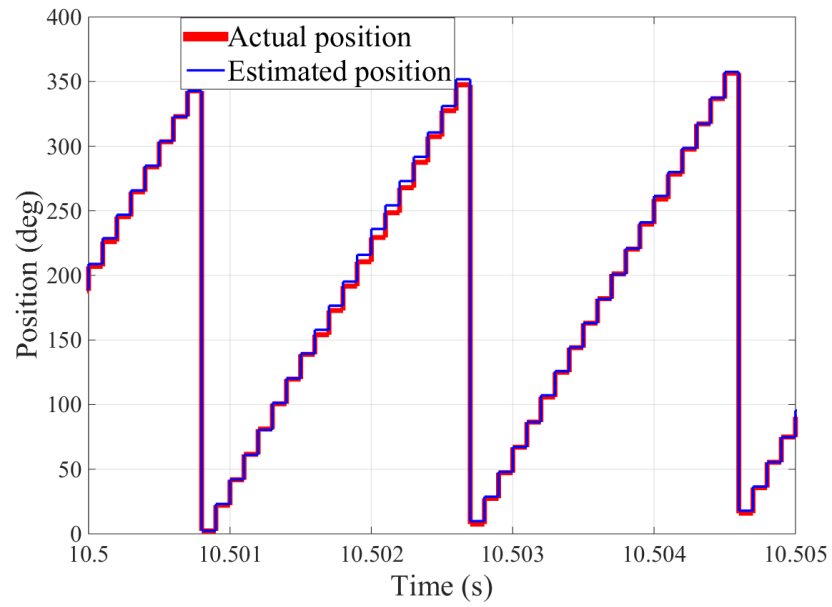

(a) Actual position vs. estimated position.

131
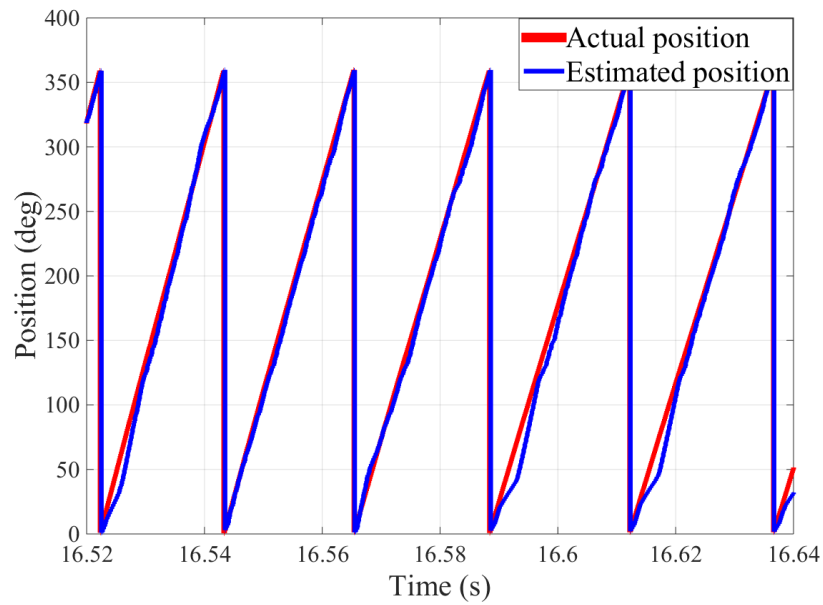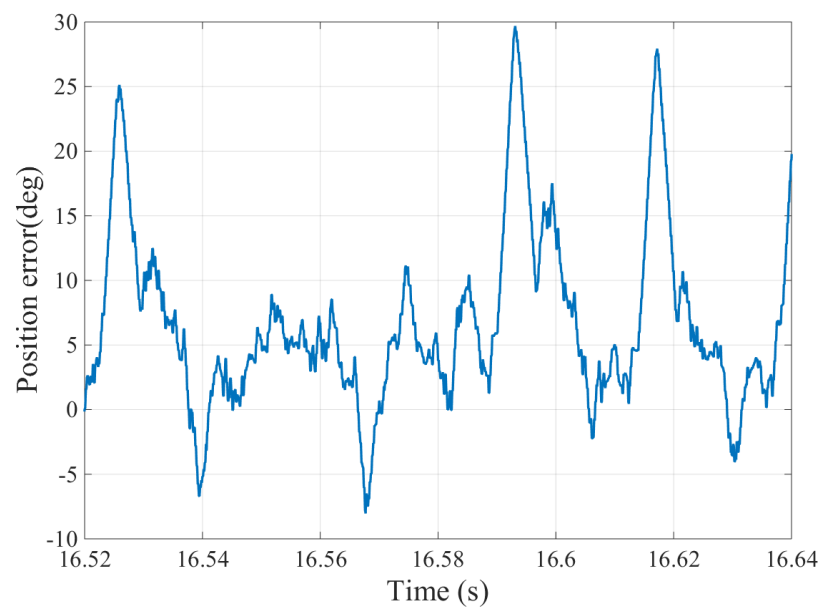
(b) Rotor position error.

Fig. 6.14 Experimental results of rotor position estimation when rotor reaches 300 RPM.

Chapter 7

CONCLUSION AND FUTURE WORK

In this thesis, a position sensorless control method for SRM drives based on the pulse injection and SMO with third order PLL is proposed. The pulse injection method requires less memory space and has merits of high reliability and accuracy. And the sliding mode observer has advantages of simple, fast, precise tracking, and high robustness. Besides, the costs can be reduced since no position sensor is needed and only current sensors are required in the system.

By injecting current pulses to idle phases, the phase inductance is calculated, which is used to determine the initial rotor position and to detect the rotor position and speed at low-speed operation. When the system operates at high-speed, the sliding mode observer is used to estimate the rotor position and speed with the measurement of three-phase currents. By combining these two methods together, the proposed position sensorless control can detect rotor position and speed with high accuracy and efficiency in the entire speed range. The third order PLL improves the dynamic response of the system.

The implementation of the proposed method is firstly studied by MATLAB/SIMULINK simulations. From the standstill position to the low-speed operation, simulation results show that position and speed can be precisely estimated by pulse injection method. And

SMO method shows its robustness and accuracy to estimate rotor position and speed at high-speed operation. The response is fast during acceleration period, and the error is comparably small at both steady state and transient state.

Experimental tests implemented on a three-phase 12/8 SRM prototype verify the high resolution of the position and speed estimation. Motor drive performance demonstrates the effectiveness of the proposed sensorless control method.

Recently, this position sensorless control method may be applied to pump system or home appliances like wash-machine. These motors do not require the four-quadrant operation and extreme high accuracy. So in order to apply sensorless control to an electrical vehicle, the accuracy and robustness need to be further improved, and the operation has to be able to switch arbitrarily among four quadrants. So the future work could concentrate on improving the accuracy, efficiency, and robustness. Besides, additional techniques can be integrated into the proposed sensorless control method to make it possible for the whole system to operate under four quadrants smoothly.

REFERENCE

[1] R. A. McCann, M. S. Islam, and I. Husain, "Application of a sliding-mode observer for position and speed estimation in switched reluctance motor drives," *IEEE Trans. Ind. Appl.*, vol. 37, no. 1, pp. 51–58, Feb. 2001.

[2] K. T. Chau and Institute of Electrical and Electronics Engineers, *Electric vehicle machines and drives: design, analysis and application*. 2015.

[3] T. J. E. Miller, "Converter Volt-Ampere Requirements of the Switched Reluctance Motor Drive," *IEEE Trans. Ind. Appl.*, vol. IA-21, no. 5, pp. 1136–1144, Sep. 1985.

[4] Q. Yu, B. Bilgin, and A. Emadi, "Loss and Efficiency Analysis of Switched Reluctance Machines Using a New Calculation Method," *IEEE Trans. Ind. Electron.*, vol. 62, no. 5, pp. 3072–3080, May 2015.

[5] Y. Yang, N. Schofield, and A. Emadi, "Double-Rotor Switched Reluctance Machine (DRSRM)," *IEEE Trans. Energy Convers.*, vol. 30, no. 2, pp. 671–680, Jun. 2015.

[6] B. Bilgin, A. Emadi, and M. Krishnamurthy, "Design Considerations for Switched Reluctance Machines With a Higher Number of Rotor Poles," *IEEE Trans. Ind. Electron.*, vol. 59, no. 10, pp. 3745–3756, Oct. 2012.

[7] P. C. Desai, M. Krishnamurthy, N. Schofield, and A. Emadi, "Novel Switched Reluctance Machine Configuration With Higher Number of Rotor Poles Than Stator Poles: Concept to Implementation," *IEEE Trans. Ind. Electron.*, vol. 57, no. 2, pp. 649–659, Feb. 2010.

[8]   Ji.-W. Ahn, "Switched Reluctance Motor," in *Torque Control*, M. T. Lamchich, Ed. InTech, 2011.

[9]   S. Vukosavic and V. R. Stefanovic, "SRM inverter topologies: a comparative evaluation," in *Conference Record of Industry Applications Society Annual Meeting*, Seattle, WA, USA, 1990, vol. 2, pp. 946–958.

[10] S. M. Lukic and A. Emadi, "State-Switching Control Technique for Switched Reluctance Motor Drives: Theory and Implementation," *IEEE Trans. Ind. Electron.*, vol. 57, no. 9, pp. 2932–2938, Sep. 2010.

[11] A. Emadi, *Energy-Efficient Electric Motors: Selection and Applications*. New York, NY: Marcel Dekker, 2004.

[12] M. Krishnamurthy, C. S. Edrington, A. Emadi, P. Asadi, M. Ehsani, and B. Fahimi, "Making the case for applications of switched reluctance motor technology in automotive products," *IEEE Trans. Power Electron.*, vol. 21, no. 3, pp. 659–675, May 2006.

[13] T. T. Borges, D. A. de Andrade, H. R. de Azevedo, and M. Luciano, "Switched reluctance motor drive at high speeds, with control of current," in *IEEE International Electric Machines and Drives Conference Record*, Milwaukee, WI, 1997, pp. TB1/12.1–TB1/12.3.

[14] H.-P. Chi, R.-L. Lin, and J.-F. Chen, "Simplified flux-linkage model for switched-reluctance motors," *IEE Proc. - Electr. Power Appl.*, vol. 152, no. 3, p. 577, 2005.

[15] D. A. Torrey, "Switched reluctance generators and their control," *IEEE Trans. Ind. Electron.*, vol. 49, no. 1, pp. 3–14, Feb. 2002.

[16] J. Ye, B. Bilgin, and A. Emadi, "An Offline Torque Sharing Function for Torque Ripple Reduction in Switched Reluctance Motor Drives," *IEEE Trans. Energy Convers.*, vol. 30, no. 2, pp. 726–735, Jun. 2015.

[17] J. Ye, B. Bilgin, and A. Emadi, "An Extended-Speed Low-Ripple Torque Control of Switched Reluctance Motor Drives," *IEEE Trans. Power Electron.*, vol. 30, no. 3, pp. 1457–1470, Mar. 2015.

[18] T. J. E. Miller, "Optimal design of switched reluctance motors," *IEEE Trans. Ind. Electron.*, vol. 49, no. 1, pp. 15–27, Feb. 2002.

[19] Baiming Shao and A. Emadi, "A digital PWM control for switched reluctance motor drives," in *IEEE Vehicle Power and Propulsion Conference*, Lille, 2010, pp. 1–6.

[20] B. Fahimi, G. Suresh, J. Mahdavi, and M. Ehsami, "A new approach to model switched reluctance motor drive application to dynamic performance prediction, control and design," in *29th Annual IEEE Power Electronics Specialists Conference*, Fukuoka, 1998, vol. 2, pp. 2097–2102.

[21] J. Mahdavi, G. Suresh, B. Fahimi, and M. Ehsani, "Dynamic modeling of nonlinear SRM drive with Pspice," in *32nd IEEE IAS ConferenceAnnual Meeting*, New Orleans, LA, 1997, vol. 1, pp. 661–667.

[22] S. M. Lukic and A. Emadi, "Modeling of electric machines for automotive applications using efficiency maps," in *2003 Electrical Manufacturing and Coil Winding Expo*, IN, 2003, pp. 543–550.

[23] M. Ilic'-Spong, R. Marino, S. Peresada, and D. Taylor, "Feedback linearizing control of switched reluctance motors," *IEEE Trans. Autom. Control*, vol. 32, no. 5, pp. 371–379, May 1987.

[24] B. Bilgin and A. Emadi, "Electric Motors in Electrified Transportation: A step toward achieving a sustainable and highly efficient transportation system," *IEEE Power Electron. Mag.*, vol. 1, no. 2, pp. 10–17, Jun. 2014.

[25] B. Fahimi, G. Suresh, and M. Ehsani, "Review of sensorless control methods in switched reluctance motor drives," in *Conference Record of IEEE Industry Applications Conference*, Rome, 2000, vol. 3, pp. 1850–1857.

[26] B. Fahimi and A. Emadi, "Position sensorless control: presenting technology ready for switched reluctance machine drive applications," *IEEE Ind. Appl. Mag.*, vol. 10, no. 1, pp. 40–47, Feb. 2004.

[27] J. P. Lyons, S. R. MacMinn, and M. A. Preston, "Flux-current methods for SRM rotor position estimation," in *Conference Record of IEEE Industry Applications Society Annual Meeting*, Dearborn, MI, USA, 1991, vol. 1, pp. 482–487.

[28] W. Zeng, C. Liu, Q. Zhou, J. Cai, and L. Zhang, "A new flux/current method for SRM rotor position estimation," in *International Conference on Electrical Machines and Systems*, Tokyo, 2009, pp. 1–6.

[29] G. Gallegos-Lopez, P. C. Kjaer, and T. J. E. Miller, "High-grade position estimation for SRM drives using flux linkage/current correction model," *IEEE Trans. Ind. Appl.*, vol. 35, no. 4, pp. 859–869, Aug. 1999.

[30] G. Suresh, B. Fahimi, K. M. Rahman, and M. Ehsani, "Inductance based position encoding for sensorless SRM drives," 1999, vol. 2, pp. 832–837.

[31] H. Gao, F. R. Salmasi, and M. Ehsani, "Inductance Model-Based Sensorless Control of the Switched Reluctance Motor Drive at Low Speed," *IEEE Trans. Power Electron.*, vol. 19, no. 6, pp. 1568–1573, Nov. 2004.

[32] H. Gao, F. R. Salmasi, and M. Ehsani, "Sensorless control of SRM at standstill," in *16th Annual IEEE Applied Power Electronics Conference and Exposition (APEC)*, Anaheim, CA, 2001, vol. 2, pp. 850–856.

[33] G. Pasquesoone, R. Mikail, and I. Husain, "Position Estimation at Starting and Lower Speed in Three-Phase Switched Reluctance Machines Using Pulse Injection and Two Thresholds," *IEEE Trans. Ind. Appl.*, vol. 47, no. 4, pp. 1724–1731, Jul. 2011.

[34] P. P. Acarnley, R. J. Hill, and C. W. Hooper, "Detection of Rotor Position in Stepping and Switched Motors by Monitoring of Current Waveforms," *IEEE Trans. Ind. Electron.*, vol. IE-32, no. 3, pp. 215–222, Aug. 1985.

[35] S. R. MacMinn, W. J. Rzesos, P. M. Szczesny, and T. M. Jahns, "Application of sensor integration techniques to switched reluctance motor drives," *IEEE Trans. Ind. Appl.*, vol. 28, no. 6, pp. 1339–1344, Dec. 1992.

[36] E. Ofori, T. Husain, Y. Sozer, and I. Husain, "A Pulse-Injection-Based Sensorless Position Estimation Method for a Switched Reluctance Machine Over a Wide Speed Range," *IEEE Trans. Ind. Appl.*, vol. 51, no. 5, pp. 3867–3876, Sep. 2015.

[37] M. Ehsani, I. Husain, S. Mahajan, and K. R. Ramani, "New modulation encoding techniques for indirect rotor position sensing in switched reluctance motors," *IEEE Trans. Ind. Appl.*, vol. 30, no. 1, pp. 85–91, Feb. 1994.

[38] A. Cheok and N. Ertugrul, "A model free fuzzy logic based rotor position sensorless switched reluctance motor drives," in *IEEE Industry Applications Conference*, San Diego, CA, 1996, vol. 1, pp. 76–83.

[39] A. Bellini, F. Filippetti, G. Franceschini, C. Tassoni, and P. Vas, "Position sensorless control of a SRM drive using ANN-techniques," in *33rd IEEE IAS Annual Meeting*, St. Louis, MO, USA, 1998, vol. 1, pp. 709–714.

[40] E. Mese and D. A. Torrey, "An approach for sensorless position estimation for switched reluctance motors using artifical neural networks," *IEEE Trans. Power Electron.*, vol. 17, no. 1, pp. 66–75, Jan. 2002.

[41] Tingna Shi, Changliang Xia, Mingchao Wang, and Qian Zhang, "Single Neural PID Control for Sensorless Switched Reluctance Motor Based on RBF Neural Network," in *6th World Congress on Intelligent Control and Automation*, Dalian, 2006, pp. 8069–8073.

[42] F. Peng, J. Ye, and A. Emadi, "A Digital PWM Current Controller for Switched Reluctance Motor Drives," *IEEE Trans. Power Electron.*, vol. 31, no. 10, pp. 7087 – 7098, Oct. 2016.

[43] F. Peng, J. Ye, and A. Emadi, "Position sensorless control of switched reluctance motor based on numerical method," in *2016 IEEE Energy Conversion Congress and Expo (ECCE'16*, Milwaukee, WI, 2016.

[44] Y. J. Zhan, C. C. Chan, and K. T. Chau, "A novel sliding-mode observer for indirect position sensing of switched reluctance motor drives," *IEEE Trans. Ind. Electron.*, vol. 46, no. 2, pp. 390–397, Apr. 1999.

[45] S. Mir, M. E. Elbuluk, and I. Husain, "Torque-ripple minimization in switched reluctance motors using adaptive fuzzy control," *IEEE Trans. Ind. Appl.*, vol. 35, no. 2, pp. 461–468, Apr. 1999.

[46] M. S. Islam, I. Husain, R. J. Veillette, and C. Batur, "Design and performance analysis of sliding-mode observers for sensorless operation of switched reluctance motors," *IEEE Trans. Control Syst. Technol.*, vol. 11, no. 3, pp. 383–389, May 2003.

[47] M. Divandari, A. Koochaki, M. Jazaeri, and H. Rastegar, "A Novel Sensorless SRM Drive via Hybrid Observer of Current Sliding Mode and Flux linkage," in *IEEE International Electric Machines & Drives Conference*, Antalya, 2007, vol. 1, pp. 45–49.

[48] G. Tan, Z. Ma, S. Kuai, and X. Zhang, "Four-quadrant position sensorless control in Switched Reluctance Motor drives based on Sliding Mode Observer," in *IEEE International Conference on Electrical Machines and Systems*, Tokyo, 2009, pp. 1–5.

[49] B. Fahimi, A. Emadi, and R. B. Sepe, "Four-Quadrant Position Sensorless Control in SRM Drives Over the Entire Speed Range," *IEEE Trans. Power Electron.*, vol. 20, no. 1, pp. 154–163, Jan. 2005.

[50] S. A. Hossain, I. Husain, H. Klode, B. Lequesne, A. M. Omekanda, and S. Gopalakrishnan, "Four-quadrant and zero-speed sensorless control of a switched reluctance motor," *IEEE Trans. Ind. Appl.*, vol. 39, no. 5, pp. 1343–1349, Sep. 2003.

[51] J. Ye, B. Bilgin, and A. Emadi, "Elimination of Mutual Flux Effect on Rotor Position Estimation of Switched Reluctance Motor Drives Considering Magnetic Saturation," *IEEE Trans. Power Electron.*, vol. 30, no. 2, pp. 532–536, Feb. 2015.

[52] M. Krishnamurthy, C. S. Edrington, and B. Fahimi, "Prediction of rotor position at standstill and rotating shaft conditions in switched reluctance machines," *IEEE Trans. Power Electron.*, vol. 21, no. 1, pp. 225–233, Jan. 2006.

[53] J.-J. E. Slotine, J. K. Hedrlek, and E. A. Mlsawa, "On Sliding Observers for Nonlinear Systems," in *IEEE American Control Conference*, Seattle, WA, 1986, pp. 1794 – 1800.

[54] I. Husain, S. Sodhi, and M. Ehsani, "A sliding mode observer based controller for switched reluctance motor drives," in *Conference Record of IEEE Industry Applications Society Annual Meeting*, Denver, CO, 1994, vol. 1, pp. 635–643.

[55] A. Levant, "Universal single-input-single-output (SISO) sliding-mode controllers with finite-time convergence," *IEEE Trans. Autom. Control*, vol. 46, no. 9, pp. 1447–1451, Sep. 2001.

[56] Man Zhihong, A. P. Paplinski, and H. R. Wu, "A robust MIMO terminal sliding mode control scheme for rigid robotic manipulators," *IEEE Trans. Autom. Control*, vol. 39, no. 12, pp. 2464–2469, Dec. 1994.

[57] Yu-Sheng Lu and Jian-Shiang Chen, "A self-organizing fuzzy sliding-mode controller design for a class of nonlinear servo systems," *IEEE Trans. Ind. Electron.*, vol. 41, no. 5, pp. 492–502, Oct. 1994.

[58] B. Bandyopadhyay, K. S. Kim, and F. Deepak, *Sliding mode control using novel sliding surfaces*. Berlin: Springer Verlag, 2009.

[59] Jin Ye, P. Malysz, and A. Emadi, "A Fixed-Switching-Frequency Integral Sliding Mode Current Controller for Switched Reluctance Motor Drives," *IEEE J. Emerg. Sel. Top. Power Electron.*, vol. 3, no. 2, pp. 381–394, Jun. 2015.

[60] W. Perruquetti and J. P. Barbot, Eds., *Sliding mode control in engineering*. New York: M. Dekker, 2002.

[61] J.-J. E. Slotine and W. Li, *Applied nonlinear control*. Englewood Cliffs, N.J: Prentice Hall, 1991.

[62] Xiao Wang, Fei Peng, and A. Emadi, "A position sensorless control of switched reluctance motors based on sliding-mode observer," in *IEEE Transportation Electrification Conference and Expo (ITEC)*, Dearborn, MI, USA, 2016, pp. 1–6.